submitted to ApJ, Version: February 24, 2016
Preprint typeset using LaTeX style emulateapj v. 01/23/15

arXiv:1602.06960v1 [astro-ph.GA] 22 Feb 2016

THE BLACK HOLE - BULGE MASS RELATION IN MEGAMASER HOST GALAXIES*

Ronald Läsker[1,7], Jenny E. Greene[2], Anil Seth[3], Glenn van de Ven[1], James A. Braatz[4], Christian Henkel[5,6], and K. Y. Lo[4],

[1]Max-Planck Institut für Astronomie, Königstuhl 17, D-69117, Heidelberg, Germany; e-mail:laesker@mpia.de
[2]Department of Astrophysical Sciences, 4 Ivy Lane, Peyton Hall, Princeton University, Princeton, NJ 08544, USA
[3]Department of Physics & Astronomy, 201 James Fletcher Bldg., 115 South 1400 East, University of Utah, Salt Lake City, UT 84112, USA
[4]National Radio Astronomy Observatory, 520 Edgemont Rd., Charlottesville, VA 22903, USA
[5]Max-Planck-Institut für Radioastronomie, Auf dem Hügel 69, D-31212 Bonn, Germany
[6]Astron. Dept., King Abdulaziz University, P.O. Box 80203, Jeddah 21589, Saudi Arabia and
[7]Finnish Centre for Astronomy with ESO (FINCA), University of Turku, Väisäläntie 20, 21500 Kaarina, Finland

submitted to ApJ, Version: February 24, 2016

ABSTRACT

We present *HST* images for nine megamaser disk galaxies with the primary goal of studying photometric BH-galaxy scaling relations. The megamaser disks provide the highest-precision extragalactic BH mass measurements, while our high-resolution *HST* imaging affords us the opportunity to decompose the complex nuclei of their late-type hosts in detail. Based on the morphologies and shapes of the galaxy nuclei, we argue that most of these galaxies' central regions contain secularly evolving components (pseudo-bulges), and in many cases we photometrically identify co-existing "classical" bulge components as well. Using these decompositions, we draw the following conclusions: (1) The megamaser BH masses span two orders of magnitude (10^6 – $10^8\,M_\odot$) while the stellar mass of their spiral host galaxies are all $\sim 10^{11}\,M_\odot$ within a factor of three; (2) the BH masses at a given bulge mass or total stellar mass in the megamaser host spiral galaxies tend to be lower than expected, when compared to an extrapolation of the BH-bulge relation based on early-type galaxies; (3) the observed large intrinsic scatter of BH masses in the megamaser host galaxies raises the question of whether scaling relations exist in spiral galaxies.

Subject headings: galaxies: bulges, galaxies: photometry, galaxies: structure, methods: observational, techniques: photometric

1. INTRODUCTION

Supermassive black holes (BHs) play a special role in galaxy evolution. They are a ubiquitous component of massive galaxies (e.g., Kormendy & Ho 2013), and appear to approximately comprise a fixed fraction of the mass of the spheroidal component of the galaxy (e.g., McConnell & Ma 2013). Motivated by these scaling relations, theory invokes energy injection from actively accreting BHs to self-regulate BH growth (Debuhr et al. 2010), truncate star formation in massive galaxies (e.g., Silk & Rees 1998; Springel et al. 2005), and keep gas in clusters from cooling (e.g., Fabian 2012).

However, our understanding of BH demographics is far from complete. In particular, while we now have dynamical BH mass measurements for more than fifty galaxies, these galaxies convey a biased view of the galaxy population. They are skewed towards dense elliptical galaxies (van den Bosch et al. 2015). They are also biased towards massive systems with few exceptions (e.g., Seth et al. 2010, 2014). Spiral galaxies are particularly challenging; due to both the typically low BH masses and the presence of dust, star formation, and non-axisymmetric components (e.g., bars), stellar and gas dynamical modeling is far more challenging. These limitations hinder our ability to diagnose the underlying physical mechanisms driving the scaling relations.

There is one method that delivers high-precision, high-accuracy dynamical BH masses in spiral galaxy nuclei: fitting the rotation curves of megamaser disks (e.g., Herrnstein et al. 2005; Kuo et al. 2011). In these special systems, we observe extremely luminous 22 GHz H_2O masers in an edge-on accretion disk on ~ 0.5 pc scales from a weakly accreting supermassive BH (see review by Lo 2005). The precision of the BH mass measurement is actually limited by our knowledge of the galaxy distances. As first demonstrated with the prototypical megamaser disk galaxy NGC4258 (Herrnstein et al. 1999), it is also possible to measure a geometric distance using very-long-baseline observations (VLBI) in combination with single-dish monitoring of the acceleration of the systemic megamasers in the disk. These geometric distance measurements are the primary goal of the Megamaser Cosmology Project (MCP; Reid et al. 2009; Braatz et al. 2010, and associated follow-up publications). Thus far, five galaxies have direct distance measurements (NGC4258, NGC5765b, NGC6264, NGC6323, UGC3789 in Herrnstein et al. 1999; Gao et al. 2015; Kuo et al. 2013, 2015; Reid et al. 2013). At least nine galaxies have reliable megamaser-based BH mass measurements: NGC1194, NGC2273, NGC2960, NGC4388, NGC6264 and NGC6323 (Kuo et al. 2011), as well as NGC3993 (Kondratko et al. 2008), NGC4258 (e.g. Miyoshi et al. 1995; Herrnstein et al. 2005; Humphreys et al. 2013), and UGC3789 (Reid et al. 2009; Kuo et al. 2011).

* Based on observations made with the NASA/ESA Hubble Space Telescope, obtained at the Space Telescope Science Institute, which is operated by the Association of Universities for Research in Astronomy, Inc., under NASA contract NAS 5-26555. These observations are associated with program 12185.

The megamaser disk galaxies allow us to peer through the gas, dust, and star formation to directly measure BH masses in spiral galaxy nuclei as well as get a handle on secular BH fueling mechanisms (Greene et al. 2013, 2014). In previous work we have studied the relationship between galaxy velocity dispersion σ^* and BH mass in megamaser disk galaxies (Greene et al. 2010). Here we tackle the relationship between BH mass and bulge mass in these objects. Although a number of prior works have included bulge luminosities for many of these galaxies (e.g., Greene et al. 2010; Kormendy & Ho 2013; Graham & Scott 2015), in this paper we demonstrate that there is significant substructure on sub-arcsecond scales, and that disentangling the bulge components from other nuclear components requires the highest possible spatial resolution provided by the Hubble Space Telescope.

This paper contains many technical sections. In Section 2 we describe the sample, our data sources, and data processing. In Section 3 we decompose the two-dimensional surface brightness profiles and in Section 4 we investigate the nature of the bulge components of the megamaser disk host galaxies. Those interested in the main results can go directly to Section 5, where we discuss the megamaser disks in the BH-galaxy mass plane, and then fit the scaling relations including the new measurements presented here. In Section 6 we summarize and discuss our results. The redshift distances to our targets are based on $H_0 = 70\,\mathrm{km\,s^{-1}\,Mpc^{-1}}$, a value that is consistent with all the published values of H_0 based on geometric distance determinations of megamaser disk galaxies (see MCP references given above).

2. DATA

2.1. *Sample*

Our sample of megamaser disk galaxies with BH masses is taken from Greene et al. (2010), with most of the $M_{\rm BH}$ measurements provided by Kuo et al. (2011, Table 1). We focus on these nine galaxies because they have Keplerian megamaser rotation curves and high-resolution imaging data, and thus well-determined $M_{\rm BH}$. While the BH mass we adopt for IC2560 ($10^{6.4\pm0.4}\,M_\odot$, Kuo et al. 2011) is based on single-dish data, published and preliminary reductions of VLBI data yield a $\log M_{\rm BH}/\,M_\odot$ of 6.54 ± 0.06 (Yamauchi et al. 2012) and 6.64 ± 0.03 (Wagner et al. in prep). If we were to adopt those values, the results for the BH scaling relations (relation parameter and subsample offsets, see Section 5) barely change (within a few percent of the uncertainties). Several of our targets are $> 50\,$Mpc away, and most of them were previously known or suspected to host small-scale structures (nuclear rings, disks or bars) in addition to the bulge. High-resolution imaging is thus essential for a robust analysis. We do not include Circinus, NGC1068, or NGC4945 in this work, since comparable high-resolution data are not readily available for them, but we will consider the first two as a secondary sample in §5.

2.2. HST *imaging*

The high-resolution *HST* data (FWHM= $0\farcs15$ in the $H-$band corresponding to 50 pc at the median sample distance of 70 Mpc) were taken between October 2010 and November 2011 (see Table 1). We obtained *HST*/WFC3-IR imaging with filters F110W and F160W (similar to 2MASS $J-$ and $H-$band) for each galaxy. Within the same program we also acquired WFC-UVIS exposures in the F336W, F438W and F814W filters, (roughly U, B and $I-$band). We base our bulge luminosities and derived masses on the $H-$band data, in order to reduce the uncertainties associated with dust obscuration and variations in stellar population, as compared to optical bands. Indeed, many of the late-type galaxies in our sample are quite dusty and have complicated color profiles. We use the color information contained in the UVIS bands for a refined luminosity-mass conversion.

All of our galaxies were imaged in four exposures with F160W using sub-pixel dithering and a total exposure time of 422 sec. They were co-added and cleaned of cosmic rays using the PyFits MultiDrizzle pipeline[2]. In order to fit our five-band observations into two orbits, we utilize sub-arrays to avoid buffer dumps. The FOV of the subarray is 70×62 arcseconds, which is filled by the target in all cases. MultiDrizzle provides exposure time maps for the combined frame that we use to calculate the noise map needed for model fitting with GALFIT.

2.3. *Ground-based $K-$band imaging*

Since our *HST* data do not cover the outskirts of our target galaxies, we obtained additional wide-field imaging data. Most of these were ground-based K-band images, acquired from 2010-2012 on the Apache Point Observatory (APO) and WIYN[3] 3.5-m telescopes, using the NICFPS and WHIRC instruments respectively (http://nicfps.colorado.edu/, Smee et al. 2011). In two fields (IC2560 and NGC3993), sufficiently deep NIR images were not available; here we used *HST* WFC3 F814W and Las Campanas Observatory (LCO) du Pont 100-inch SITe2K-CCD I-band images. For details of instruments, exposure times and observing dates, see Table 1. Apart from providing valuable constraints on the derived galaxy parameters and thus allowing robust fits to the complex morphologies we encounter, their FOV is also large enough to allow reliable background subtraction, unbiased by galaxy light. In ground-based K-band images, these advantages are tempered by a bright ($\sim 14\,\mathrm{mag\,arcsec^{-2}}$) background that is variable both spatially and temporally. A carefully designed observing strategy and data reduction is therefore required to achieve reliable background subtraction.

In taking the data, we apply a large-scale dither pattern, with the target first imaged near the detector center, and then moved towards the corners of the FOV in a clockwise pattern. Before and after every on-target exposure we perform an off-target exposure, and the whole pattern is repeated several times. This results in ~ 25 science frames and twice the number of sky frames. With this strategy, we obtain a reliable reconstruction of the background, since every part of the detector remains unoccupied by the relatively large target galaxy at least in a sizeable fraction of the exposures, and we can simul-

[2]PyFits is a product of the Space Telescope Science Institute, which is operated by AURA for NASA.

[3]The WIYN Observatory is a joint facility of the University of Wisconsin-Madison, Indiana University, the National Optical Astronomy Observatory and the University of Missouri.

TABLE 1
The Megamaser Sample

Galaxy	RA	Dec	D [Mpc]	Hubble Type	L_H [$10^{10}\,L_{\odot,H}$]	R_e [kpc]	$t_{\rm exp}$ [s]	obs. date	wide-field imaging
(1)	(2)	(3)	(4)	(5)	(6)	(7)	(8)	(9)	(10)
IC 2560	10 : 16 : 18.7	−33 : 33 : 50	41.8	(R)SB(r)b	13.2	4.0	422	2010-10-23	UVIS-F814W LCO DuPont/Tek-I
NGC1194	03 : 03 : 49.1	−01 : 06 : 13	52.0	SA0+	5.75	2.8	422	2011-11-23	APO3.5m/NIC-K
NGC2273	06 : 50 : 08.6	+60 : 50 : 45	26.0	SB(r)a:	3.47	1.4	422	2011-01-31	APO3.5m/NIC-K
NGC2960	09 : 40 : 36.4	+03 : 34 : 37	71.0	Sa?	7.76	1.9	422	2011-06-14	APO3.5m/NIC-K
NGC3393	10 : 48 : 23.4	−25 : 09 : 43	53.6	(R)SB(rs)	9.33	2.5	422	2011-11-11	UVIS-F814W
NGC4388	12 : 25 : 46.7	−12 : 39 : 44	19.0	SA(s)b:	3.09	1.4	422	2011-06-08	APO3.5m/NIC-K
NGC6264	16 : 57 : 16.1	−27 : 50 : 59	136.0	S?	8.71	4.0	422	2011-07-30	APO3.5m/NIC-K
NGC6323	17 : 13 : 18.1	−43 : 46 : 57	105.0	Sab	8.71	2.5	422	2011-09-01	WIYN/WHIRC-K
UGC03789	07 : 19 : 30.9	−59 : 21 : 18	50.0	(R)SA(r)ab	5.37	2.2	422	2011-09-06	APO3.5m/NIC-K

Note. — Columns (1-5) give the galaxy name, coordinates, distance in Mpc, and Hubble Type (RC3 catalog, de Vaucouleurs et al. 1991). Column (6) gives the the galaxy (total) H-band luminosity in units of $10^{10}\,L_{\odot,H}$, and column (7) the galaxy effective radius in kpc. Both L_H and R_e values result from our imaging data and multi-component fitting. The inner parts are imaged with *HST*/WFC3 in the F160W filter, with exposure times in seconds, and dates given in columns (8) and (9). In order to get constraints on the outer parts of the surface brightness that did not fit on the WFC3-IR FOV of $70\farcs4 \times 62\farcs6$, we also include data that we obtained on telescopes and instruments given in column (10).

taneously monitor the evolution of the background level and the two-dimensional structure in the background.

Using the dark and twilight flat frames, we identify bad pixels, and mask them in all subsequent exposures. After flatfielding the raw frames, a background pattern (see bottom-left panel in Figure 1) persists, as well as a much weaker, near-random pattern that corresponds to the expected pattern from variable non-uniform sky (atmospheric) emission. We ascribe the time-invariant portion of the residual background pattern to a discrepancy between the twilight flatfield image and the response of the detector to night sky illumination. Therefore we need to subtract the mean background pattern that persists after the frames have been flatfielded with the twilight flat. The standard alternative, dome flatfield images, provides a significantly poorer approximation to the nighttime sky (and flatfield) pattern. We addressed the residual time-invariant background pattern by flatfielding using a "superflat", which is a flatfield image constructed from the images taken over the course of the night. However, we found no improvement in the background subtraction using this method. To achieve the required S/N in the flat requires summing over most of the images over the course of the night, but there is sufficient change in the background pattern with time that residual patterns remain after flatfielding with the "superflat".

We construct an image of the mean residual background pattern as follows. We first normalize each frame by its mean background, and then take a pixel-by-pixel median over all the normalized frames, including all sky frames, and also on-target frames when the target covers less then 40% of the FOV. By averaging so many frames, we can remove additional bad pixels and astronomical sources, while retaining a high S/N in the averaged sky image. For masking of intervening objects we use source detection by the SExtractor software, combined with by-hand masks for bright stars and extended objects (galaxies). The mask for measuring the mean must be a combination of the masks of all frames, in order to avoid level offsets caused by large masked objects covering different parts of the detector on an uneven background. We subsequently subtract from each frame this "sky structure" image, scaled by the frame's background level.

This procedure is very effective at removing the residual near-constant background pattern (see Figure 1, bottom-right panel). However, it requires that every part of the detector is uncontaminated by celestial sources, which renders the on-target frames unusable in some galaxies. For those fields, the sky pattern can still be reconstructed using the interleaved sky exposures. Naturally, for a successful background subtraction we also need to measure the average sky level, apart from its spatial structure. For this, we use on-target measurements rather than the pure sky frames because the mean sky level fluctuates by $\sim 1\%$ ($\sim$ 16-17 mag arcsec^{-2}) even on timescales of a minute or less.

After subtracting sky structure and level, we coadd our frames. To that end, we re-detect all astronomical sources using SExtractor, use the resulting source catalogs to compute a 3rd-order polynomial astrometric solution of the field distortion and true pointings (different from the coordinates found in the headers by $\sim 1''$ on average), and finally re-project and coadd the frames using SWarp.

After this first-pass sky subtraction and co-addition, we have an image that is much deeper than any individual frame and hence offers a much better opportunity to mask faint sources (stars and small background galaxies), as well as low-level extended "wings" of bright stars and large galaxies. It also allows a better visual identification of large galaxies in the field. In fact, faint but previously unmasked source flux does sometimes leave visible imprints in the sky-subtracted frames, which propagate to the first-pass stack. After obtaining the improved masks from the deep first-pass stack, we repeat the above procedure, this time using the deep mask projected onto the individual frames. This improves the sky structure model and removes remaining artifacts in the background.

2.4. *Combining* HST *and ground-based data*

We combine *HST* ($H-$band) with ground-based images, in order to provide sufficient constraints during the fitting process. We experimented and found that most of the real structures present in our galaxies cannot be analyzed reliably with GALFIT when either the ground-based or *HST* data are taken alone. For the medium-resolution (median FWHM $\sim 0\farcs8$) ground-based data the cause is

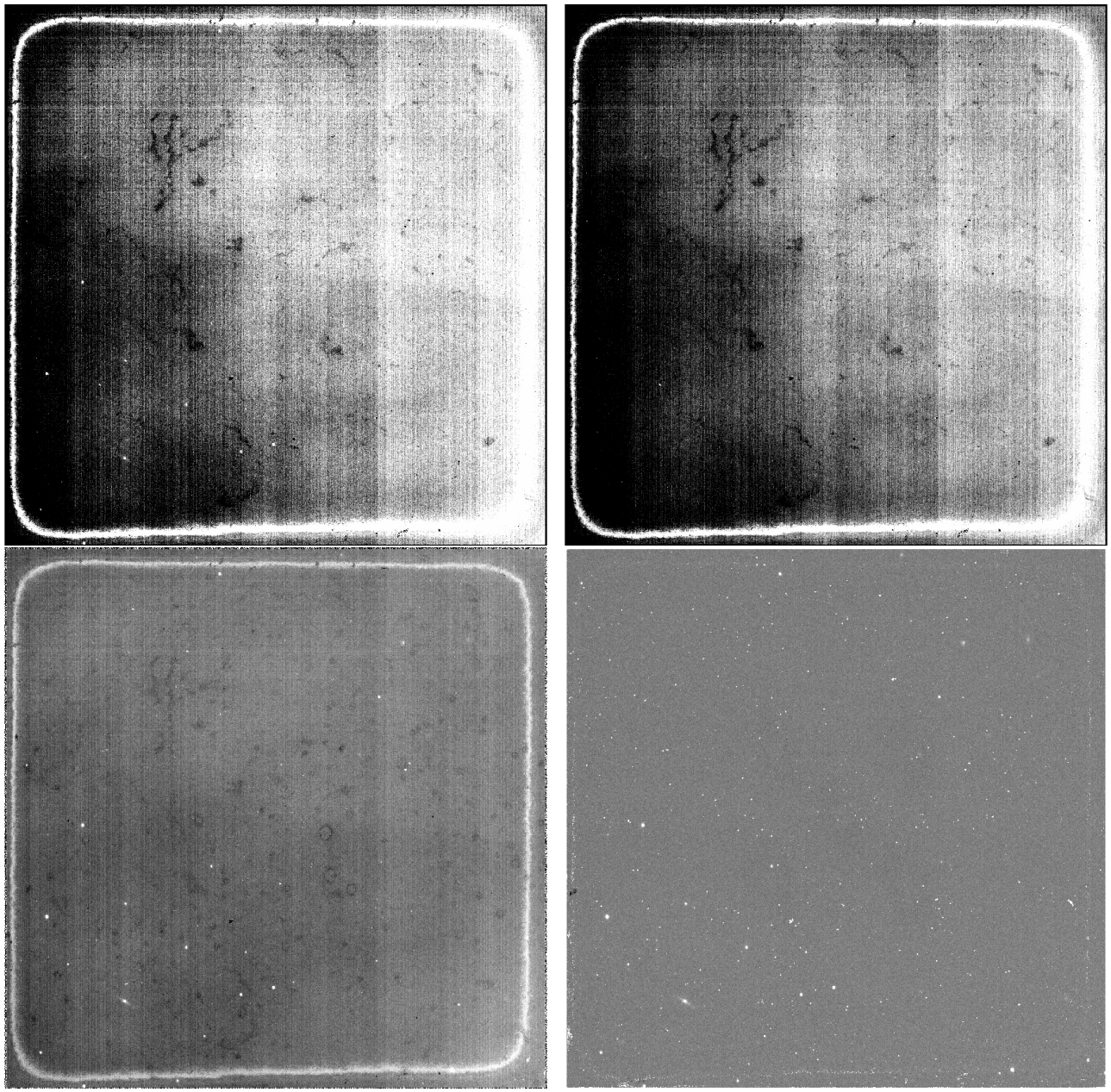

FIG. 1.— Example of the need for subtracting the residual common sky pattern after flatfielding, from APO data. Top left: raw exposure, top right: twilight flatfield stack. The structure remaining after dividing by the flatfield image is evident (bottom-left panel), as well as the improvement after subtracting the mean sky pattern (the mean of all frames of the OB, after source masking, bottom-right). Random temporal sky pattern variation is negligible and not visible at this contrast. The same relative greyscale was used in all panels (±10% of the mean).

clear: small-scale structures are not resolved, and a basic bulge plus disk model is the only feasible model in most cases. However, the *HST* data alone are also insufficient: the lack of data at large scales prevents a convergence of more complex models. In surface-brightness profile modeling, the need for large-scale information on both the galaxy light distribution and the background has been discussed in Peng et al. (2010).

We combine each co-added *HST* $J-$ or $H-$band image with ground-based K-band data by first scaling the former to the latter: we measure the radial surface brightness profiles in both, and pick by eye the part of the profile in which both overlap and exhibit the same shape. The matched profiles (Figure 2) show that $J-$ and $H-$band profiles are very similar to the $K-$band profiles, except in the very center (active galactic nucleus or AGN light and dust) and around spiral arms (dust and young stellar populations), and the similarity of the profiles justifies our approach. After rescaling and background-subtracting the *HST* images using a linear fit to the profiles, $< HST >=< \mathrm{bkg} > + < \mathrm{scale} > * < \mathrm{ground} >$, we resample the ground-based image stack onto the *HST* WCS and replace $K-$band by *HST* data where they exist. Similarly, we re-project, scale, and replace the noise and weight maps of $K-$band stacks with *HST* data where available.

3. IMAGE FITTING

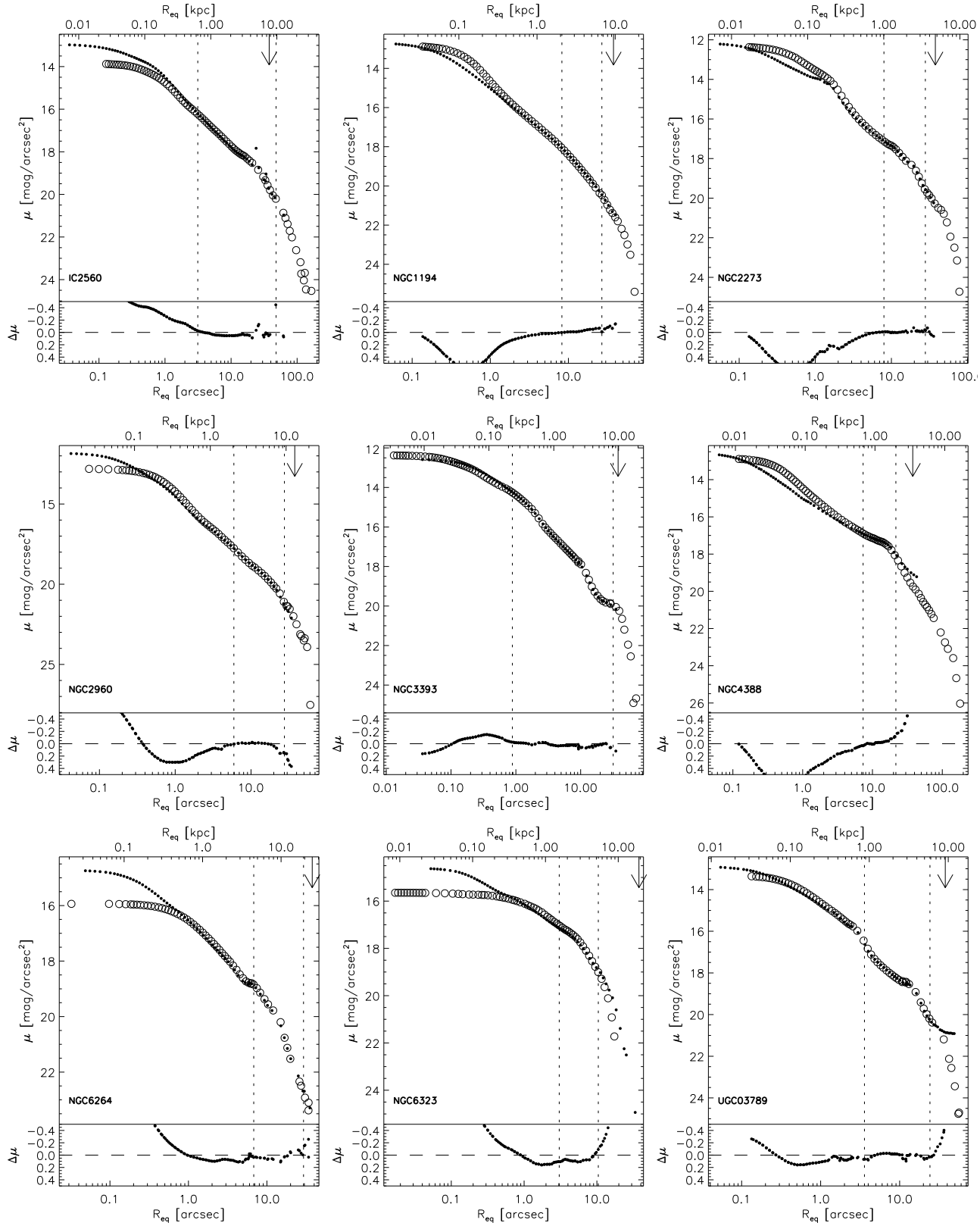

FIG. 2.— Comparison of wide-field (open circles) and *HST*/WFC3-F160W (filled dots) surface brightness profiles μ, plotted against equivalent circular radius, $R_{eq} = \sqrt{ab}$. The wide-field data are generally deep ground-based K-band images, except in NGC3393 (*HST*/WFC3-UVIS F814W). In IC2560, the filled circles show F160W combined with *HST*/WFC3-UVIS F814W data, and open circles ground-based LCO-100 I-band data. The profiles were matched by a linear fit (*HST* background level and flux scaling) using a radial range chosen to minimize color gradients (dotted vertical lines). The arrow indicates the radius outside of which we replace the *HST* with the wide-field data. Residuals of *HST* minus wide-field data are plotted in the lower parts of the figures, exposing $H-K$ (or $H-I$) color variations and, in particular, how much better *HST* resolves the nuclear region.

3.1. *Decomposition philosophy*

Although there is considerable interest in the correlations between BH mass and bulge luminosity or mass, there are few works that examine bulge masses in spiral galaxies with dynamical BH masses (they include Gadotti 2008; Hu 2008; Sani et al. 2011; Kormendy & Ho 2013). Often, spiral galaxies are excluded due to the difficulties in identifying robust bulge parameters (e.g., McConnell & Ma 2013). For one thing, the nuclei of spiral galaxies contain gas, dust, and ongoing or recent star formation (e.g., Carollo et al. 1997). These alone complicate the task considerably, since it is difficult to determine the true bulge parameters or mass-to-light ratio. However, it is even more difficult to determine exactly what bulge means in the context of these galaxies.

All of our galaxies contain a large-scale disk, and all show a steepening of the profile towards the center - a "bulge" by the most general definition. These central light excesses, however, show a wide range of physical properties, often more similar to disks than to classical bulges and elliptical galaxies: they are flattened like disks, tend to be fitted by an exponential (Andredakis & Sanders 1994) or Sérsic (1963) with low index (generally $n < 2$, see Fisher & Drory 2010), they show bars, dust, or spiral arms as disks do, and they have recent or ongoing star formation like disks (Carollo et al. 1997, and the review in Kormendy & Kennicutt 2004).

Together these attributes are interpreted as evidence that the central light excess or bulge region is being built up slowly by secular, gas-rich processes such as bar or spiral arm transport. To distinguish these components from kinematically hot systems without gas or young stars (e.g., elliptical galaxies) these systems have come to be known as "pseudobulges," while bulges that have the characteristics of ellipticals are called "classical bulges". Because the classification of a bulge depends on how it formed, it is certainly possible that some late-type galaxies contain both a pseudo- and classical bulge component, with the former having low mass-to-light ratios and thus dominating the light (Nowak et al. 2010; Erwin et al. 2015). Thus, we first decompose these different components (e.g. Weinzirl et al. 2009; Laurikainen et al. 2010; Läsker et al. 2014a), and then ask which are of interest in the context of BH-bulge scaling relations.

We take the following dual approach. We first consider a "basic" model, comprising only a bulge and a large-scale disk, plus a nuclear point source if it can be included[4]. In the basic fit, the small-scale components are mostly fitted by the "bulge" component and only to a small degree accounted for by the disk component. Therefore, the magnitude of this "basic bulge" represents an approximate upper limit to the true (classical) bulge magnitude.

With a basic model in hand, we construct a more complete model, including structures on small scales, which may help us isolate a bulge component. We simultaneously model any central bars, rings, or disks, and look for an additional light component that is rounder and more centrally concentrated than the outer disk. If there is one, we call this the "classical" bulge. In the future, we will improve these decompositions by combining spatially resolved kinematics (e.g., Greene et al. 2014) with our *HST* imaging.

[4] i.e., if the bulge+disk model (without the point source) does not already overestimate the central surface brightness

3.2. *Fitting*

We now describe our two-dimensional parametric modeling in more detail to model the central components in each galaxy.

Working in two dimensions allows us to make full use of the information contained in the data to reduce degeneracy, and is an important advantage over one dimensional modeling for the complex galaxy structures considered here. Each two-dimensional model component is corrected for the effects of the point-spread function (PSF), and then the parameters of the model are optimized using χ^2 minimization with the publicly available code GALFIT3 (Peng et al. 2010). At minimum (our "basic" model), the models include a bulge, a large-scale disk, and a central point source model the AGN and/or an unresolved nuclear star cluster in those cases where the bulge+disk model does not overestimate the cnetral light already. In all of the megamaser host galaxies more components are present. We identify these based on visual identification in the science image, the residual image of the basic model, and the radial profiles of surface brightness (SB), ellipticity (e) and position angle (PA).

An accurate PSF model is an important ingredient in the modeling. We construct a PSF model by combining a number of stars in our images, which gives us a model of the PSF that is local both in space and in time to the observations of the galaxy. In the Appendix we describe various PSF comparisons to show that we are recovering the PSF accurately (see Figure 27 in the appendix). Similarly, masking of intervening objects, background subtraction, availability of a sufficiently large image area around the target galaxy, and an appropriate noise image impact the feasibility and accuracy of the fit results. We describe these ancillary data in the appendix, Section B.

We follow wide-spread convention in prescribing the radial surface-brightness profile of Sérsic form for the bulge, as well as an exponential profile for the large-scale disk. The Sérsic profile is defined as

$$I(R) = I_e \exp\{-b_n[(R/R_e)^{1/n} - 1]\} \quad (1)$$

in terms of three independent parameters: the effective radius R_e along the semi-major axis (SMA), the surface brightness I_e at R_e, and the Sérsic index n. The value of b_n is numerically determined such that the area inside of R_e contains half of the total flux. The large-scale disk is modeled with an exponential profile, which is equivalent to a Sérsic profile with $n \equiv 1$ and the scale radius (R_s) is related to $R_e = b_{n=1}R_s = 1.678R_s$. The two-dimensional surface brightness profile follows from (1) by additionally specifying the center (x_0, y_0), axis ratio ($q = 1 - e$), and PA of the elliptical isophotes. In GALFIT, I_e is replaced by the profile surface brightness magnitude, $\mu_{\rm ser} = \mu_0 - 2.5 \log F_{\rm ser}$, where μ_0 is the photometric zero point, and $F_{\rm ser}$ the total flux, which is calculated by

$$F_{\rm ser} = 2\pi R_e^2 q I_e n b_n^{-2n} e^{-b_n} \Gamma(2n) \quad (2)$$

with $\Gamma(2n) = \int_0^\infty x^{2n-1}e^{-x}{\rm d}x$ the Gamma function.

The full image model is the sum of the fluxes from all included components. Apart from the two-dimensional

PSF for the AGN, we exclusively employ profiles of Sérsic form, albeit with fixed Sérsic index if an exponential ($n \equiv 1$) or Gaussian ($n \equiv 0.5$) profile is desired. We sometimes use profile modifications, including Fourier modes, truncations, coordinate rotation, and bending modes. For more details on these perturbations see Peng et al. (2010).

In Table 2, we list a selection of the resulting GALFIT parameters: component magnitudes, sizes (bulge R_e and disk R_s), and the bulge Sérsic index. Total apparent magnitudes are also listed (column 2).

3.3. *Detailed decompositions*

It is not trivial to determine the number and type of components to fit to these many-component profiles in the face of possible profile mismatches and parameter degeneracies. We generally begin with a very simple two-component model, and then examine the fit residuals, the ellipticity, and the PA profile to see whether additional components are warranted. We also refit, adding components in a different order, to be sure that GALFIT robustly converges on the same fit. The most challenging task is to find the most probable and physically realistic model while retaining acceptable alternatives for the systematic uncertainty estimate. Compared to this systematic (modeling) uncertainty, the formal parameter uncertainties from the χ^2 derivatives are very small.

In the following subsections, we describe the most common subcomponents and how we identify them. Each is demonstrated graphically in Figure 3.

3.3.1. *Nuclear disks*

Nuclear disks have a scale of $\lesssim 100$ pc. They are intrinsically flattened, which is evident when they are observed nearly edge-on, and may be misaligned with the large-scale disk (e.g. NGC4388). There is kinematic evidence for a nuclear disk that we also recognize photometrically in the case of both NGC2273 (e.g., Barbosa et al. 2006) and NGC4388 (Greene et al. 2014). Even when seen nearly face on, nuclear disks are distinguished by their relatively sharp boundaries and occasionally inset spiral arms (e.g., IC2560). Since they occur in the central regions of the galaxy and have high surface brightness, they tend to bias larger scale components to higher n and smaller size if not modeled separately. We model nuclear disks using a Sérsic profile, typically with $n \leq 1$. Sometimes these disks are delineated by starforming regions arranged in a ring (NGC2273, UGC3789) and we model them accordingly (see 3.3.3). We include a nuclear disk or ring in five of the nine target galaxies (IC2560, Fig. 9; NGC2273, Fig. 13; NGC2960, Fig. 15; NGC4388, Fig. 19; UGC3789, Fig. 25).

3.3.2. *Bars*

A bar is present in the images of NGC2273 (Fig. 14), NGC3393 (Fig. 18) and UGC3789 (Fig. 26). The classic signatures of a bar are a simultaneous increase in ellipticity and flat PA over the radial range where the bar dominates the light (e.g., Menéndez-Delmestre et al. 2007), followed by a sharp drop in ellipticity at the outer radius where the bar ends. In certain cases, if the galaxy is at high inclination or the bar is pointing towards us, then it is more challenging to uncover, yielding an ambiguity in the final decomposition (see for instance NGC1194, Fig. 11). Nuclear bars, similar to nuclear disks or rings, can particularly bias the light profile of any underlying classical bulge component. Because bars form only in disk structures, we exclude them from any classical bulge estimate.

We model all bars as a Sérsic profile with free n, and find them all to have $n \lesssim 1$ as expected. GALFIT offers the (modified) Ferrer profile, which becomes zero outside of the truncation radius and is an alternative profile suited for bars due to its flat center and steep outer profile (Peng et al. 2010). It does not provide an improvement of the fit over Sérsic profiles in our data. We do allow a 4th-order Fourier mode to fit the boxiness of the isophotes of the bar.

3.3.3. *Rings*

A ring is prominent in NGC3393 (Fig. 17) and NGC6323 (Fig. 23). Three rings are present in NGC2273 (see Fig. 13, and Erwin & Sparke 2003) and UGC3789 (Fig. 25). The inner rings in each galaxy are associated with a nuclear disk (see 3.3.1). In NGC2273 we refrain from modeling the outermost ring, due to its low surface brightness. Nuclear rings generally bias the parameters for other nuclear components (e.g., bars and bulges) to fainter and more compact (lower n) profiles if not accounted for (UGC3789 is an example). At larger scales, omitting rings (or spiral arms) usually biases the disk to higher flux or larger R_s. We generally model rings as an inner truncation multiplied by a Sérsic profile with fixed $n = 0.5$ (a Gaussian profile). The compactness of this profile is suitable to model the steep decline of the profile. We also test using an exponential profile ($n = 1$), but find that it does not improve the fit. Finally, we never fit a nuclear disk and nuclear ring component simultaneously, as they are degenerate.

3.3.4. *Spiral arms*

We detect and fit spiral arms in six out of our nine targets. Spiral arms can be modeled in GALFIT using coordinate rotation, which changes the PA as a function of radius. Fitting spiral arms is not merely a cosmetic measure, but also impacts the best-fit parameters of the large-scale disk. Spiral arms often span a limited radial range in the disk, and thus we use an inner truncation to limit their profile towards small radii. In four cases (IC2560, Fig. 9; NGC2273, Fig. 13; NGC3393, Fig. 17; and NGC4388, Fig. 19), the arms are tightly wound or partially dust-obscured. These prove difficult to model with a free-parameter rotation function, so we model them as a ring. This leaves only two galaxies (NGC6264, Fig. 21; NGC6323, Fig. 23) where we used a rotation function for the spiral component. The remaining three galaxies have no significant spiral structure that could impact our fits. The Sérsic index of the arm model is fixed during the fit due to degeneracy with the parameters of the required inner truncation. We tested values of $n = 0.5$, 1.0 and 1.5, and pick the value that leads to the smallest residuals.

3.3.5. *Envelopes*

Some of our targets (IC2560, Fig. 9; NGC1194, Fig. 11; NGC4388, Fig. 19; and UGC3789, Fig. 25) show a

TABLE 2
GALFIT BEST-FIT PARAMETERS OF GALAXY IMAGE MODELS

Galaxy	Total		Bulge						Disk				Psf		Additional components
	m_t (2)		m_b (3)		R_e [″] (4)		n (5)		m_d (6)		R_s [″] (7)		m_p (8)		mag and type (9)
	bas	bul	bas	bul	bas	bul	bas	bul	bas	bul	bas	bul	bas	bul	
IC2560	8.83	8.62	10.71	11.50	0.99	0.59	2.9	1.5	9.04	9.65	6.2	5.6	–	16.33	13.44, 11.77, 11.72, 9.57 ND, XBul, SpRing, Env
NGC1194	9.90	10.01	10.22	12.04	4.6	1.8	6.8	3.2	11.39	13.50	3.5	6.9	–	17.30	12.75, 10.32 Bar, Env
NGC2273	9.13	9.04	10.96	10.81	0.25	0.33	1.0	2.0	9.36	9.75	1.4	2.2	14.84	15.24	12.85, 11.30, 11.31 NR, Bar, Spir
NGC2960	10.36	10.35	11.24	11.01	0.68	15.8	4.0	1.0	12.02	10.89	3.1	2.1	–	14.84	12.44 ND
NGC3393	9.46	9.55	10.19	11.20	1.6	0.62	3.5	2.3	10.24	10.77	5.5	1.6	17.63	15.94	13.65, 13.01, 10.57 Bar, SpRing, Env
NGC4388	8.59	8.49	10.57	10.28	0.9	1.2	3.8	2.2	8.79	9.72	2.4	1.7	14.78	14.80	13.00, 10.43, 9.80 ND, SpRing, Env
NGC6264	11.64	11.64	12.97	14.44	3.2	0.65	3.1	1.3	12.02	12.67	5.6	5.1	18.48	18.04	13.59, 12.72 Bar, SpRing
NGC6323	11.08	11.08	14.05	14.14	0.75	0.66	1.2	1.1	11.16	11.82	4.2	3.4	17.45	17.40	13.05, 12.49 Ring, Spir
UGC03789	9.98	10.00	11.47	11.50	0.51	0.8	1.5	3.3	10.31	11.07	3.1	2.3	15.89	16.63	13.25, 13.66, 12.58, 11.76 Bar, NR, Ring, Env

NOTE. — In columns (2)-(8) we list $H-$band galaxy total magnitude, bulge magnitude, effective radius and Sérsic index, disk magnitude and scale radius, and the magnitude of the central point source. Each of those columns contains two values: the first one ("bas") derived from the basic decomposition (bulge, disk, and the central point source if it could be fitted), followed by the results of the full model ("bul") which includes significant additional components and yields our best estimate of the "classical" bulge parameters by virtue of separating non-bulge and pseudobulge components. The additional components' magnitudes of the full model are given in column (9), along with their morphology in abbreviated form: "NR" for nuclear ring, "ND" for nuclear disk, IDisk for inner disk, "XBul" for X-shaped/boxy bulge, "Bar", "Ring" for medium-large scale ring, "Spir" for spiral modified by rotation, "SpRing" for spiral arms that nearly form a ring (no coordinate rotation fitted), and "Env" for envelope. See table 3 for a short, and Section 3.3 for a detailed presentation of those morphologies and classification criteria.

TABLE 3
MORPHOLOGICAL TYPES OF NON-STANDARD COMPONENTS

Abbreviation	Type	description and criteria
NR	nuclear ring	ring (see below) of $\lesssim 500$ pc size, similar to nuclear disk with inner truncation
ND	nuclear disk	$R_e \lesssim 500$ pc Sérsic profile with $n \lesssim 1$, often not aligned with galaxy major axis
IDisk	inner disk	flattened as the main disk but smaller (~ 1 kpc); only in NGC2960 where it exhibits spiral arm substructure
XBul	X-shaped/boxy bulge	Sérsic with $1 \lesssim n \lesssim 2$, $q \approx q_{\rm disk}$ and $R_e \sim 1$ kpc; identified in IC2560
Bar	bar	Sérsic $n < 1$, generally elongated and often misaligned from major axis, in NGC1194 probably seen down its long axis
Ring	ring	Sérsic with inner truncation and $n = 0.5$ fixed at intermediate and large $\gtrsim 1$ kpc scales
SpRing	spiral/ring	shows up in the profile as a ring but also spiral structure (tight winding) in the image, n fixed to 0.5 or 1.0
Spir	spiral	Sérsic profile with coordinate rotation to emulate spiral arms, sometimes fixed $n = 0.5$ or $n = 1$
Env	envelope	extended disk and/or a halo depending on ellipticity ϵ, accounts for flux excess above the main disk at large radii ($\gtrsim 5$ kpc), Sérsic n varyingly fixed or free

NOTE. — We list here the abbreviations and morphologies of non-standard (beyond bulge, disk and PSF) components we used while fitting GALFIT models to our galaxy images. Detailed descriptions of the morphological types, and the criteria we used to identify/classify them, are presented in Section 3.3.

profile extension above the large-scale disk that sets in at > 5 kpc scales (see Figure 1). These envelopes are identifiable visually on the image, and are accompanied by a change in axis ratio $q = b/a$ coincident with a break in the surface brightness profile, as seen in so-called type III upbending or anti-truncated disks (e.g., Erwin et al. 2005; Pohlen & Trujillo 2006; Erwin et al. 2008). They are sometimes rounder than the disk, like an outer halo, but are often flattened and best fit by an exponential profile. Inclusion of the envelope typically impacts the bulge parameters only weakly, due to the large difference in scale. However, it may significantly contribute to the total galaxy magnitude (IC2560, NGC4388).

3.4. *Systematic uncertainties*

The uncertainty in our fitting is dominated not by measurement error but rather by systematic uncertainty. In general, degeneracy or deficiency in our modeling dominates the uncertainty, but the background level can also play a significant role in some cases (e.g., NGC4388).

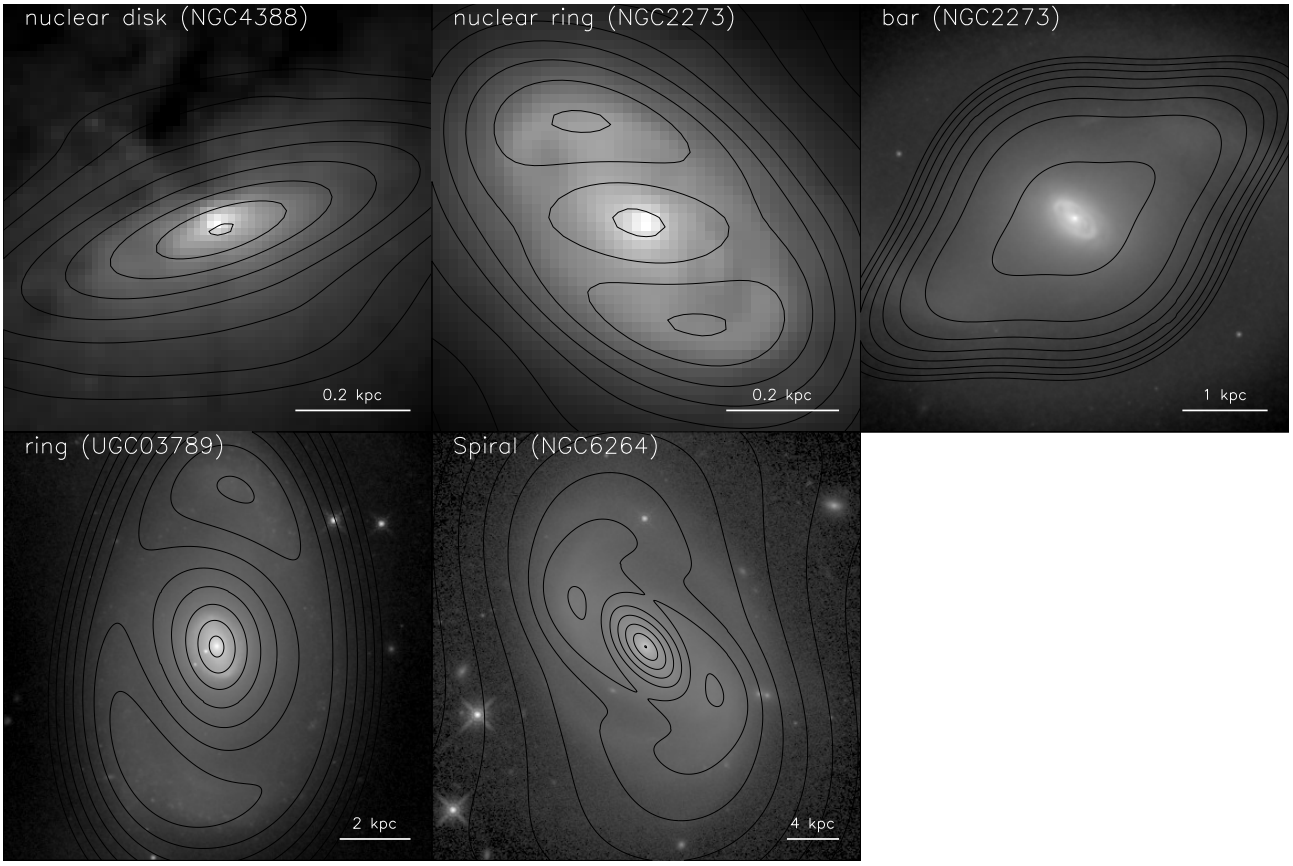

FIG. 3.— Examples of observed and GALFIT-modeled morphological components in our sample. Shown are *HST*/WFP3-F160W image cutouts, with contours of their model counterparts overlaid. For detailed descriptions of the component types and the fitting process, see Section 3.3 and the appendix. The offset of the model contours with respect to the brightest point in the image seen in the small-scale nuclear disk and nuclear ring examples is a result of constraining all model component center coordinates, except those of the central point source, to a common value during the fit.

TABLE 4
SYSTEMATIC UNCERTAINTIES

Galaxy	Bulge								Disk		PSF	
	m_b				$\log(R_e/\,\mathrm{kpc})$		$\log n$		m_d		m_p	
	psf	rsc	mod	tot	mod	tot	mod	tot	mod	tot	mod	tot
IC2560	0.00	0.02	0.30	0.30	0.10	0.10	0.17	0.18	0.75	0.75	0.13	0.17
NGC1194	0.06	0.08	0.54	0.54	0.40	0.42	0.11	0.11	0.19	0.45	8.37	8.37
NGC2273	0.00	0.04	0.34	0.34	0.19	0.19	0.16	0.17	0.14	0.30	0.39	0.40
NGC2960	0.11	0.02	0.08	0.14	0.06	0.08	0.14	0.17	0.02	0.05	0.29	0.31
NGC3393	0.00	0.06	0.11	0.13	0.10	0.12	0.13	0.16	1.07	1.07	0.23	0.28
NGC4388	0.00	0.31	0.51	0.60	0.11	0.32	0.06	0.24	0.45	0.79	0.12	0.19
NGC6264	0.02	0.43	0.93	1.03	0.35	0.43	0.15	0.16	0.28	0.30	0.17	0.24
NGC6323	0.01	0.51	0.52	0.73	0.23	0.55	0.21	0.47	0.32	4.02	0.47	0.54
UGC03789	0.03	0.12	0.41	0.43	0.18	0.23	0.06	0.08	0.21	0.22	0.14	0.20

NOTE. — Systematic uncertainties for five parameters of the full decompositions: the bulge magnitude, logarithmic effective radius, and Sérsic index (m_b, $\log(R_e/\,\mathrm{kpc})$, and $\log n$), as well as the disk magnitude (m_d) and magnitude of the central point source (m_p). Each total ("tot") systematic error is the sum of the errors resulting from PSF model ("psf"), background and flux scaling ("rsc"), and model ("mod") systematic uncertainties, added in quadrature. In general, the modeling uncertainty (number and profiles of the model components, see Section §3.4.1) dominates the total systematic error, which is why PSF- and background/scaling-related errors (Sections 3.4.2 and 3.4.3) are shown only for the most important parameter in our study, m_b.

3.4.1. *Modeling uncertainty*

In the previous subsection, and in the Appendix, we describe our general approach to finding the most suitable model for a given galaxy image. Even given the high spatial resolution and depth of our data, and the complexity of our models, the true structure of the galaxy may not be fully represented. Thus, our choice of number of components and boundary conditions leaves a systematic uncertainty in the parameters we are interested in. This systematic parameter uncertainty originating in the choice of model is separate from the random uncertainties that originate in pixel noise. The latter are directly provided by GALFIT and are completely subdominant to the systematic modeling uncertainties[5].

We take a pragmatic approach and consider a handful (usually 2-4) of alternative models to our chosen best-fit model that we consider acceptable. This way, we obtain several alternative values of the resulting bulge parameter of interest (chiefly the magnitude), and take their standard deviation as a systematic uncertainty estimate. These values are presented in Table 4. Typical systematic uncertainty estimates are a few tenths of a magnitude. We use these uncertainties with the other systematic uncertainties added in quadrature, to represent the measurement error in the derived bulge mass ($L_{\rm bul}$ and $M_{\rm bul}$) when investigating the $M_{\rm BH}-M_{\rm bul}$ scaling relation in §5.

3.4.2. *PSF uncertainty*

We use a PSF image that is the weighted average of 14 individual star cutouts, as we find them on the model-subtracted WFC3/IR F160W images. Using this averaged image instead of any particular (fixed) individual star cutout reduces random noise, finite sampling and centering errors, as well as (correlated) background residuals, which propagate to model parameter errors. We estimate the PSF-related uncertainty of any parameter p when fitted by a single PSF image to be $\sigma^{(i)}_{p,\rm PSF} = \frac{1}{N-1}\Sigma_{i=1,...,N}\, p_i$, where p_i is the fit result when using the i-th of N available individual PSF images. Then, the uncertainty in p when fitting with the combined PSF image is approximately $\sigma_{p,\rm PSF} = \frac{1}{\sqrt{N}}\sigma^{(i)}_{p,\rm PSF}$, akin to the uncertainty of individual measurements propagating to the uncertainty of the mean of measurements.

3.4.3. *Background uncertainty*

The background uncertainties in our combined *HST*+ground-based images largely stem from the matching of the *HST* data to the ground-based data. In the former, the sky is not well known because the galaxy fills the field of view. In contrast, the ground-based images have a wide FOV and a well-defined background.

Due to color gradients across the galaxy, the fitting of the sky offset and relative flux scaling of the *HST* data generally depends on the radial range of the surface brightness profile chosen to constrain the fit. We chose the fiducial range to minimize color gradients, but even in the optimal range, fluctuations from measurement noise or actual variations within the profile add uncertainty in the fitted sky offset and relative flux scaling. In order to estimate the resulting uncertainty to the sky offset of the *HST* data, we employ a "Jackknife" resampling method. In each realization, one of the N surface brightness measurements within the fiducial range is omitted, resulting in N sample realizations of the fitted offset, a_i. Then, the uncertainty in the *HST* sky level a is $\sigma_a = \frac{n-1}{n}\sum_{i=1} N(a_i - \bar{a})$. These background errors are listed in Table 4 in columns labeled "rsc".

[5] i.e by one to several orders of magnitude

3.5. *Colors and conversion to stellar mass*

In order to facilitate direct comparison with early-type galaxies, we attempt to mitigate the variability in mass-to-light ratio $\Upsilon \equiv M_\star/L$ by using the galaxy color. Since the variation in Υ with population properties and dust column density is decreased at NIR wavelengths, we choose F160W (nearly $H-$band) to measure the luminosity, and derive $\Upsilon_H \equiv M_\star/L_H$ based on optical colors. We use the color-Υ relation from Bell et al. (2003), which determines conversions between a single galaxy color and the galaxy Υ based on stellar population synthesis models and an assumed dust model. We also experimented with the two-color relations from Zibetti et al. (2009), but found that these conversions yielded unrealistically low Υ values for some of the most massive ellipticals in our comparison sample, for whom the color is very red (§3.6). We note that many systematic uncertainties remain in stellar population synthesis modeling, particularly regarding the contribution to the near-infrared light from asymptotic giant branch stars (e.g. Maraston 2005; Conroy et al. 2009; Kriek et al. 2010; Zibetti et al. 2013). It is possible that the Bell et al. (2003) mass-to-light ratios are overestimates at blue $g-i$ color because their models do not treat these later stages of stellar evolution (e.g. Roediger & Courteau 2015).

Since we have measured F435W (roughly $B-$band) and F814W (roughly I-band) magnitudes, we are closest in color to the $g-i$ conversions to $\Upsilon_{\rm H}$ from Bell et al. (2003). We derive a conversion between the *HST* colors and the Sloan Digital Sky Survey (SDSS; York et al. 2000) $g-i$ system using simple stellar population models from the Padova group (Marigo et al. 2008), including extinction in each band ranging from an A_V of 0 to 3. A tight linear relation is found (scatter of 0.05 mag) between the $g-i$ and $F438W-F814W$ color of

$$g-i = -0.443 + 0.738(F438W - F814W)\ . \quad (3)$$

Note that the $F438W$, $F814W$, $F160W$ and $H-$band magnitudes here are all in the Vega system, while the SDSS magnitudes are given in the AB system (Oke & Gunn 1983; Fukugita et al. 1996).

For both the basic and classical bulges we measure the bulge color by defining a radial range over which the given component dominates the total flux. Using the same aperture on both bands we can derive a color without performing full fits to each band. We ensure that PSF and AGN corrections are negligible by imposing a lower limit of $\gtrsim 2\,$pix ($0.26''$) on the semimajor axis of the aperture, corresponding to ~ 50 pc at the typical distance of 50 Mpc. The magnitudes for the entire galaxy (total) are measured from the total $H-$band magnitude within the WFC3-IR sky-subtracted image. We note that a more precise method to determine component colors would involve simultaneous fitting of images in multiple bands, but this analysis is outside the scope

TABLE 5
Bulge and total colors

Galaxy	$a_1['']$	$a_2['']$	$a_1['']$	$a_2['']$	$F435-814W$			$F814-160W$			$g-i$			$i-H$			$H-K$
	bul		bas		bul	bas	tot	bul	bas	tot	bul	bas	tot	bul	bas	tot	
IC2560	0.28	5.89	0.28	7.85	2.83	2.79	2.14	1.70	1.67	1.58	1.65	1.62	1.14	2.46	2.42	2.31	0.26
NGC1194	0.28	9.49	0.28	9.49	2.91	2.92	2.38	1.64	1.65	1.55	1.70	1.71	1.31	2.38	2.40	2.27	0.38
NGC2273	0.28	5.89	0.28	4.03	2.38	2.25	2.33	1.78	1.80	1.57	1.31	1.22	1.28	2.56	2.58	2.30	0.29
NGC2960	0.28	1.88	0.28	6.48	2.44	2.28	1.99	1.58	1.62	1.42	1.36	1.24	1.03	2.31	2.36	2.11	0.35
NGC3393	0.28	3.33	0.28	9.49	2.09	2.21	2.06	1.62	1.59	1.59	1.10	1.19	1.08	2.36	2.32	2.32	0.28
NGC4388	2.27	5.89	0.28	3.33	1.90	2.29	1.87	1.99	2.30	1.90	0.96	1.25	0.94	2.81	3.19	2.70	0.28
NGC6264	0.28	1.41	0.28	4.87	2.32	2.49	1.79	1.61	1.62	1.56	1.27	1.39	0.88	2.35	2.36	2.29	0.33
NGC6323	0.28	1.41	0.28	0.96	2.95	2.91	1.73	1.83	1.91	1.60	1.73	1.70	0.83	2.62	2.71	2.34	0.33
UGC03789	0.27	4.67	0.28	4.43	2.03	2.01	1.94	1.69	1.67	1.47	1.06	1.04	0.99	2.45	2.42	2.18	0.27

Note. — Bulge colors were measured in elliptical annuli bounded by a_1 and a_2 where the respective bulge component dominates, for the classical bulge ("bul") in our detailed decomposition and the Sérsic component in the basic Sérsic+exponential ("bas") decomposition. Meanwhile, total colors ("tot") were measured across the entire WFC3-IR FOV. Colors in the *HST*/WFC3 F435W, F814W and F160W (similar to Johnson B, I and 2MASS H) bands were converted to $g-i$ and $i-H$ as described in Section 3.5. The $H-K$ color is taken from the 2MASS catalog and measured within the 20 mag arcsec^{-2} isophote.

TABLE 6
Bulge and total mass-to-light ratios

Galaxy	$\log \Upsilon_H(g-i)$		
	bul	bas	tot
IC2560	0.11	0.10	0.02
NGC1194	0.12	0.05	0.05
NGC2273	0.05	0.03	0.04
NGC2960	0.06	0.04	-0.00
NGC3393	0.01	0.03	0.01
NGC4388	-0.01	0.04	-0.02
NGC6264	0.04	0.06	-0.03
NGC6323	0.12	0.12	-0.04
UGC03789	0.00	0.00	-0.01

Note. — Logarithmic H-band mass-to-light ratios ($\log \Upsilon_H(g-i)$) based on the Bell et al. (2003) prescription. The colors and decompositions on which these are based are listed in Table 5.

of our study and left to future work.

The inferred colors are listed in Table 5, along with the inner and outer annuli in which bulge colors were measured, both for the basic and classical bulges. Table 6 shows the $\Upsilon_H(g-i)$ that are derived from the Bell et al. (2003) models. The resulting $\log M_\star = \log L_H + \log \Upsilon_H$ are given in Table 7 and used in Section 5 regarding their correlation with $M_{\rm BH}$.

3.6. *Galaxies from the literature*

The primary sample of megamaser disk galaxies that we have fitted comprises nine disk galaxies of similar total stellar mass ($\sim 10^{11}\,M_\odot$). We wish to compare the results for our megamaser sample with a larger sample of galaxies spanning a range of masses, morphologies, and $M_{\rm BH}$. Many works have done two-dimensional image decomposition of the hosts of galaxies with dynamical BH mass measurements (e.g. Marconi & Hunt 2003; Sani et al. 2011; Vika et al. 2012; Beifiori et al. 2012). Here we rely on the $M_{\rm BH}-L_{\rm bul}$ data of Läsker et al. 2014b (L14 hereafter), since of all available previous work, their image analysis and quality are closest to our current study. We will discuss the comparison with other literature data in Section 6. The Läsker et al. 2014b sample comprises 35 galaxies of all Hubble types (4 spiral, 11 lenticular, and 20 elliptical galaxies) selected based on the availability of a reliable BH mass at the time the imaging data were taken. As in this paper, L14 provides total photometry, results based on basic bulge+disk models, and detailed decompositions, all based on homogeneous deep sub-arcsecond resolution $K-$band photometry. One of the galaxies in L14, NGC4258, is the prototypical megamaser disk galaxy. In the following, we will include NGC4258 in our sample of maser galaxies.

The sample from L14 is not identical to that of Kormendy & Ho (2013, KH13 hereafter). L14 includes the gas emission-based $M_{\rm BH}$ measurements of PGC49940 and Cygnus A, as well as NGC2778, NGC4261, NGC6251 and NGC7052, which were omitted by KH13 due to doubts about their $M_{\rm BH}$ reliability. Conversely, several $M_{\rm BH}$ measurements are included in KH13 that became available after the photometry for L14 was completed.

We again use the Bell et al. (2003) color conversions to calculate the stellar masses of the L14 sample. In this case, we do not have uniform *HST* color imaging for the objects. Instead, we use the SDSS photometry provided by the NASA-SDSS Atlas[6] (NSA hereafter; see, e.g., Blanton et al. 2011). Eighteen of the L14 galaxies have SDSS photometry. For these, we use the NSA single-component Sérsic fits for the galaxy magnitudes. We correct for galactic extinction (Schlafly & Finkbeiner 2011, retrieved using the NED[7]) and calculate a $g-i$ color. For the galaxies that are not in the NSA catalog, we use the mean $g-i$ color corresponding to the appropriate Hubble type: 1.17 mag (E), 1.15 mag (S0), and 1.0 mag (S).

The resulting $H-$band mass-to-light ratio $\Upsilon_H(g-i)$ ranges from 0.99 to 1.06, and thus any assumptions made based on the color likely have minor effects on the galaxy mass estimates. We calculate L_H from the L14 $K-$band magnitudes assuming the extinction-corrected 20 mag arcsec^{-2}-isophotal $H-K$ color of the 2MASS database. We find good agreement between the masses derived this way and the empirical relation of Cappellari (2013), which fitted a relation between dynamical mass and M_K. The dynamical estimates are 0.2 dex higher on average and related to our color-based masses by a correlation with slope 0.9 but with negligible scatter. The higher dynamical masses are consistent with the presence of dark matter within R_e increasing with increasing galaxy mass. Similarly, our color-based masses are consistent with the values given in KH13, which are only 0.06 dex more massive on average with a scatter of only

[6] http://www.nsatlas.org/
[7] http://ned.ipac.caltech.edu/

TABLE 7
Luminosities, masses, and sizes

Galaxy	$\log(M_{\rm BH}/M_\odot)$		$\log(L_H/L_{\odot,H})$			$(B/T)_L$		$\log(M_\star/M_\odot)$				$(B/T)_{M\star}$		$\log(R_e/\,{\rm kpc})$		
	val	err	bas	bul	tot	bas	bul	bas	bul	err	tot	bas	bul	bas	bul	tot
IC2560	6.40	0.40	10.29	9.97	11.12	0.18	0.07	10.40	10.08	0.14	11.14	0.22	0.09	-0.14	-0.33	0.60
NGC1194	7.82	0.05	10.67	9.94	10.76	0.74	0.15	10.72	10.39	0.20	10.81	0.74	0.38	0.58	-0.34	0.44
NGC2273	6.88	0.05	9.77	9.83	10.54	0.19	0.19	9.82	9.88	0.12	10.58	0.19	0.20	-0.70	-0.56	0.15
NGC2960	7.05	0.05	10.53	10.63	10.89	0.44	0.55	10.59	10.21	0.22	10.89	0.50	0.21	-0.28	0.73	0.29
NGC3393	7.49	0.12	10.71	10.30	10.97	0.51	0.21	10.72	10.31	0.05	10.98	0.51	0.21	0.14	-0.21	0.40
NGC4388	6.93	0.05	9.66	9.78	10.49	0.16	0.19	9.65	9.77	0.22	10.47	0.17	0.20	-0.11	-0.00	0.15
NGC6264	7.45	0.05	10.41	9.82	10.94	0.30	0.08	10.45	9.86	0.41	10.91	0.35	0.09	0.33	-0.26	0.60
NGC6323	6.96	0.05	9.75	9.72	10.94	0.06	0.06	9.87	9.84	0.27	10.90	0.09	0.09	-0.20	-0.24	0.40
UGC03789	7.05	0.05	10.14	10.13	10.73	0.26	0.25	10.14	10.13	0.15	10.72	0.26	0.26	-0.36	-0.12	0.34

Note. — BH masses ($\log M_{\rm BH}/M_\odot$) and their errors, bulge and total H-band luminosities ($\log L_H/L_{\odot,H}$), the ratio of bulge to total luminosity [$(B/T)_L$], stellar masses ($\log M_*/M_\odot$), and effective H-band radii [$\log(R_e/\,{\rm kpc})$] of our sample based on our GALFIT models. "Bas" indicates values based on basic bulge+disk(+point source) models while "bul" indicates those based on the full models of the classical bulge parameters. Bulge mass errors are based on the combined calibration, point-source and modeling uncertainties (see Table 4). Luminosities were converted to masses via the color-based $\Upsilon_H(g-i)$ (Bell et al. 2003), with colors measured on our *HST*/WFC3 F435W, F814W, and F160W images inside the appropriate apertures (bulge-dominated regions, see Section 4.4). The low B/T of the classical bulges conform to the late Hubble types of most of our targets. Alternative values for $\log M_{\rm BH}$ of IC2560 (6.54 ± 0.06, Yamauchi et al. 2012) and 6.643 ± 0.025, Wagner et al. in prep) based on VLBI data instead of the single-dish based $M_{\rm BH}$ adopted here have no appreciable effect on the scaling relations (Section 5).

0.15 dex. The least certain masses are for the spirals, where again the stellar population modeling harbors the most uncertainties. As one additional sanity check, we consider the five megamaser galaxies in the NSA catalog; deriving a stellar mass for them using the Bell et al. (2003) color relations and L_i, we find agreement at the 0.2 dex level, indicating that our stellar masses are all on the same relative scale.

In Section 5 we also consider three additional late-type galaxies: the Milky Way, Circinus, and NGC1068 (the megamaser host NGC4258 is already included in the L14 sample). In the first case the BH mass is known more precisely than any other (e.g., Ghez et al. 2008; Gillessen et al. 2009) but the bulge mass is quite difficult to determine. In the other two systems, the BH masses are based on megamaser disk modeling, but the fidelity of $M_{\rm BH}$ has been questioned. In the case of NGC1068, the rotation curve presented by Greenhill et al. (1996) is sub-Keplerian, perhaps because of a massive self-gravitating disk (Lodato & Bertin 2003). Circinus (Greenhill et al. 2003) may have an uncertain inclination (Ferrarese & Ford 2005).

The $M_{\rm bul}$ of the MW is taken from Kormendy & Ho (2013). Bulge magnitudes and masses for Circinus and NGC1068 are based on the work of Sani et al. (2011). We convert their apparent [3.6μm] magnitudes to $M_\star$ using their formula (5) in conjunction with σ_v (dynamical mass), or their equation (6) (empirical $M_\star - L_{3.6}$). For NGC1068, both $M_\star$ values of the bulge are nearly identical; for Circinus they differ by 0.5 dex so we use their mean ($\log M_{\rm bul}/M_\odot = 10.00$).

4. RESULTS: BULGE CLASSIFICATION

In this section, we investigate the general properties (luminosities, sizes, stellar masses) of the megamaser disk host galaxies. First we discuss whether or not our galaxies contain pseudobulges and then we attempt to determine whether or not they contain classical bulges. The nature of these components was discussed above in §3.1.

4.1. *Presence of Pseudobulges*

In §3, we described in detail the different physical components that are required to fully model the central regions of our megamaser disk galaxies. Because pseudobulges are defined by their formation history, not by their appearance, we are forced to consider what properties might indicate a pseudobulge. Here we mean primarily that we have identified structural components (nuclear rings or disks, as well as X-shaped/boxy bulges) that are associated with secular evolution. In the past it has been shown that Sérsic indices $n < 2$ correlate with the presence of pseudobulges (e.g., Kormendy & Kennicutt 2004; Fisher & Drory 2010), as well as low effective surface brightnesses at a given size (Gadotti 2009), and so we will also consider these specific criteria.

Below, we will go through the classification of each galaxy in detail (§4.4). Here we simply summarize our main finding: all but two of the galaxies show unambiguous signatures of secular evolution. We find sub-kpc disks, bars, or spirals in all galaxies with Hubble Type Sa or later (Table 1). We only identify one case (the lenticular galaxy NGC1194) with no evidence for a pseudobulge. Thus, we are fairly confident that the large majority of these galaxies do contain a pseudobulge component.

As emphasized by Erwin et al. (2015) among others, the presence of pseudobulge components does not preclude the presence of a rounder, older, kinematically hot classical bulge. From the point of view of BH scaling relations, it may well be that this classical bulge component matters most (Nowak et al. 2010). Thus, we have attempted to use our photometric fitting to identify such components. In the next section, we characterize these putative classical bulge components using color, shape, and structural information.

4.2. *Bulge Luminosities, Sizes, and Colors*

We derive galactic-extinction–corrected luminosities and linear sizes from the apparent magnitudes and sizes presented in Table 2, assuming $M_{\odot,H}$=3.32. As a reminder, the "basic" bulge is derived from a fit that includes just two or three components: disk, bulge and central point source where it can be fit. The point source may arise from the contribution of an AGN or be stellar in nature (e.g., NGC3384 Graham & Driver 2007; Ravindranath et al. 2001). Basic fits are indicated with the subscript "bas" in tables and figures. The "classical"

bulge component is the roundest and highest n component in the multi-component fit. Classical bulge components are indicated with subscript "bul" in figures and tables. Finally, the "total" magnitude and size are calculated as the sum of all components in our best fit multi-component model. We list the resulting parameters in Table 7, along with the bulge-to-total ratios (B/T) for the classical and basic bulge measurements.

In general, the basic bulges are both more extended (mean effective radius 0.8 kpc, ranging from 0.2 to 3.8 kpc) and more luminous ($0.5-5.1\times10^{10}\,L_{\odot,H}$) while the classical bulges, as they comprise only a single component of the galaxy central region, tend to be smaller (mean effective radius of 0.7 kpc, ranging from 0.3 to 5.4 kpc) and slightly fainter ($0.5-4.3\times10^{10}\,L_{\odot,H}$). Likewise the median bulge-to-total ratio (B/T) drops slightly from the basic bulge (30%) to the classical bulge (20%). Generally these B/T values are completely consistent with our expectations for early-type spirals (e.g., Simien & de Vaucouleurs 1986; Laurikainen et al. 2010).

The $g-i$ colors of the bulge and total galaxy are compared in Figure 4. As expected, the total color is always bluer than the bulge color, which avoids light from the large-scale disk component. We also check whether our detailed decompositions result in redder bulges than the basic decompositions. The latter tend to include central disks and rings, which are presumably younger and bluer. With our aperture measurements, however, classical bulges are not appreciably redder than the basic bulges. This similarity suggests that any color differences are too subtle for our crude method to discern, or that dust obscuration offsets real differences in the population.

4.3. *Bulge Shapes and Profiles*

As discussed in §3, we model a putative classical bulge component in addition to the exponential kpc-scale disk and any other identifiable morphological components, such as bars and nuclear disks. We attempt to understand the nature of the putative classical bulge components by examining their intrinsic flattening, Sérsic indices, and photometric scaling relations. Recall that in Figures and Tables, the classical bulge component is denoted as "bul".

4.3.1. *Flattening*

As one determining factor, we consider the flattening of the classical bulge component. A true classical bulge should be rounder than the disk. In contrast, if the light is dominated by a disky component, we expect to see a wide distribution of flattening $q = b/a$. The q of the disk and pseudobulge component should be similar, since secular evolution is supposed to bring material into the bulge from the disk. In practice, all of our classical bulge candidates have a higher projected axis ratio than the main disk, with the difference in bulge-disk q ranging from $0.2-0.5$.

4.3.2. *Sérsic n and the n − L relation*

The basic bulges are best-fit by Sérsic indices ranging from 1.0 to 6.8 (Table 2). The presence of compact disk-like central components (e.g., rings, disks, or bars) tends to drive up the value of n for the basic bulge components.

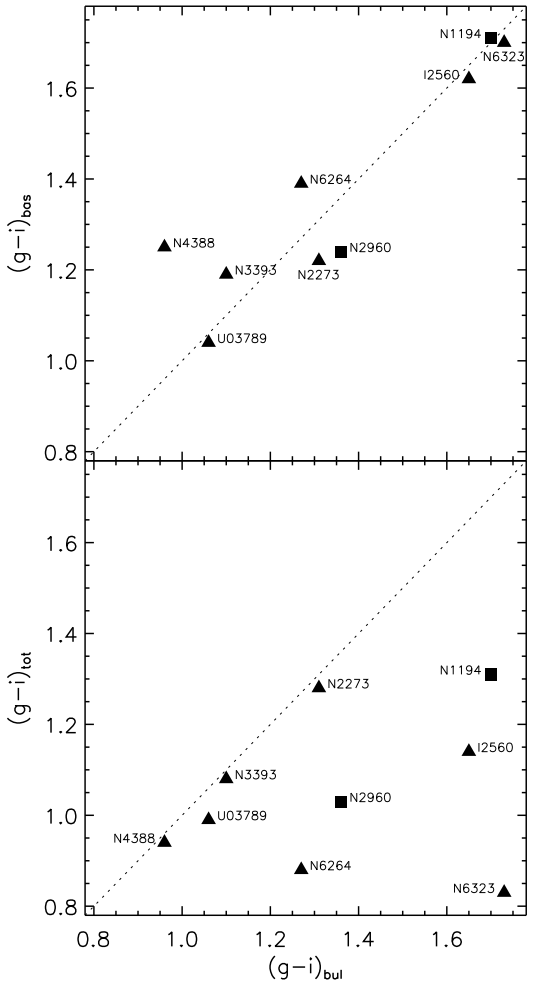

FIG. 4.— Comparison of the $g-i$ color (mag) of the basic bulge ("bas"; top panel) and total galaxy ("tot"; bottom panel) with the classical bulge ("bul"; full decomposition) for our megamaser sample, as drawn from Table 5. S0 galaxies are indicated with squares while spiral galaxies are triangles. All colors are measured in apertures: the region where the respective bulge component dominates in the GALFIT model, while total color is measured within the HST/WFC3-IR field-of-view. The colors of basic and classical bulge differ only marginally, but all bulge colors are redder than the total color, as expected.

When we perform more detailed decompositions, the effect of the nuclear components is mitigated, leading in general to lower n. For example, in the galaxy NGC4388, n drops from 3.8 to 2.2 when the highly inclined nuclear disk is modeled separately from the bulge. These classical bulge components have Sérsic $n \in [1.0, 4.4]$, with four of the nine classical bulge candidates having $n < 2$ (IC2560, NGC2960, NGC6264, NGC6323). The classical bulges in Erwin et al. (2015) also tend to have $n < 2$, suggesting that a high Sérsic index is not a hard requirement for low-mass classical bulges using our photometric definition of a rounder, extra-light component (§3.1).

Most of the classical bulge Sérsic indices in our late-type galaxies follow the relation with $L_{\rm bulge}$ in early-type bulges (Figure 5, left panels). Yet, the $n < 2$ bulges have lower n for their luminosity than classical bulges in general. NGC2960 is an interesting outlier. As suggested by Kormendy & Ho (2013), this galaxy may be a merger remnant. We find a kpc-scale disk in NGC2960, plus a

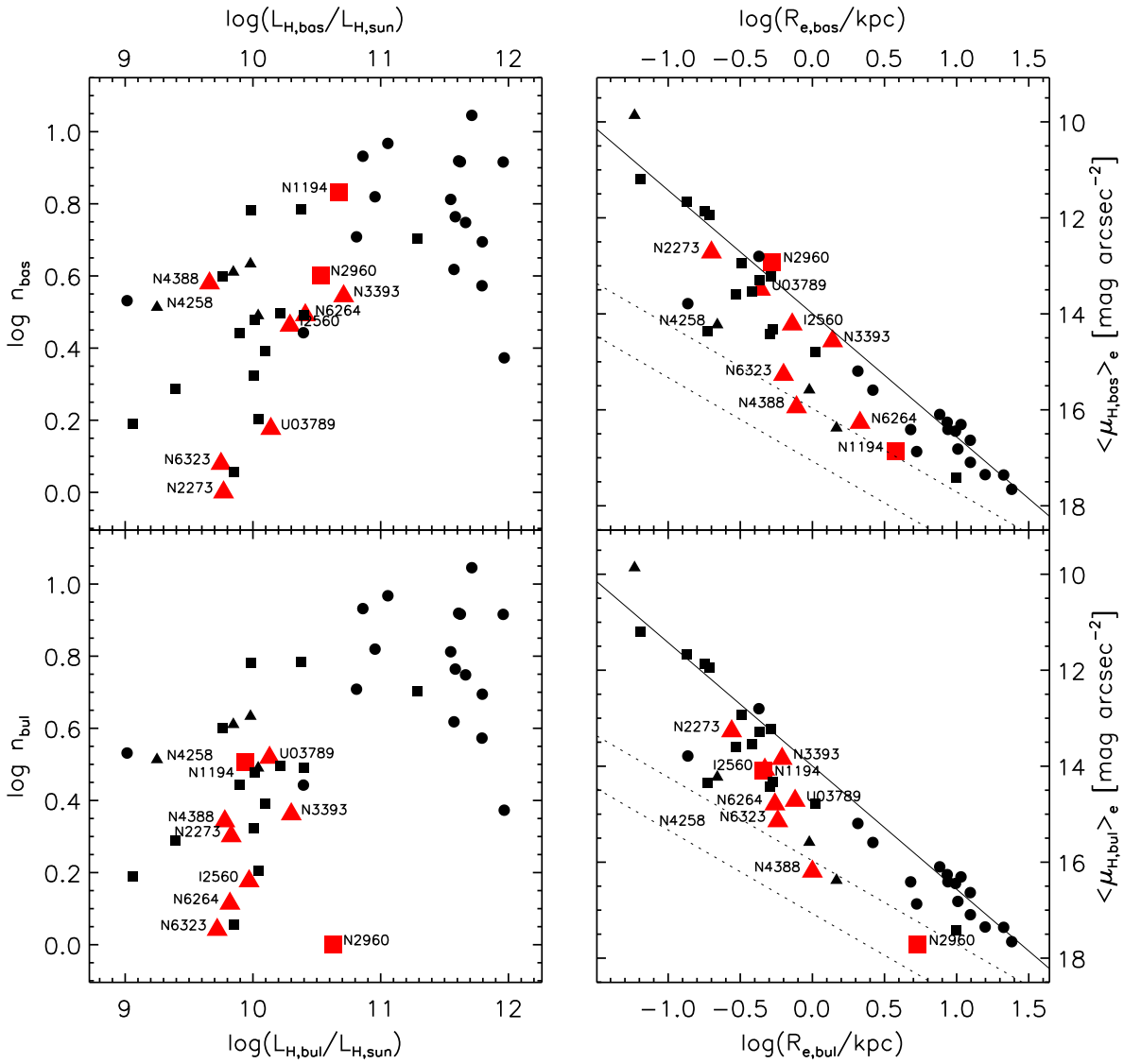

FIG. 5.— Correlations of photometric bulge parameters. The large red symbols represent the bulges of the present study, with "basic" bulges from bulge+disk decompositions shown in the top panels (subscript "bas") and classical bulges from full decompositions in the bottom panels (subscript "bul"). The bulges of L14 are overplotted as small black symbols, and the only megamaser-based $M_{\rm BH}$ from L14 (NGC 4258) labeled along with the rest of the maser hosts. Circles indicate elliptical, squares lenticular, and triangles spiral galaxies. *Left panels:* relation between bulge Sérsic index n and H-band bulge luminosity. Our measurements (bulges in mostly spiral galaxies) broadly match the L14 relation (mostly ellipticals and bulges in early-types), but the $n - L_H$ correlation is generally weak. *Right panels:* H-band surface brightness inside R_e (μ_e) versus R_e (Kormendy 1977). Overplotted in solid is the fit for early-type galaxies by Khosroshahi et al. (2000), transformed from K to H-band using an average $H - K = 0.3$ mag and distances corrected from their $H_0 = 50\,{\rm km\ s^{-1}Mpc^{-1}}$ to our $H_0 = 70\,{\rm km\ s^{-1}Mpc^{-1}}$. Dotted lines mark the upper limit for pseudobulge brightness recommended by Gadotti (2009), assuming $i - H = 2.1$ and $i - H = 3.2$ (the bluest and reddest bulge colors, respectively, in our sample): the classical bulge measurements for the megamaser hosts are only slightly below the early-type relation and avoid the region of pseudobulges, suggesting we indeed excluded the latter and recovered the classical bulge component. However, this applies to the basic bulge measurements as well, which have on average larger size and lower surface brightness than the classical bulges from full decompositions.

nuclear disk with a steep profile, neither of which is easily interpreted as a classical bulge. If we instead consider its basic bulge (bottom-left panel of Figure 5), it falls in line with the general trend.

4.3.3. *The $\mu_e - R_e$ relation*

We also investigate a projection of the Fundamental Plane (Dressler et al. 1987; Djorgovski & Davis 1987) to see whether we have isolated components that scale like elliptical galaxies. We use the Kormendy (1977) relation between the surface brightness measured within the effective radius ($\mu_{\rm e}$) and effective radius. We have asserted based on morphology that most of our galaxies harbor pseudobulges. Structural studies find that pseudobulges tend to have lower effective surface brightness at a given size than classical bulges and elliptical galaxies (Carollo 1999; MacArthur et al. 2003; Gadotti 2009; Laurikainen et al. 2010; Fisher & Drory 2010). Thus, we turn to this projection to test whether our galaxies have the structures of pseudobulges.

In Figure 5 (top right), we show the Kormendy relation for our basic bulges. They reside marginally below the relation for ellipticals and early-type bulges, but have relatively high effective surface brightness compared with

the pseudobulge selection advocated by Gadotti (2009). Interestingly, Laurikainen et al. (2010) also find that μ_e/R decreases in later-type spirals. Since our objects are nearly all S0-Sab galaxies, perhaps we should not be surprised that they do not fall far below the elliptical galaxy relation.

Nevertheless, we find clear evidence in the bulge morphologies for pseudobulge components. Why do these not translate into considerably lower μ_e at a given size as we might expect? We conclude that while nuclear bars, disks, and rings are readily apparent in our *HST* images, they do not carry a substantial fraction of the central mass. This is why we find only very small changes in mass and size when going from the "basic" to the "classical" bulge component. We can then investigate the nature of the dominant bulge components in these galaxies. From photometry alone, it is difficult to characterize these classical bulge components. In two cases, NGC2273 and NGC4388, we have additional kinematic information. Here we know that there is a nuclear disk on < 200pc scales, followed by $V/\sigma < 1$ further out in the bulge, showing that the stars outside of the nuclear disk are supported predominantly by random motions. In the case of these two galaxies, some of the stars are also part of the known kpc-scale bar (Veilleux et al. 1999; Falcón-Barroso et al. 2006; Greene et al. 2014). For the rest of our galaxies, we do not yet know the kinematics of the stars in our putative classical bulges.

4.4. *Final Bulge Classification*

For each galaxy, we will summarize the evidence that we have a pseudobulge, a classical bulge, or both. We established that in nearly all cases megamaser disk host galaxies show unambiguous pseudobulge signatures in the form of nuclear rings, nuclear or inner ($\lesssim 1$ kpc) disks, central dust, and spiral structures.The presence of these components is our criterion for classifying a galaxy as containing a pseudobulge.

We have also attempted to isolate classical bulges. As criteria for classical bulge determination we use (1) shape: they should be rounder than the large-scale disk; (2) surface brightness in relation to the effective radius: they should be close to the relation between μ_e and R_e defined by elliptical galaxies; and (3) Sérsic index: they should have high ($n > 2$) values. In our view, the Sérsic index is the least reliable discriminator of classical bulges, due to the large scatter in the $n-L$ plane. We determine that a galaxy contains a classical bulge if it satisfies two of these three criteria. For each galaxy, we assign a *P* to indicate a likely pseudobulge and a *C* to indicate a likely classical bulge.

IC2560: IC2560 is a relatively strongly inclined galaxy with a readily apparent X-shaped bar/bulge, which provides clear evidence for a pseudobulge component. We do identify a small classical bulge candidate that is rounder than the disk ($q = 0.6$ versus $q = 0.4$). The position in the $\mu_e - R_e$ diagram, close to the relation of early-type galaxies, likewise points towards a classical bulge, while the Sérsic index is somewhat low ($n = 1.5$). However, despite the above classical bulge indicators, given the dust and complexity of IC2560 in the central regions we cannot confirm that this small component is indeed a classical bulge. (P)

NGC1194: This edge-on, bulge-dominated galaxy is difficult to fit robustly due to significant dust contamination and a likely bar. The basic and classical bulge fits are round and both have a high Sérsic index. The effective surface brightness is not as high as in massive ellipticals, but is higher than expected for a pseudobulge based on the work of Gadotti (2009). Overall, we determine that NGC1194 contains a classical bulge. We do not find any pseudobulge component. (C)

NGC2273: While the $\mu_e - R_e$ position is consistent with expectations for classical bulges, the axis ratio of the putative classical bulge component matches that of the disk. The Sérsic index is intermediate with $n = 2$. Superposition of the candidate bulge component with the strong bar complicates significant detection of a classical bulge, and given the generally complex inner structure, we conclude that there is not sufficiently compelling evidence for a classical bulge component. NGC2273 unambiguously contains pseudobulge components. From photometry, it has long been known to contain multiple rings and a nuclear disk (Erwin et al. 2003). More recently, kinematic evidence has confirmed that the central ~ 200pc is dominated by a disk (Barbosa et al. 2006; Falcón-Barroso et al. 2006). There is also a kpc-scale bar component. (P)

NGC2960: Apart from a large-scale smooth and round component, this galaxy contains two central disks, one nuclear and one ~ 1 kpc-sized with inset spiral structure. It is particularly challenging in this case to determine what component comprises the bulge. Treating the nuclear disk component as the classical bulge yields a very low Sérsic index, but a high central surface brightness. The other option was suggested by KH13; the galaxy may be an elliptical that just swallowed a spiral galaxy. In that case the classical bulge may be the outer component and the inner (1 kpc) disk a recently acquired addition. The outer component is round, and the observed low μ_e is likely an artifact of the distortion to the center caused by the merger. Although technically this component does not satisfy our classical bulge requirements, we treat it as a classical bulge distorted by a merger. Since we detect an inner disk, it has a clear pseudobulge component. (CP)

UGC3789: This galaxy is relatively face on, so using the shape is challenging. However, given the high Sérsic index $n = 3.3$ and relatively high μ_e, we identify a classical bulge component. We see clear signs for pseudobulge components in the nuclear and larger-scale rings. (CP)

NGC3393: Like UGC3789, this galaxy is close to face on. The classical bulge candidate is round and has a Sérsic index $n = 2.3$. Because the galaxy is face on, we cannot infer much about the intrinsic shape of the component. The high effective surface brightness, combined with $n > 2$, argues for a classical bulge. NGC3393 contains multiple rings and a bar. The evidence for pseudobulge components is clear. (CP)

NGC4388: The classical bulge fit to this galaxy is rounder than the disk by a factor of two. However, given the low μ_e of the putative classical bulge, $n \approx 2$, and the significant dust extinction towards the galaxy center, we do not find a convincing classical bulge component. This well-known galaxy has a kpc-scale bar that has been studied kinematically (Veilleux et al. 1999). On the smallest scales, we have identified a nuclear disk both from the *HST* photometry and our NIR spectroscopy

(Greene et al. 2014), all pointing to a pseudobulge component. (P)

NGC6264: One of the most distant galaxies in the sample, this galaxy clearly contains a kpc-scale bar, and thus a pseudobulge component. The galaxy is close to face-on, so the axis ratio is not very constraining. The Sérsic index is low ($n \approx 1$) but μ_e relatively high. Given the lack of consensus between the different indicators and the distance of the galaxy leading to extra degeneracy with the bar, we do not robustly identify a classical bulge. (P)

NGC6323: We fit a very round central component as a classical bulge candidate. The low Sérsic index of $n \approx 1$ and the low surface brightness combined suggest that we have not isolated a classical bulge component. By contrast, the structural properties of the bulge and the inner kpc-scale disk/ring lead us to conclude that NGC6323 harbors a pseudobulge (P).

Armed with these bulge classifications, luminosities, and stellar masses for our different stellar components, we now turn to the primary goal of this paper, the BH scaling relations.

5. RESULTS: BH SCALING RELATIONS

Our goal is to learn about the origin of the BH-galaxy scaling relations by studying their slope, zeropoint, and scatter over as wide a dynamic range as possible. Before this work, there were very few dynamical BH masses in late-type galaxies. We add nine new systems with structural measurements.

5.1. *The Special Role of Megamaser Disk Galaxies*

In this subsection, we focus on the megamaser disk galaxies taken alone (including NGC4258 from L14). Megamasers play two important roles. First and foremost, VLBI allows us to resolve much smaller spheres of influence than optical or NIR stellar- or gas-dynamical methods, and the usually near-perfect Keplerian rotation curves traced by the masers provide the most precise and accurate extragalactic black hole mass measurements. Nuclear megamasers probe the full range of BH mass at a given galaxy property in a way that no other current technique can. Secondly, as a corollary, they allow us to probe BH mass in spiral galaxies, where gas, dust, and typically small spheres-of-influence all conspire to make stellar or gas-dynamical techniques especially challenging.

The megamaser disk galaxies span a stellar mass range of $\log M_*/M_\odot = 10.5 - 11.1$ (only a factor of four), and yet the BH masses span a range of $\log(M_{\rm BH}/M_\odot) \approx 6.4 - 7.8$, a factor of 25. If we take the scaling relations measured for predominantly early-type galaxies from L14, then for the measured BH masses we expect a range in bulge mass of 10^8 to $10^{10}\,M_\odot$, corresponding to a range in bulge-to-total light (B/T) of 10^{-3} (for IC2560) to 0.2 (NGC1194), with a median value of 0.03. In contrast, galaxies of these Hubble types (S0-Sb) typically have $B/T \approx 0.1 - 0.2$ (Simien & de Vaucouleurs 1986; Laurikainen et al. 2010). *It is already clear before we perform any fitting that these BHs would need to have very small classical bulge components if they were to obey the scaling relations seen in early-type galaxies.* A similar conclusion was reached for the $M_{\rm BH} - \sigma_*$ relation by Greene et al. (2010, see also KH13 for other refs).

The maser galaxies occupy a range of bulge masses $\log M_*/M_\odot = 9.5 - 11$. The wide distribution in BH mass in a narrow range of galaxy property[8] shows us that there is not a tight correlation between $M_{\rm BH}$ and galaxy or bulge mass for galaxies with $M_* \lesssim 10^{11}\,M_\odot$. Instead, the measured correlation found for early-type galaxies defines an upper envelope for the BH mass, with many of the megamaser galaxies scattering below this relation. As we will quantify in the following subsections, this broad tail towards low $M_{\rm BH}$ appears to hold even when we consider bulge rather than total galaxy mass.

This tail to low BH mass, which is most clearly apparent in the megamaser disk galaxies, raises a more basic question about the scaling relations. We have to wonder whether the scaling relations reflect the true distribution in nature, or whether they reflect our inability to measure BHs at low mass in high-mass galaxies (Batcheldor 2010). Gültekin et al. (2011) explore the possibility that the $M_{\rm BH} - \sigma$ relation is only an upper envelope, since galaxies with unresolved gravitational spheres of influence may be preferentially missing. At high galaxy mass, $\sigma_* > 250\,{\rm km\,s^{-1}}$ (corresponding roughly to $\sim 10^{11}\,M_\odot$; e.g., Häring & Rix 2004), Gültekin et al. (2011) show that the existing dynamical BH mass sample is large enough to rule out a long tail to low $M_{\rm BH}$[9]. However, at lower stellar velocity dispersion, a large range in $M_{\rm BH}$ at fixed galaxy property is what we observe. We discuss the possibility of bias in the low-mass galaxy sample, along with the possibility of bias in the megamaser disk galaxies, in §6.1. First we quantitatively fit the relationships between $M_{\rm BH}$ and measured galaxy properties.

5.2. *Fitting method*

We use the IDL implementation of the Bayesian inference-based LINMIX_ERR (Kelly 2007) for fitting our BH scaling relations between $M_{\rm BH}$ and galaxy properties. This routine naturally implements intrinsic scatter in the y-coordinate as part of the model, i.e. the relation is modeled as a probability distribution in (x, y) space. It renders a Markov-Chain Mote Carlo (MCMC) realization of the posterior distribution of the linear relation parameters, which are the zeropoint (α), slope (β), and dispersion of the Gaussian intrinsic scatter (ϵ). We thus fit relations of the form

$$y = \alpha + \beta(x - x_0) + \mathcal{G}(\epsilon)\ , \tag{4}$$

where $y = \log(M_{\rm BH}/M_\odot)$, x are logarithmic luminosities or masses, i.e. $x = \log(L_H/L_{\odot,H})$ or $x = \log(M/M_\odot)$, and $\mathcal{G}(\epsilon)$ symbolizes a Gaussian probability distribution with dispersion ϵ. The x-offset x_0 is calculated before fitting as the mean of the x-coordinates of the data in order to reduce covariance between α and β. The linear relation (4) implies a powerlaw between $M_{\rm BH}$ and L_H or M_*, and $\beta = 1$ corresponds to a linear relation between $M_{\rm BH}$ and the galaxy property. The presented result for each relation parameter is the mean and the 68% confidence interval of the posterior after marginalization over the other parameters. Some recent papers have suggested a

[8] Within this range, two galaxies in the L14 sample have $M_{\rm BH} > 10^8\,M_\odot$, increasing the total range of $M_{\rm BH}$ yet further (Figure 6).

[9] That is, barring dramatic problems with the BH masses, such as very steep IMF gradients (McConnell et al. 2013; Martín-Navarro et al. 2015)

broken power-law fit to BH scaling relations with bulge luminosity or mass (e.g., Graham & Scott 2015). This is an interesting possibility, but we do not have a sufficient sample size in this paper to address that possibility rigorously. The values quoted in Table 8 are the mean values of the parameters in the Markov Chain, and the given intervals delineate the 68% confidence interval of the drawn samples relative to the mean.

5.3. *Subsamples*

When we combine the megamaser disk galaxies with L14, we have a large enough sample to split galaxies based on various properties, and then ask where they fall in the BH-bulge mass plane. We will focus exclusively on the 44 galaxies (L14 and ours) that have dynamical BH mass measurements as described in §4.

We consider the following subsamples. We investigate the scaling of the 10 megamaser galaxies, which includes NGC4258 from the L14 sample. We also group all late-type galaxies. Many works (Hu 2008; Greene et al. 2008; Gadotti 2009; Greene et al. 2010; Kormendy et al. 2011) have suggested that late-type galaxies with pseudobulges may obey different scaling relations than classical bulges, since secular evolution may not efficiently fuel BH growth. In practice, because there is considerable overlap between the late-type and pseudobulge samples (7/9 of our megamaser sample), we will only consider one late-type subsample comprising the eight non-S0 megamasers considered here and the three additional spiral galaxies from L14. Finally, we consider a low-mass sample, since if the scaling relations arise from hierarchical merging via the central limit theorem (e.g. Peng 2007; Jahnke & Macciò 2011) then the scaling relations would break down at low mass. For this subsample we simply take the 22 lowest-mass or lowest-luminosity galaxies.

We calculate the offset of each subsample from the "primary relation", which is the relation fitted to the data excluding the respective subsample. For each Monte-Carlo realization of the primary relation, the offset Δa (Table 8) is the weighted-mean $y = \log M_{\rm BH}$-offset of the subsample from the primary relation. The weights are the y- and projected x-measurement errors, plus the intrinsic scatter in the relation, added in quadrature. We take into account the uncertainty in Δa by drawing it from its (Gaussian) error distribution around the weighted-mean offset. The intrinsic scatter of the subsample (ϵ) we subsequently determine by iteratively varying its value, and adding it in quadrature to the measurement errors, until $\chi^2 = 1$ for the given primary relation slope and subsample offset. We thus calculate Δa and ϵ for each element of the Markov chain, and the resulting Δa and ϵ distributions are evaluated for their mean and 1σ-uncertainty. The offset for the maser sample is referred to as $\Delta a_{\rm mega}$, that for the late-type galaxies is $\Delta a_{\rm late}$, and the low-mass sample is $\Delta a_{\rm low}$.

There is another sample of spiral galaxies with indirect BH masses, based on reverberation mapping. A subsample of the reverberation mapped AGN have *HST* imaging that allows detailed bulge-disk decompositions (Bentz et al. 2009a). These fall in an inferred $M_{\rm BH}$ range of $10^7 - 10^9\ M_\odot$ that overlaps with the megamaser disks at the low-mass end. Many of the hosts are also disk galaxies. Bentz et al. (2009b) find that $M_{\rm BH}$ is quite tightly correlated with $L_{\rm bul}$ (even with no conversion to mass) and do not see the long tail to low $M_{\rm BH}$ that is seen with the megamaser galaxies. Interestingly, the scatter seen between $M_{\rm BH}$ and σ_* is also smaller at $M_{\rm BH} \approx 10^7\ M_\odot$ for the reverberation-mapped sources than the megamaser disk galaxies (e.g., Greene et al. 2010; Woo et al. 2010). We discuss this difference in §6.1.

We also note that there are two other prominent outliers in the BH-bulge scaling relations (S0 galaxies NGC4342 and NGC3998) that have apparently high $M_{\rm BH}$ for their stellar mass. In both galaxies, the bulge luminosity is strongly dependent on the adopted decomposition (for details, see Läsker et al. 2014a). However, even taking the total luminosity as an upper limit on $L_{\rm bul}$ still puts their $M_{\rm BH}$ above the $M_{\rm BH} - L_{\rm bul}$ relation. In the case of NGC3998, $M_{\rm BH}$ would be five times lower if the gas-dynamical measurement was adopted instead of the stellar-dynamical model, true for many galaxies with both stellar and gas dynamical measurements (see Walsh et al. 2012). The BH mass measurement in NGC4342 is based on stellar dynamics. Here the large $M_{\rm BH}$ for its (bulge) luminosity is similar to an emerging class of S0 galaxies that appear to have overly massive BHs for their stellar bulge mass (van den Bosch et al. 2012; Walsh et al. 2015, 2016). These galaxies tend to be very compact with large central velocity dispersions and fast rotation on large scales, live in rich environments, and may have very different formation histories than the megamaser galaxies studied here. However, they contribute to our overall conclusion that there is very significant scatter in $M_{\rm BH}$ for bulge masses $< 5 \times 10^{10}\ M_\odot$.

5.4. *The $M_{\rm BH} - M_{\rm bas}$ relation for basic bulges*

We begin by examining the "basic" bulge fit, in which we assume that the galaxy can be well fit by the combination of a bulge, disk, and possible point source (Figure 6, left). These fits represent an upper limit on the bulge component, and are also a good analog to fits in the literature to the SDSS (e.g., Lackner & Gunn 2012) and to higher-redshift galaxies (Bell et al. 2012). The expected range of H-band bulge luminosities for the megamaser disks, based on the scaling relations, is 10^8 to $10^{10}\ L_\odot$. The observed range, in contrast, is much narrower (3×10^9 to $4 \times 10^{10}\ L_\odot$). If we measure the average offset in $M_{\rm BH}$ between the megamaser disks and the best-fit L14 relation ($\Delta a_{\rm mega}$ in Table 8, row 2), we find a mean offset of -0.8 ± 0.2 dex in BH mass from the best-fit relation.

These galaxies tend to have recent or ongoing star formation in their nuclei, biasing the observed bulge luminosities to high values compared with the predominantly old stellar populations that dominate early-type galaxies. We attempt to mitigate these differences by transforming to stellar mass. We try to put both the literature and megamaser galaxies on the same stellar mass scale to facilitate direct comparison (§3.6). When considering stellar mass rather than luminosity (Figure 6, right; $\Delta a_{\rm mega}$ in Table 8, row 5), we still see that the megamaser disks remain offset to smaller BH masses at a given bulge mass (-0.8 ± 0.2 dex).

If we instead examine the offset between the best-fit L14 relation, and the spiral galaxy subset rather than the megamaser subset, the net offset $M_{\rm BH}$ declines a bit, $\Delta a_{\rm late} = -0.6 \pm 0.2$ dex. The fact that the measured offset $\Delta a_{\rm late}$ is smaller than $\Delta a_{\rm mega}$ is interesting, and

TABLE 8
Scaling relation parameters $\log(M_{\rm BH}) - \log(x)$ with galaxy properties and galaxy subsamples

x	x_0	α		β		ϵ		$\Delta a_{\rm mega}$		$\epsilon_{\rm mega}$		$\Delta a_{\rm late}$		$\epsilon_{\rm late}$		$\Delta a_{\rm low}$		$\epsilon_{\rm low}$	
		val	err	val	err	val	err	val	err	val	err	val	err	val	err	val	err	val	err
$L_{\rm bul}$	10.56	8.13	0.09	0.87	0.11	0.56	0.07	-0.63	0.21	0.90	0.11	-0.51	0.24	0.73	0.12	0.09	0.39	0.72	0.14
$L_{\rm bas}$	10.64	8.12	0.09	0.99	0.13	0.57	0.07	-0.80	0.22	0.93	0.13	-0.58	0.24	0.76	0.13	0.04	0.37	0.76	0.13
$L_{\rm tot}$	10.93	8.12	0.11	0.99	0.19	0.71	0.09	-1.13	0.21	1.35	0.11	-1.03	0.22	1.23	0.12	0.47	0.40	1.04	0.25
$M_{\rm bul}$	10.66	8.12	0.08	0.88	0.10	0.52	0.06	-0.58	0.21	0.79	0.12	-0.49	0.22	0.70	0.12	-0.22	0.31	0.71	0.12
$M_{\rm bas}$	10.74	8.13	0.09	0.98	0.12	0.56	0.07	-0.76	0.22	0.89	0.13	-0.57	0.24	0.74	0.14	0.05	0.34	0.74	0.11
$M_{\rm tot}$	11.01	8.13	0.10	1.04	0.17	0.68	0.08	-1.05	0.20	1.25	0.11	-0.98	0.21	1.16	0.12	-0.04	0.36	0.84	0.12

Note. — The first column identifies the quantity x that is respectively fitted by a relation $\log(M_{\rm BH}/\,M_\odot) = \alpha + \beta(\log(x/x_\odot) - x_0) + G(\epsilon)$ (Equation 4 in Section 5.2), where $x_\odot$ is $L_{\odot,H}$ or $M_\odot$, and $G(\epsilon)$ denotes a Gaussian distribution with dispersion ϵ. Given in the second column is the offset x_0 (the inverse variance-weighted mean of all x), which is subtracted from the x before fitting in order to reduce covariance between α and β. All other parameters are fit to the data using LINMIX_ERR and the resulting Markov chain MonteCarlo (MCMC) sample, which is evaluated for the mean ("val") and the standard deviation ("err", i.e. the size of the 68%-confidence interval). These parameters are: the relation zeropoint (α), logarithmic slope (β), and log-scatter in the $y = \log(M_{\rm BH}/\,M_\odot)$-direction ($\epsilon$) for the fit to the entire sample of 44 objects, as well as the respective offset and intrinsic scatter of three subsamples: megamasers ("mega"), spiral galaxies ("late") and low-mass galaxies ("low"). Low-mass galaxies always constitute half of the sample, i.e. for each relation those 22 galaxies with the lowest x values. The subsamples' offsets are relative to a relation fit to the data minus the subsample; the parameters of these relations are not shown here. The subsample scatter ϵ is relative to the offset relation with the same β as the main relation.

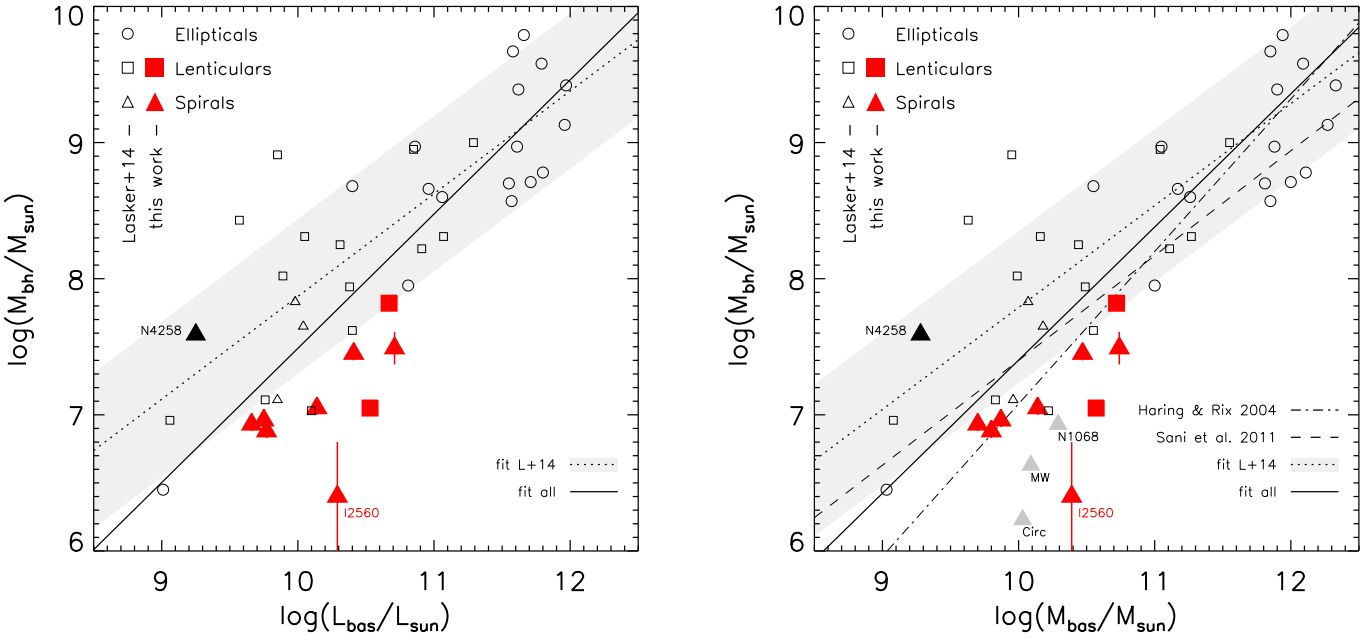

Fig. 6.— Correlation of $\log M_{\rm BH}$ with "basic" bulge based on simple bulge+disk(+point source) decompositions of our megamaser BH hosts. We show $\log L_{H,\rm bas}$ (left) and $\log M_{\rm bas}$ (right panel). The maser disks analyzed in this paper based on HST/WFC3 imaging are indicated by large filled red symbols with error bars. The errors on the bulge magnitudes are small, as we have not estimated systematic errors for these basic fits. The filled black symbol (NGC4258, which also has a megamaser-based $M_{\rm BH}$), and small open symbols (with error bars suppressed for clarity) are values from Läsker et al. (2014a), with their "spheroid" K-band luminosity converted to L_H and M as described in §3.5. Circles indicate elliptical, squares S0, and triangles spiral galaxies. The solid line represents the fit to the combined sample of L14 and the present study. The dotted line shows the relation fit when restricted to the L14 sample, i.e. with all megamasers except NGC4258 omitted, and the grey area indicates the 1σ intrinsic scatter (ϵ). For comparison, the $M_{\rm BH} - M_{\rm bul}$ relations of Sani et al. (2011) and Häring & Rix (2004) are overplotted as dashed and dot-dashed lines, respectively, in the right panel. For illustration, the grey labeled triangles in the right panel show three more BH hosts with $M_{\rm bul}$ taken from the literature. These, however, are excluded from our fit because the Milky Way (MW) bulge mass is highly uncertain while the megamaser-based $M_{\rm BH}$ (Circinus, NGC1068) are in question.

indicates a possible difference between the distribution of $M_{\rm BH}$ for megamaser disks and galaxies with stellar/gas dynamical BH mass measurements.

In summary, when we consider the most general concept of "bulge" as the centrally concentrated component that constitutes a light excess above the large-scale disk, we find a wide range of BH mass at fixed bulge mass and a significant offset from the early-type $M_{\rm BH} - M_{\rm bul}$ relation for the megamaser disks and late-type galaxies in general. A qualitatively similar result has been seen before in late-type galaxies for the subset of pseudobulge galaxies (Hu 2008; Greene et al. 2008; Sani et al. 2011; Kormendy & Ho 2013).

5.5. *The $M_{\rm BH} - M_{\rm bulge}$ relation for "classical" bulge components*

In §4 we described in detail our attempt to isolate a classical bulge component in the maser disk galaxies. Considering the colors, shapes, and structures of the putative "classical" bulge components, we identified a classical bulge in four cases (NGC1194, NGC2960,

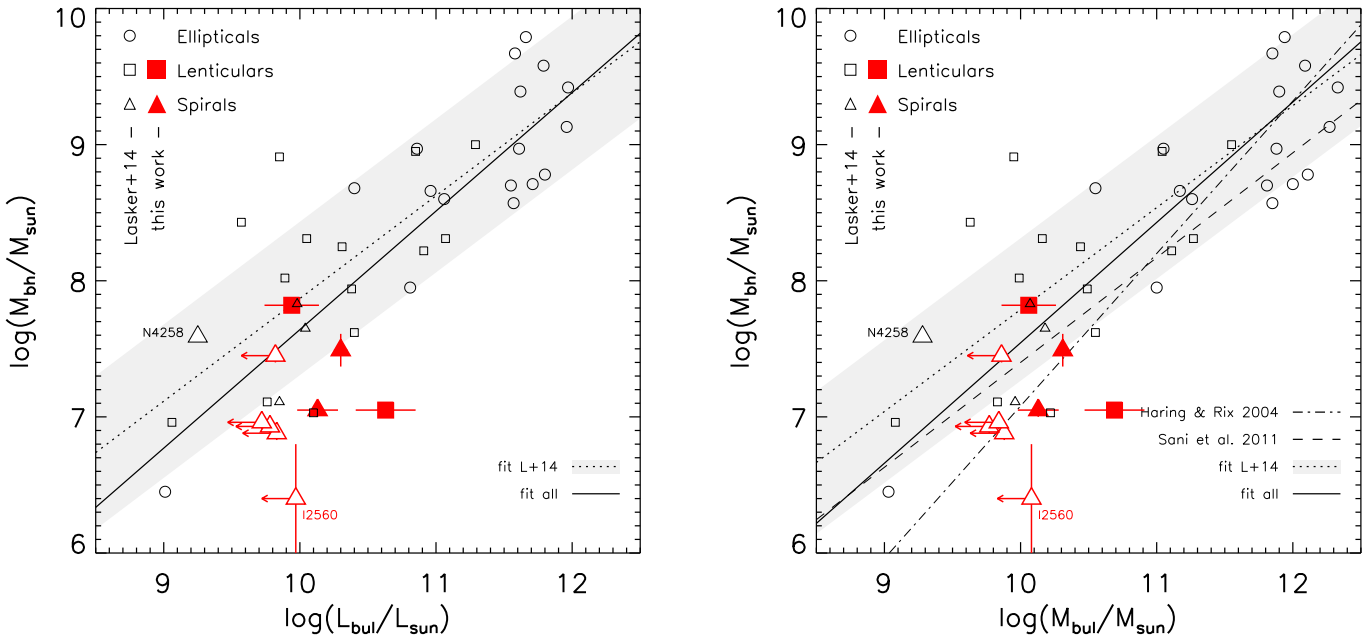

FIG. 7.— Same as Figure 6, but using the classical bulge parameters from our adopted multi-component decompositions for the megamaser hosts (filled red symbols with error bars). In cases where we do not identify a classical bulge, we plot an open symbol. The megamaser disk galaxy NGC4258 is indicated as an open triangle. The fits and the literature sample (Läsker et al. 2014a) are the same as in Figure 6. Using the more detailed decompositions moves the megamasers closer to the relation of the L+14 sample, but only slightly so. Similarly, the conversion to mass reduces the scatter marginally. The megamaser galaxies also appear to have lower $M_{\rm BH}$ at a given $L_{\rm bul}$ or $M_{\rm bul}$ than the general BH host population, while their scatter is similar to other galaxies in the low-mass regime they occupy.

NGC3393, and UGC3789).

We compare the BH and stellar mass for the confirmed classical bulges (solid symbols) in Figure 7. Obviously, these classical bulge components will, by construction, contain less stellar mass than the basic bulges (typically by ~ 0.2 dex), nominally improving the agreement with the elliptical galaxy $M_{\rm BH} - M_{\rm bul}$ relation. We indeed see better agreement overall when plotting $M_{\rm BH}$ against classical rather than basic bulge measurement: the offset in $M_{\rm BH}$ is $\Delta a_{\rm late} = -0.6 \pm 0.2$ dex. However, if we focus only on those galaxies where we believe there is a secure classical bulge component (filled symbols in Fig. 7), we see that there is still a net offset towards lower $M_{\rm BH}$ at a given bulge mass. Thus, we tentatively conclude that simply identifying more robust classical bulges in these galaxies will not eradicate the trend towards higher scatter and lower $M_{\rm BH}$ at a given bulge mass. As noted by Sani et al. (2011) and Läsker et al. (2014a), it is still difficult to definitively rule out that observational issues (e.g., hidden nuclear star clusters or other small-scale components) are contaminating our measurements, but as the number of galaxies with *HST* data and high-fidelity dynamical BH masses increase, it becomes more and more clear that there is simply a very wide range of $M_{\rm BH}$ in these low-mass galaxies.

5.6. $M_{\rm BH} - M_{\rm tot}$ *relation*

There has been considerable interest in recent years in the relation between total stellar mass and $M_{\rm BH}$, with various claims that total stellar mass also should show a relationship with $M_{\rm BH}$ (Peng 2007), possibly even tighter than bulge mass (Jahnke & Macciò 2011), and one that does not evolve with redshift (Cisternas et al. 2011; Jahnke et al. 2009; Bennert et al. 2010, 2011). We examine the $M_{\rm BH} - M_{\rm tot}$ relation using the L14 and our megamaser samples in Figure 8. Focusing on the stellar mass range where the megamasers are found, we see here the most striking mismatch between the range in $M_{\rm BH}$ (2.5 dex) and the range in stellar mass (0.4 dex). Thus, at a fixed stellar mass, galaxies may contain BHs with a wide range of mass. We do not see strong evidence that the total stellar mass to $M_{\rm BH}$ relation is tighter than others in the literature, and we see virtually no correlation at all below $M_* \approx 10^{11}\ M_\odot$. Regardless, $\epsilon(M_{\rm BH} - M_{\rm tot})$ is still marginally consistent with $\epsilon(M_{\rm BH} - M_{\rm bul})$ (cf. Läsker et al. 2014b). We measure an offset between the megamasers and the best-fit L14 relation of $\Delta a = -0.8 \pm 0.2$ dex, similar to the apparent offset between active and quiescent BHs observed by Reines & Volonteri (2015).

6. DISCUSSION AND SUMMARY

With the megamaser disk galaxies, we have a sample of $\sim L^*$ spiral galaxies with very precise BH mass measurements. The masers allow us to explore BH demographics in spiral galaxies more robustly than any other dynamical method. Firstly, we can spatially resolve the spheres of influence of much lower-mass BHs, allowing us to probe the full range of $M_{\rm BH}$ at fixed galaxy property. Secondly, the maser disks are not impacted by the dust and mixed stellar stellar populations that challenge stellar and gas dynamical techniques (although see also den Brok et al. 2015).

6.1. *The Role of Bias in Different BH Samples*

The megamaser disk galaxies span 1.5 dex in BH mass but only 0.6 dex in galaxy mass. Furthermore, the ratio of $M_{\rm BH}/M_*$ is, on average, considerably lower than what is seen in more massive elliptical and S0 galaxies. This long tail to low $M_{\rm BH}$ at fixed stellar mass is seen most conclusively in the maser disk samples, likely due

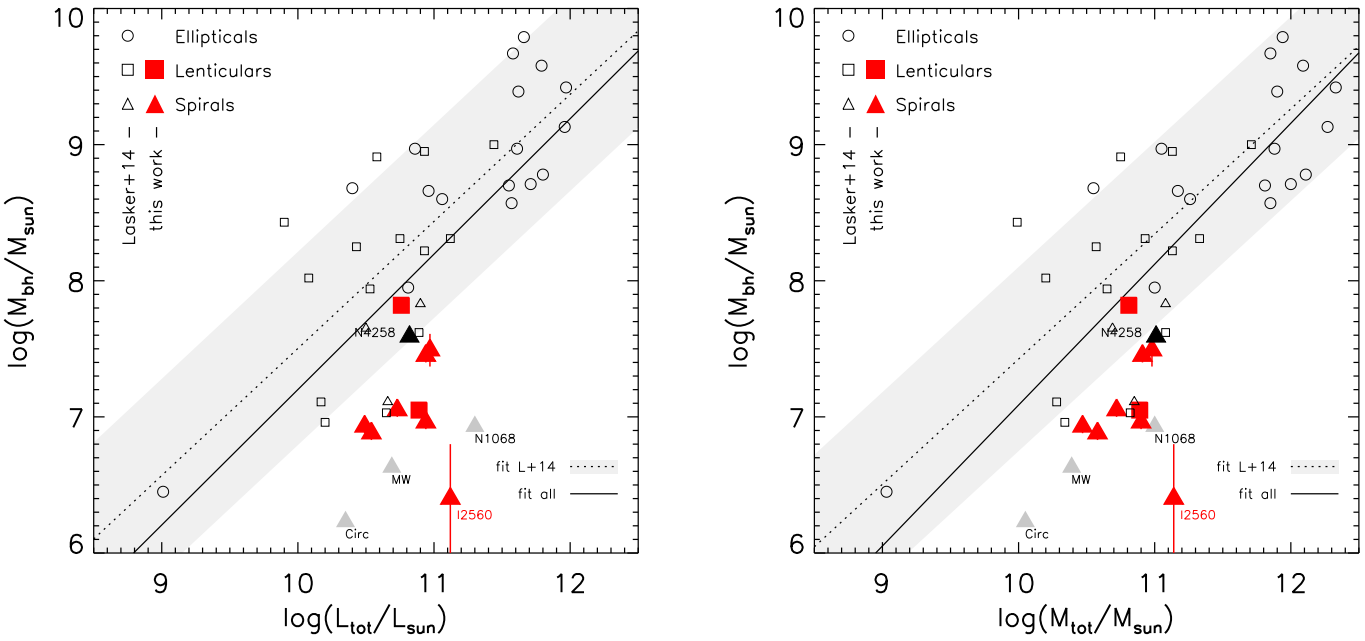

FIG. 8.— Correlation of log $M_{\rm BH}$ with total log $L_{H,\rm tot}$ (left panel) and log $M_{\rm tot}$ (right panel), for the megamaser BH hosts (large filled symbols, red for this study, NGC4258 in black) and for the L14 sample of BH hosts with $M_{\rm BH}$ from stellar or gas kinematics (small symbols). Symbols shapes (Hubble type) and lines (relation fits) are defined as in Figures 6 and 7. As for the relation with bulges, the megamaser hosts reside at lower $M_{\rm BH}$ than predicted by the fit (dotted line) to the predominantly early-type BH host galaxy sample (open symbols) of Läsker et al. (2014a).

to the difficulties of resolving the gravitational sphere of influence for low-mass BHs (Batcheldor 2010; Gültekin et al. 2011; van den Bosch et al. 2015). In the stellar mass range probed by the maser disks ($M_* < 10^{11}\,M_\odot$), we see a hint in this paper that stellar dynamical, gas dynamical, and reverberation-mapped samples do not truly sample the full range of $M_{\rm BH}$ at a given M_*. In particular, only the megamaser disk galaxies extend to the lowest $M_{\rm BH}$ probed at a fixed galaxy mass. In the case of the stellar and gas dynamical measurements, it is not surprising that the BHs do not sample the low-mass regime, since we cannot resolve their sphere of influence. Thus, we argue that only the megamaser disks reveal the true distribution of $M_{\rm BH}$ at a given galaxy property.

It is more difficult to pin down the origin of the difference between the maser and the reverberation mapped sources. One possibility is a bias in the reverberation-based BH masses, which after all have been calibrated to follow the inactive $M_{\rm BH} - \sigma$ relation. Alternatively, the reverberation sources may also have a bias toward higher $M_{\rm BH}$ at a given galaxy mass, due to the preferential selection of the most luminous sources with correspondingly high mass BHs. Until we come to a full understanding of this issue, it will be difficult to fully compare the scaling relations for single-epoch virial BH masses with dynamical BH masses (e.g., Graham & Scott 2015; Reines & Volonteri 2015).

Alternatively, the megamaser disk sample could have a bias towards lower $M_{\rm BH}$ at fixed galaxy property due to their selection as active galaxies if, for some reason, the megamaser disks pick out galaxies that are preferentially growing towards the end state of the $M_{\rm BH} - \sigma$ relation. The megamaser disks are nearly the only active galaxies with dynamical BH masses, so it is worth considering the possibility that masers select a non-representative sample. We argue against that possibility, repeating the arguments in Greene et al. (2010). The galaxies are found, on average, a factor of four below the relation between $M_{\rm BH}$ and $L_{\rm bulge}$. To erase this offset, at their current Eddington ratios of $\sim 10\%$ (Greene et al. 2010), would require $\sim$ 1 Gyr of steady BH growth. On the other hand, typical lifetimes of AGN are likely shorter than this (Martini & Weinberg 2001) while pseudobulge growth times are much longer than this (Kormendy & Kennicutt 2004), so how the megamaser disks would know to grow at this particular moment is difficult to understand. Furthermore, if such a bias impacted the maser galaxies, we would expect to see the same effect in the reverberation-mapped sources, which we do not.

In principle, it is also possible that megamaser disk galaxies are biased against the most massive BHs (Reines & Volonteri 2015; van den Bosch et al. 2016). However, if there were a large sample of spiral galaxies with very massive BHs ($\gtrsim 10^8\,M_\odot$) we would likely know about them already from stellar- or gas-dynamical $M_{\rm BH}$ measurements.

6.2. *Differences in Scaling Relations*

Barring such biases, megamaser disks enable us to probe the underlying distribution of BH mass for spiral galaxies. The observations presented here apply (at minimum) to all BHs in spiral galaxies with $M_* < 10^{11}\,M_\odot$. That is, at a fixed galaxy property, there is a large range of $M_{\rm BH}$, extending systematically below the relations defined by the early-type, massive galaxies.

We consider two explanations for the differences in scaling relations between the masers and early-type galaxies. One is that the scaling relations vary with galaxy morphology. In this picture, the formation history of the galaxy (e.g., the formation of a massive bulge) is tied to the fueling and feedback processes of the growing BH. For instance, galaxies that build their central

bulges primarily with secular processes may never efficiently fuel their BHs (e.g., Hu 2008; Greene et al. 2008; Gadotti 2008). This would result in the observed offset to lower masses, along with significant scatter, preferentially among spirals. To test these possibilities, we urgently need BH mass measurements in more bulge-dominated low-mass galaxies like M32. We also note the intruiging possibility raised by Saglia et al. (2016) that at high enough mass density, the BHs in pseudobulges obey the same scaling relations

The other possibility is that the BH scaling relations are driven by merging via the central limit theorem, as advocated by Peng (2007) and Jahnke & Macciò (2011). In this picture, galaxies with fewer mergers do not converge to a tight scaling relation, leading to a strong dependence of scatter on galaxy (or halo) mass. If we could measure the scatter in the scaling relations as a function of mass and morphology over the full range of $M_{\rm BH}$, we could determine which of these scenarios is preferred. Unfortunately, we still have very few measurements at low mass, and vanishingly few in low-mass early-type galaxies (M32, van den Bosch & de Zeeuw 2010; NGC404, Seth et al. 2010, Nguyen et al. in prep.; NGC 4395 den Brok et al. 2015). It remains very challenging to distinguish these two possibilities.

Finally, there is the possibility that the scaling relations are completely artificial and actually just define an upper envelope that arises due to problems with the stellar and gas-dynamical methods. Others have considered this possibility (Batcheldor 2010; Gültekin et al. 2011; van den Bosch et al. 2015). In the coming decade, ALMA (Davis 2014) and 30m-class telescopes (Do et al. 2014) will provide an order of magnitude increase in angular resolution, allowing us to test this possibility. What we really need are megamaser disks in early-type galaxies. Searches thus far have not been successful (van den Bosch et al. 2016), but they are worth continuing.

Despite significantly increasing the sample of L^* spiral galaxies with dynamical $M_{\rm BH}$ measurements, our samples at low mass and late-type morphology remain small. Thus, our conclusions are not yet definitive. While we did our best to identify classical bulges with photometric indicators, a combination of photometry and kinematics would undoubtedly work better (e.g., Erwin et al. 2015). Luckily, there are additional megamaser disk galaxies with Keplerian rotation curves and secure $M_{\rm BH}$ being observed with *HST* in Cycle 22 (P.I. Greene). We are also securing AO-assisted integral-field observations of the stellar and gas kinematics in five of these objects with SINFONI on the VLT (P.I. Greene). The combination of these two data sets should prove powerful in setting our results on firmer ground.

ACKNOWLEDGMENTS

We thank Stefano Zibetti for providing his $(g-i, i-H)$ mass-to-light ratio tables. RL thanks Arjen van der Wel for advice on reconstructing the WFC3 PSF, as well as Remco van den Bosch and Akin Yildirim for useful discussions. We are also grateful to Chien Y. Peng for his substantial advice on our analysis, and to Dimitri Gadotti, Alister Graham, Kayhan Gültekin, John Kormendy, Amy Reines and Marta Volonteri for their comments on the manuscript. JEG was partially supported by NSF grant AAG:1310405. Based on observations obtained with the Apache Point Observatory 3.5-meter telescope, which is owned and operated by the Astrophysical Research Consortium; on observations at Kitt Peak National Observatory, National Optical Astronomy Observatory (NOAO Prop. ID: 2011A-0170; PI: J. Greene), which is operated by the Association of Universities for Research in Astronomy (AURA) under a cooperative agreement with the National Science Foundation; and the Las Campanas Observatory 100-inch du Punt telescope, operated by the Carnegie Insitution for Science (CIS). Funding for the NASA-Sloan Atlas has been provided by the NASA Astrophysics Data Analysis Program (08-ADP08-0072) and the NSF (AST-1211644). This research has made use of the NASA/IPAC Extragalactic Database (NED) which is operated by the Jet Propulsion Laboratory, California Institute of Technology, under contract with the National Aeronautics and Space Administration.

REFERENCES

Andredakis, Y. C., & Sanders, R. H. 1994, MNRAS, 267, 283
Barbosa, F. K. B., Storchi-Bergmann, T., Cid Fernandes, R., Winge, C., & Schmitt, H. 2006, MNRAS, 371, 170
Batcheldor, D. 2010, ApJ, 711, L108
Beifiori, A., Courteau, S., Corsini, E. M., & Zhu, Y. 2012, MNRAS, 419, 2497
Bell, E. F., McIntosh, D. H., Katz, N., & Weinberg, M. D. 2003, ApJS, 149, 289
Bell, E. F., van der Wel, A., Papovich, C., et al. 2012, ApJ, 753, 167
Bennert, V. N., Auger, M. W., Treu, T., Woo, J.-H., & Malkan, M. A. 2011, ApJ, 742, 107
Bennert, V. N., Treu, T., Woo, J.-H., et al. 2010, ApJ, 708, 1507
Bentz, M. C., Peterson, B. M., Netzer, H., Pogge, R. W., & Vestergaard, M. 2009a, ApJ, 697, 160
Bentz, M. C., Peterson, B. M., Pogge, R. W., & Vestergaard, M. 2009b, ApJ, 694, L166
Blanton, M. R., Kazin, E., Muna, D., Weaver, B. A., & Price-Whelan, A. 2011, AJ, 142, 31
Braatz, J. A., Reid, M. J., Humphreys, E. M. L., et al. 2010, ApJ, 718, 657
Cappellari, M. 2013, ApJ, 778, L2
Carollo, C. M. 1999, ApJ, 523, 566
Carollo, C. M., Stiavelli, M., de Zeeuw, P. T., & Mack, J. 1997, AJ, 114, 2366
Cisternas, M., Jahnke, K., Bongiorno, A., et al. 2011, ApJ, 741, L11
Conroy, C., Gunn, J. E., & White, M. 2009, ApJ, 699, 486
Davis, T. A. 2014, MNRAS, 443, 911
de Vaucouleurs, G., de Vaucouleurs, A., Corwin, Jr., H. G., et al. 1991, Third Reference Catalogue of Bright Galaxies. Volume I: Explanations and references. Volume II: Data for galaxies between 0^h and 12^h. Volume III: Data for galaxies between 12^h and 24^h.
Debuhr, J., Quataert, E., Ma, C.-P., & Hopkins, P. 2010, MNRAS, 406, L55
den Brok, M., Seth, A. C., Barth, A. J., et al. 2015, ArXiv e-prints, arXiv:1507.04358
Djorgovski, S., & Davis, M. 1987, ApJ, 313, 59
Do, T., Wright, S. A., Barth, A. J., et al. 2014, AJ, 147, 93
Dressler, A., Lynden-Bell, D., Burstein, D., et al. 1987, ApJ, 313, 42
Erwin, P., Beckman, J. E., & Pohlen, M. 2005, ApJ, 626, L81
Erwin, P., Beltrán, J. C. V., Graham, A. W., & Beckman, J. E. 2003, ApJ, 597, 929
Erwin, P., Pohlen, M., & Beckman, J. E. 2008, AJ, 135, 20
Erwin, P., & Sparke, L. S. 2003, ApJS, 146, 299

Erwin, P., Saglia, R. P., Fabricius, M., et al. 2015, MNRAS, 446, 4039
Fabian, A. C. 2012, ARA&A, 50, 455
Falcón-Barroso, J., Bacon, R., Bureau, M., et al. 2006, MNRAS, 369, 529
Ferrarese, L., & Ford, H. 2005, Space Sci. Rev., 116, 523
Fisher, D. B., & Drory, N. 2010, ApJ, 716, 942
Fukugita, M., Ichikawa, T., Gunn, J. E., et al. 1996, AJ, 111, 1748
Gadotti, D. A. 2008, MNRAS, 384, 420
—. 2009, MNRAS, 393, 1531
Gao, F., Braatz, J. A., Reid, M. J., et al. 2015, ArXiv e-prints, arXiv:1511.08311
Ghez, A. M., Salim, S., Weinberg, N. N., et al. 2008, ApJ, 689, 1044
Gillessen, S., Eisenhauer, F., Trippe, S., et al. 2009, ApJ, 692, 1075
Graham, A. W., & Driver, S. P. 2007, ApJ, 655, 77
Graham, A. W., & Scott, N. 2015, ApJ, 798, 54
Greene, J. E., Ho, L. C., & Barth, A. J. 2008, ApJ, 688, 159
Greene, J. E., Seth, A., Lyubenova, M., et al. 2014, ApJ, 788, 145
Greene, J. E., Peng, C. Y., Kim, M., et al. 2010, ApJ, 721, 26
Greene, J. E., Seth, A., den Brok, M., et al. 2013, ApJ, 771, 121
Greenhill, L. J., Gwinn, C. R., Antonucci, R., & Barvainis, R. 1996, ApJ, 472, L21
Greenhill, L. J., Booth, R. S., Ellingsen, S. P., et al. 2003, ApJ, 590, 162
Gu, Q.-S., Shi, L., Lei, S.-J., Liu, W.-H., & Huang, J.-H. 2003, Chinese J. Astron. Astrophys., 3, 203
Gültekin, K., Tremaine, S., Loeb, A., & Richstone, D. O. 2011, ApJ, 738, 17
Häring, N., & Rix, H.-W. 2004, ApJ, 604, L89
Herrnstein, J. R., Moran, J. M., Greenhill, L. J., & Trotter, A. S. 2005, ApJ, 629, 719
Herrnstein, J. R., Moran, J. M., Greenhill, L. J., et al. 1999, Nature, 400, 539
Hu, J. 2008, MNRAS, 386, 2242
Humphreys, E. M. L., Reid, M. J., Moran, J. M., Greenhill, L. J., & Argon, A. L. 2013, ApJ, 775, 13
Jahnke, K., & Macciò, A. V. 2011, ApJ, 734, 92
Jahnke, K., Bongiorno, A., Brusa, M., et al. 2009, ApJ, 706, L215
Kelly, B. C. 2007, ApJ, 665, 1489
Khosroshahi, H. G., Wadadekar, Y., Kembhavi, A., & Mobasher, B. 2000, ApJ, 531, L103
Kondratko, P. T., Greenhill, L. J., & Moran, J. M. 2008, ApJ, 678, 87
Kormendy, J. 1977, ApJ, 218, 333
Kormendy, J., Bender, R., & Cornell, M. E. 2011, Nature, 469, 374
Kormendy, J., & Ho, L. C. 2013, ARA&A, 51, 511
Kormendy, J., & Kennicutt, Jr., R. C. 2004, ARA&A, 42, 603
Kriek, M., Labbé, I., Conroy, C., et al. 2010, ApJ, 722, L64
Krist, J., Hook, R., & Stoehr, F. 2010, Tiny Tim: Simulated Hubble Space Telescope PSFs, Astrophysics Source Code Library, ascl:1010.057
Kuo, C. Y., Braatz, J. A., Reid, M. J., et al. 2013, ApJ, 767, 155
Kuo, C. Y., Braatz, J. A., Condon, J. J., et al. 2011, ApJ, 727, 20
Kuo, C. Y., Braatz, J. A., Lo, K. Y., et al. 2015, ApJ, 800, 26
Lackner, C. N., & Gunn, J. E. 2012, MNRAS, 421, 2277
Läsker, R., Ferrarese, L., & van de Ven, G. 2014a, ApJ, 780, 69
Läsker, R., Ferrarese, L., van de Ven, G., & Shankar, F. 2014b, ApJ, 780, 70
Laurikainen, E., Salo, H., Buta, R., Knapen, J. H., & Comerón, S. 2010, MNRAS, 405, 1089
Lo, K. Y. 2005, ARA&A, 43, 625
Lodato, G., & Bertin, G. 2003, A&A, 398, 517
MacArthur, L. A., Courteau, S., & Holtzman, J. A. 2003, ApJ, 582, 689
Maraston, C. 2005, MNRAS, 362, 799
Marconi, A., & Hunt, L. K. 2003, ApJ, 589, L21
Marigo, P., Girardi, L., Bressan, A., et al. 2008, A&A, 482, 883
Martín-Navarro, I., Barbera, F. L., Vazdekis, A., Falcón-Barroso, J., & Ferreras, I. 2015, MNRAS, 447, 1033
Martini, P., & Weinberg, D. H. 2001, ApJ, 547, 12
McConnell, N. J., Chen, S.-F. S., Ma, C.-P., et al. 2013, ApJ, 768, L21
McConnell, N. J., & Ma, C.-P. 2013, ApJ, 764, 184
Menéndez-Delmestre, K., Sheth, K., Schinnerer, E., Jarrett, T. H., & Scoville, N. Z. 2007, ApJ, 657, 790
Miyoshi, M., Moran, J., Herrnstein, J., et al. 1995, Nature, 373, 127
Mulchaey, J. S., Regan, M. W., & Kundu, A. 1997, ApJS, 110, 299
Nowak, N., Thomas, J., Erwin, P., et al. 2010, MNRAS, 403, 646
Oke, J. B., & Gunn, J. E. 1983, ApJ, 266, 713
Peng, C. Y. 2007, ApJ, 671, 1098
Peng, C. Y., Ho, L. C., Impey, C. D., & Rix, H.-W. 2010, AJ, 139, 2097
Petitpas, G. R., & Wilson, C. D. 2002, ApJ, 575, 814
Pohlen, M., & Trujillo, I. 2006, A&A, 454, 759
Ravindranath, S., Ho, L. C., Peng, C. Y., Filippenko, A. V., & Sargent, W. L. W. 2001, AJ, 122, 653
Reid, M. J., Braatz, J. A., Condon, J. J., et al. 2009, ApJ, 695, 287
—. 2013, ApJ, 767, 154
Reines, A. E., & Volonteri, M. 2015, ApJ, 813, 82
Roediger, J. C., & Courteau, S. 2015, ArXiv e-prints, arXiv:1507.03016
Saglia, R. P., Opitsch, M., Erwin, P., et al. 2016, ArXiv e-prints, arXiv:1601.00974
Sani, E., Marconi, A., Hunt, L. K., & Risaliti, G. 2011, MNRAS, 413, 1479
Schlafly, E. F., & Finkbeiner, D. P. 2011, ApJ, 737, 103
Sérsic, J. L. 1963, Boletin de la Asociacion Argentina de Astronomia La Plata Argentina, 6, 41
Seth, A. C., Cappellari, M., Neumayer, N., et al. 2010, ApJ, 714, 713
Seth, A. C., van den Bosch, R., Mieske, S., et al. 2014, Nature, 513, 398
Silk, J., & Rees, M. J. 1998, A&A, 331, L1
Simien, F., & de Vaucouleurs, G. 1986, ApJ, 302, 564
Smee, S. A., Barkhouser, R. H., Scharfstein, G. A., et al. 2011, PASP, 123, 87
Springel, V., Di Matteo, T., & Hernquist, L. 2005, MNRAS, 361, 776
Sun, A.-L., Greene, J. E., Impellizzeri, C. M. V., et al. 2013, ApJ, 778, 47
van den Bosch, R. C. E., & de Zeeuw, P. T. 2010, MNRAS, 401, 1770
van den Bosch, R. C. E., Gebhardt, K., Gültekin, K., et al. 2012, Nature, 491, 729
van den Bosch, R. C. E., Gebhardt, K., Gültekin, K., Yıldırım, A., & Walsh, J. L. 2015, ApJS, 218, 10
van den Bosch, R. C. E., Greene, J. E., Braatz, J. A., Constantin, A., & Kuo, C.-Y. 2016, ArXiv e-prints, arXiv:1601.00645
Veilleux, S., Bland-Hawthorn, J., & Cecil, G. 1999, AJ, 118, 2108
Vika, M., Driver, S. P., Cameron, E., Kelvin, L., & Robotham, A. 2012, MNRAS, 419, 2264
Walsh, J. L., van den Bosch, R. C. E., Barth, A. J., & Sarzi, M. 2012, ApJ, 753, 79
Walsh, J. L., van den Bosch, R. C. E., Gebhardt, K., et al. 2015, ApJ, 808, 183
—. 2016, ApJ, 817, 2
Weinzirl, T., Jogee, S., Khochfar, S., Burkert, A., & Kormendy, J. 2009, ApJ, 696, 411
Woo, J.-H., Treu, T., Barth, A. J., et al. 2010, ApJ, 716, 269
Yamauchi, A., Nakai, N., Ishihara, Y., Diamond, P., & Sato, N. 2012, PASJ, 64, arXiv:1207.6820
York, D. G., Adelman, J., Anderson, Jr., J. E., et al. 2000, AJ, 120, 1579
Zibetti, S., Charlot, S., & Rix, H.-W. 2009, MNRAS, 400, 1181
Zibetti, S., Gallazzi, A., Charlot, S., Pierini, D., & Pasquali, A. 2013, MNRAS, 428, 1479

APPENDIX

DETAILED NOTES ON GALAXY DECOMPOSITIONS

IC 2560

IC2560 (Figures 9 and 10) contains a large-scale disk with well-defined spiral arms at intermediate radii. The disk is detectable out to $\sim 150''$ (30 kpc) along the major axis (with PA$= -50$ deg) and has an axis ratio of ~ 0.6; it grows rounder at large radius. The tightly-wound spiral arms range from 6-12 kpc ($30 - 60$") and broadly resemble a ring. The central X-shaped bulge/bar dominates the light inside $\sim 10''$ (2 kpc). Finally, the surface-brightness profile exhibits a "knee" at $1''$ (0.2 kpc) that corresponds to a nuclear disk.

The spiral ring and X-shaped bulge/bar are apparent in the residuals to the basic bulge+disk model (Figure 10). Thus, in our more complex fit, we introduce one component for the ring and one for the X-shaped bar/bulge. We also include a large-scale (extended) envelope, with a best-fit exponential scale radius of $47''$ (9.5 kpc) to accommodate the obviously rounder outer component. Our best-fit model (Figure 9) also includes a faint nuclear disk that is exposed in the residual image and indicated by profile inflections around $1''$. Although the formal χ^2 improves only marginally when the disk is added, we see spiral structure associated with the nuclear disk in the residual image, and the disk model perfectly fits the apparent knee in the μ-profile at SMA $\sim 1''$ (0.2 kpc). The bulge component changes when the nuclear disk is included, growing by $1''$ (a factor of two) and 0.34 mag, as it is no longer trying to fit the very compact nuclear disk.

In the best-fit model, we fix the Sérsic index of the ring, envelope and nuclear disk to 1, 1, and 0.5 respectively. The ring is modified by an inner truncation. The X-shape is modeled by a 4th-order Fourier mode. Our estimate for the systematic (modeling) error of the classical bulge magnitude is 0.4 mag, which we derive by considering the difference between the best-fit values from our reference model and several alternative models: allowing a free Sérsic index for first the envelope (bulge magnitude unchanged, $n_{\rm env} \rightarrow 0.6$), then the nuclear disk ($+0.3$ mag, $n_{\rm nuc.disk} \rightarrow 0.8$), and finally the main disk (-0.4 mag, $n_{\rm d} \rightarrow 0.2$). We also construct alternative models by omitting from the model the nuclear disk (bulge $+0.3$ mag), or omit the X-shaped pseudobulge (-0.6 mag).

Our high resolution data allows us to cleanly separate the X-shaped bar/bulge from from a nuclear disk and the small, round (possibly classical) bulge. In the low-resolution and shallower *Spitzer* data of Sani et al. (2011), they are clearly fitting the disk and envelope together, since their disk is rounder than their bulge component. Likewise, their bulge component contains multiple components. In net, they find a B/T of about 0.5, i.e. significantly higher than even the B/T of 0.18 in our basic model.

NGC 1194

NGC1194 (Figures 11 and 12) appears to be an S0 seen at relatively high inclination. The innermost region ($\sim 1''$ nucleus) is round, bright, and distinct from the flatter ($q \sim 0.5$) outer regions, which can be visually traced to about $90''$ (20 kpc). The ellipticity profile features a local peak at $\sim 3''$ (~ 0.7 kpc), followed by a trough at $\sim 8''$ (2 kpc). Subtracting the basic bulge+disk model additionally reveals a dust lane that is parallel to the major axis but offset by $\sim 4''$ to the south-west, as well as a minor-axis boxy light excess at $\sim 6''/1.5$ kpc.

Turning to the basic model first, we see that there is no need for an AGN component as the central light is already slightly overestimated by the bulge+disk model. Out to $\sim 1''$ a major-axis excess in residual light may indicate an edge-on nuclear disk, while on larger scales ("$\sim 6''$; Figure 12) we may be seeing the residuals of an end-on bar. There is a local ellipticity peak $\sim 40''$ likely pointing to a disk component. At large radius, the basic model fits the extended light profile with the bulge (leading to a very high Sérsic index $n = 6.8$), but the best-fit bulge is too round to fit the outer component properly and leads to a over-extended profile at large radii compared with the profile in the data.

Our adopted model includes a bar-like component and an "envelope", in addition to a bulge, disk, and point source. The envelope, which has a best-fit Sérsic profile with $n = 2$, reduces the flux excess and axis ratio at the largest scales ($\gtrsim 100''$) compared to the basic bulge+disk model, as well as reducing the bulge Sérsic index ($n = 3.2$). The envelope is intermediate in flattening between bulge and disk: $q = 0.5$, versus 0.7 and 0.4, respectively. This outer component is as flattened as the inner disk, and carries a large share of the total flux ($\sim 75\%$), so we surmise that it probably represents a large-scale thick disk. Supporting this interpretation, there is also a large HI-disk in NGC1194 (Sun et al. 2013). The bar-like component fits the apparent minor axis excess on $\sim 10''$ scales. An additional $0.3''$(80 pc)-sized nuclear component can be fit and slightly improves residuals, but we refrain from including it in our adopted model due to the complicated and dust obscured center. However, we retain such a model with nuclear component as an alternative that serves to estimate the systematic modeling errors of the model parameters.

Turning to the systematic errors, we find that the basic bulge is 1.8 mag brighter than the bulge component in our adopted model. If we remove just the envelope from the adopted model, we obtain a 1.6 mag brighter bulge. Interestingly, if we *add* to the adopted model the putative nuclear component, while constraining the envelope Sérsic index to $n = 1$ to reduce degeneracy, we again get a significantly *brighter* bulge than in our adopted model (by 0.8 mag). Conversely, the bulge parameters barely change when we fit the large-scale disk with a Sérsic profile (0.1 mag fainter bulge, and $n_{\rm disk} \rightarrow 0.8$). Finally, we explored whether masking of dust features (central, and particularly the lane parallel to the major axis) alters our results and found virtually no difference in parameters when applying the mask. In summary, these alternative models indicate a systematic bulge magnitude uncertainty of 0.8 mag.

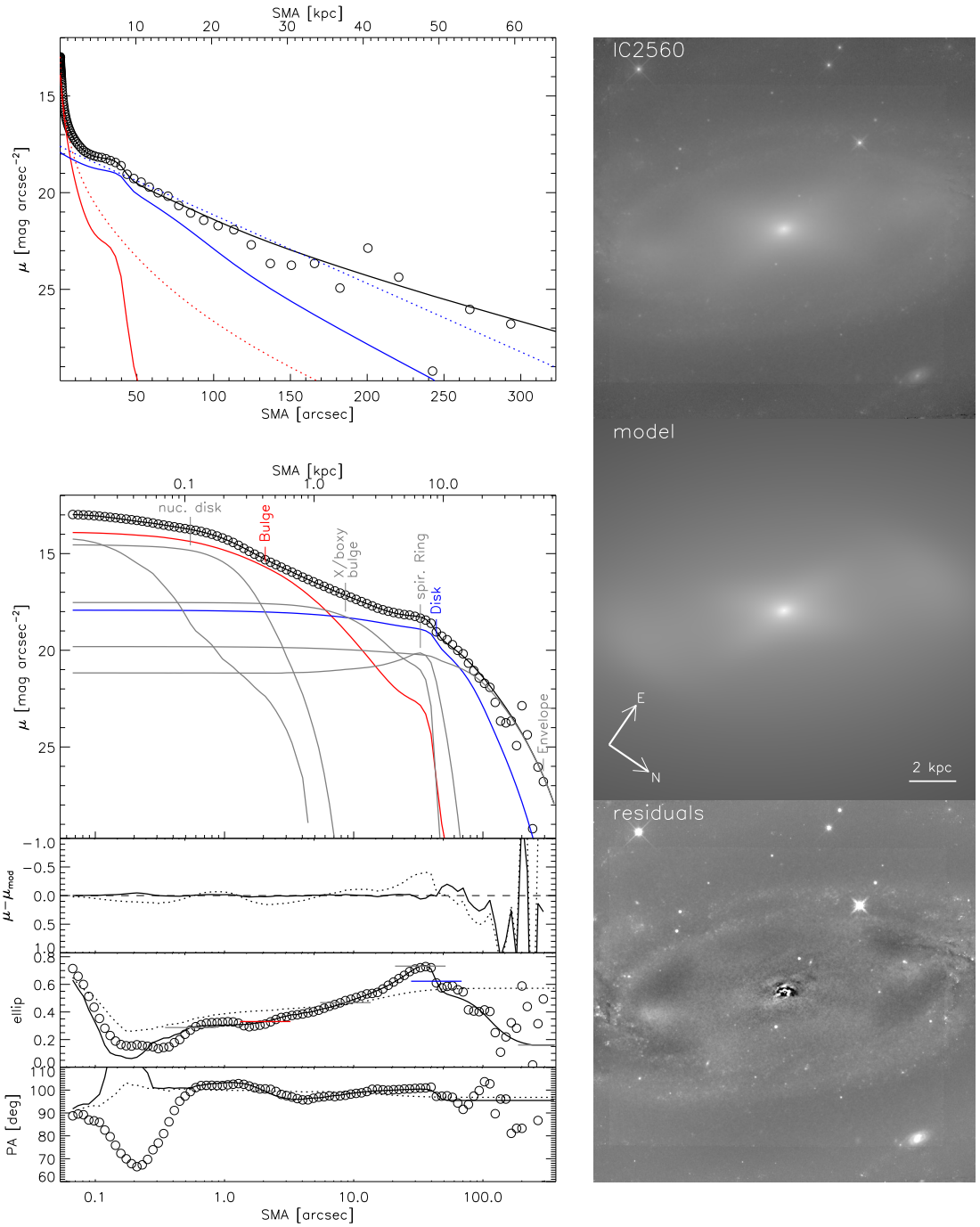

FIG. 9.— IC2560 photometric data and model. *Left panels:* semi-major axis (SMA) profiles of H-band surface brightness (μ), data-model residuals ($\mu - \mu_{\rm mod}$), ellipticity (ellip), and east-of-north position angle (PA). Open circles show the observed data, and solid lines the full model (thick black), its bulge (red), main exponential disk (blue), and all other model components (thin grey lines). For comparison with our best-fit model, shown by the dashed lines are total (black), bulge (red) and disk (blue) profiles of the "basic model", which includes only a bulge and disk (for IC2560, the point source could not be fitted in the basic model as the best-fit bulge+disk model overpredicts the central flux). The top-left panel plots *mu* against linear SMA and shows the basic model bulge and disk, while the lower panels use a logarithmic SMA scaling and omit the basic model components for better visibility of the full model's multiple components. See Figure 10, for the basic model components' $\mu - \log(\mathrm{SMA})$ profiles. The names and ellipticities (horizontal bars) of the full model's components are indicated at the SMA distances where the components' contribution to the total flux is maximal. In IC2560's full model, the envelope accounts for the strongly increased flattening at $\gtrsim 20$ kpc, the spiral arms are tightly wound and hence modeled by a ring with inner truncation, and the X-shaped pseudobulge by a Sérsic with best-fit index $n = 0.5$ and a 4th-order isophote harmonic. *Right panels, from top to bottom:* the image data and full model on a logarithmic greyscale, and full model residuals on a linear greyscale. Evident is a residual spiral structure in the innermost regions, presumably from an unmodeled nuclear disk.

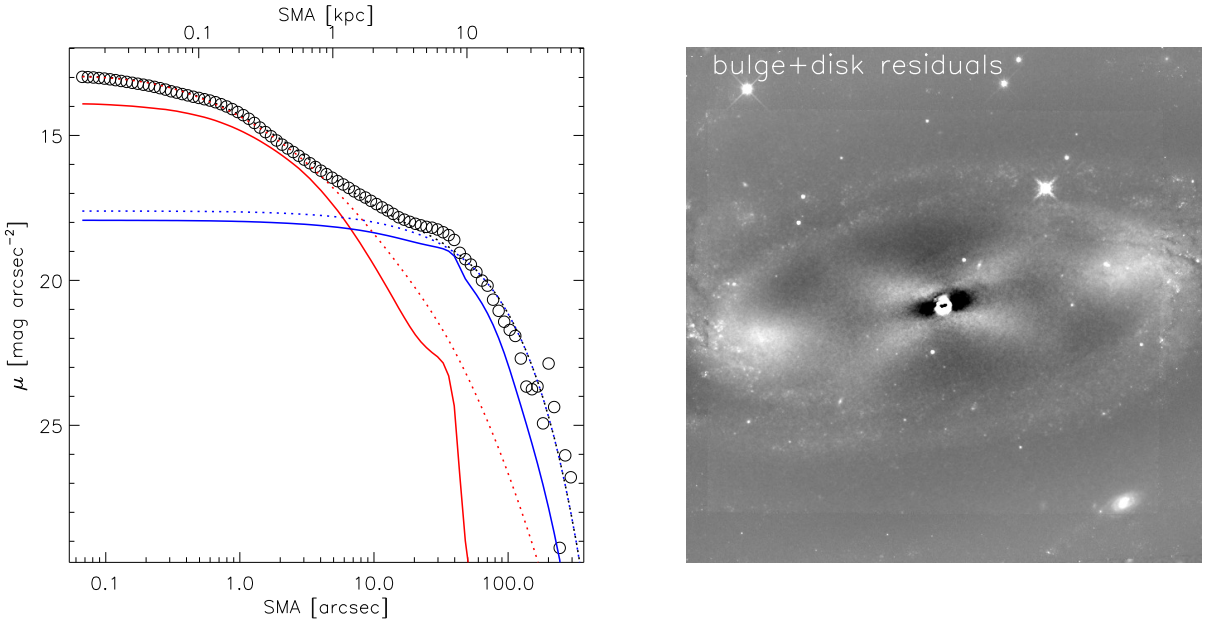

FIG. 10.— IC2560 photometric data and model, continued from Figure 9. *Left panel:* logarithmic semimajor-axis (SMA) H-band surface brightness (μ) of the data (open circles), full model (solid lines) and basic bulge+disk model (dashed). The black lines represent the total model μ, red the bulge, and blue the disk contribution. The other components of the full model are not shown (but see Figure 9. *Right panel:* data-model residuals of the basic (bulge+disk) model. The bright onset of the spiral arms is unaccounted for, as well as the X-shaped pseudobulge. The central brightness is overpredicted by the basic model, and therefore the point source cannot be fitted before the mentioned components are included in a full model.

NGC 2273

NGC2273 (Figures 13 and 14) is a nearby (26 Mpc) spiral galaxy with several prominent rings and a central disk. Due to the proximity of the galaxy, the inner structure is well-resolved and the galaxy extends $\sim 100''$ on the sky. At the largest radii (SMA $\gtrsim 60''/7.5$ kpc), the light distribution is flattened ($q \sim 0.6$) with a major-axis PA of about 140 deg E of N. The ends of the spiral arms are also visible. Further inwards, the arms dominate the light. They are tightly wound, forming a broad ring at $10 - 20''$ ($1.3 - 2.5$ kpc) along the SMA. The ellipticity of the ring is lower than that of the outer disk, and the PA is misaligned by about +40 deg from the outer disk. The spiral arms emerge from opposite sides of an apparent bar, which thickens to become lens-like towards the center. Located well inside this bar/bulge region, at SMA $= 2''$ (250 pc), is a bright and slightly asymmetric nuclear ring and disk (Mulchaey et al. 1997; Erwin & Sparke 2003; Gu et al. 2003) with similar PA and axis ratio as the outer disk (see also Petitpas & Wilson 2002; Barbosa et al. 2006; Falcón-Barroso et al. 2006). In the galaxy center, near the resolution limit, the brightness rises steeply. This feature appears round and is $1''$ (130 pc) in diameter. It is either an inner bulge or a barely resolved star cluster.

Starting with a basic bulge+disk+psf model (Figure 1), the best-fit bulge component traces the light of the nuclear ring, while the disk component broadly accounts for the main spiral arms. We improve on the basic model by adding a nuclear ring, bar, and spiral arms (Figure 2). We find a Gaussian profile with inner truncation for the nuclear ring and the spiral component. We found that this choice fits the data better than an exponential, and avoids the degeneracy of the more general Sérsic profile in the presence of the simultaneously adjustable truncation parameters. The bar component is a Sérsic with $n \sim 0.2$ and boxy isophotes (Fourier amplitude $a_4 = -0.1$) as expected. The bulge and nuclear disk components are oriented along the (outer) major axis (~ 50 deg E of N), while the bar component is rotated by a relative +80 deg. The large-scale disk provides a good fit beyond $\gtrsim 20''$(2.5 kpc) aside from the spiral arms themselves, which cannot be robustly modeled.

We bracket systematic uncertainties in our reference model with three additional models. Replacing the exponential disk by a Sérsic profile leads to a 0.2 mag reduction in the classical bulge light, and the disk index of $n = 1.5$ shows that the corresponding component indeed traces the exponential part of the profile. We test the effect of removing the bar, which was visually confluent with the bulge, and obtain a 0.6 mag increase in bulge flux. In this modification, the classical bulge R_e increases by a factor of two, becomes steeper ($n = 3.8$ versus the reference $n = 2.1$), and effectively accounts for most of the light inside the spiral ring. However, this model without a bar results in strongly increased residuals, and we thus prefer to include the bar. Finally, we test using a Sérsic profile for the nuclear ring and model a nuclear disk instead of the ring. We find virtually unchanged classical bulge parameters, but significantly elevated residuals in the latter case. The resulting low Sérsic index (0.1) of the disk also suggests that an inner truncation is appropriate to model the nuclear disk. In conclusion, we arrive at a conservative systematic uncertainy of 0.4 mag for the classical bulge magnitude of NGC2273.

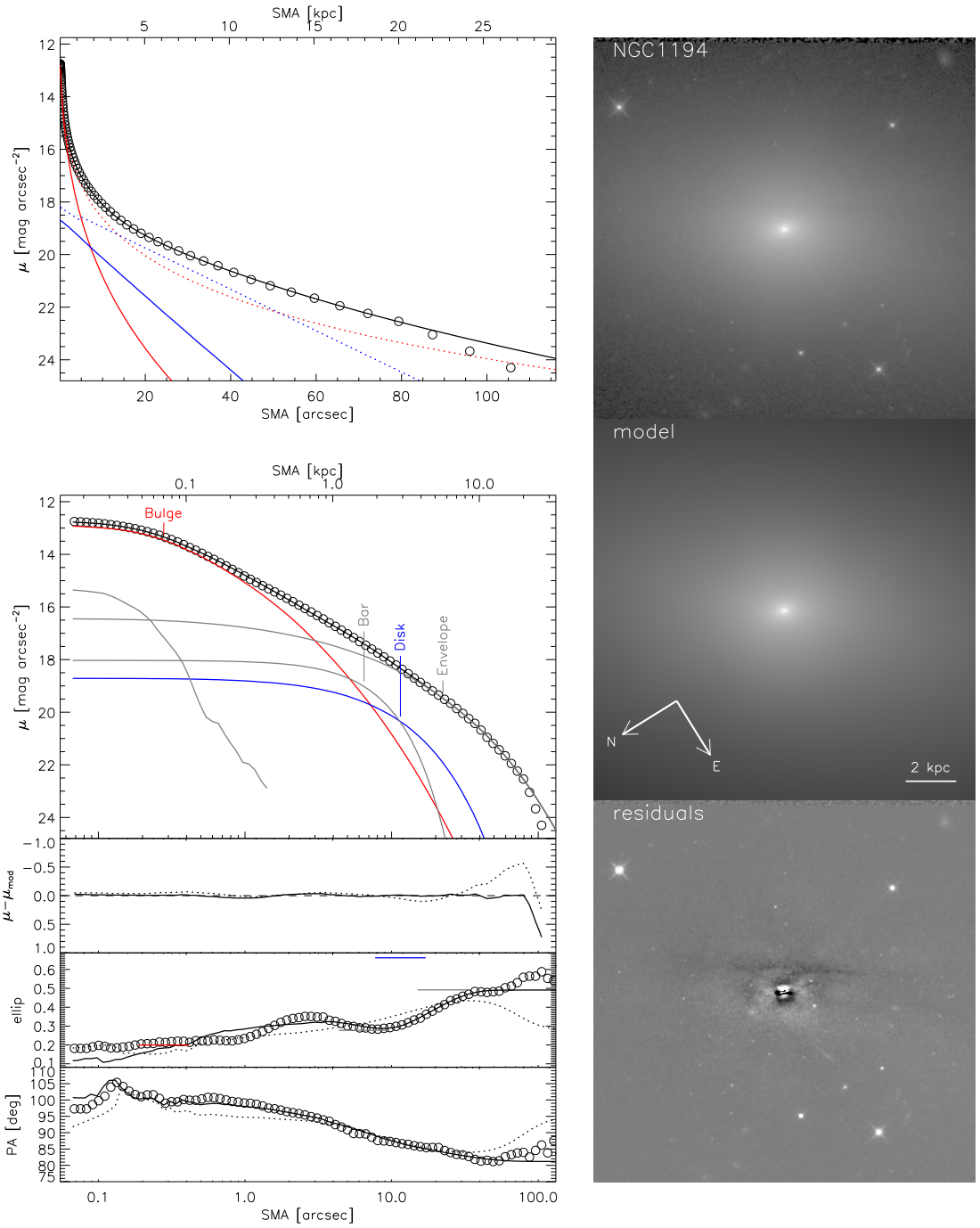

FIG. 11.— NGC1194 photometric data and model, with layout as in Figure 9. *Left panels:* semi-major axis (SMA) profiles of H-band surface brightness (μ), data-model residuals ($\mu - \mu_{\rm mod}$), ellipticity (ellip), and east-of-north position angle (PA). Open circles: data, solid lines: full model, dashed lines: basic (bulge+disk) model. Thick black: total model image profiles, red: bulge, blue: disk, and thin grey: all other components. Only select profiles are shown in the $\mu - {\rm SMA}$ (top panel) and $\mu - \log {\rm SMA}$ (second from top) plots (see also Figure 12). Ellipticities of individual components are indicated by horizontal bars. *Right panels:* Images of the data, model and residuals. In the full model, the envelope component is required to allow the point source to be fitted; otherwise, the bulge is too bright in the center with a comparatively high ($n \sim 7$) Sérsic index. It also provides the higher flattening in the outer parts compared to the bulge, which otherwise (in the basic model) dominates the light at $\gtrsim 10\,$kpc. The intermediate-scale ($\sim 2\,$kpc) component is tentatively termed "bar" here for its compact profile (Sérsic $n \sim 0.8$) and $\sim 90\,$deg PA offset from the disk major axis. It is strong enough to be required for fitting the disk and envelope separately.

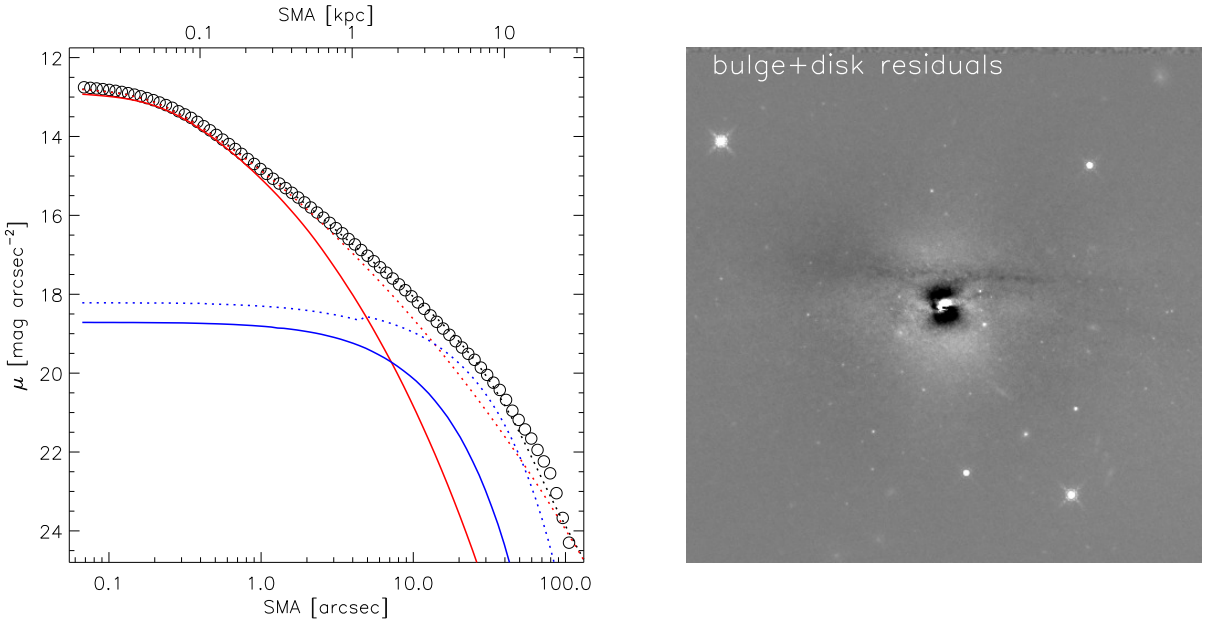

FIG. 12.— NGC1194 photometric data and model, continued from Figure 11. *Left panel:* SMA surface brightness (μ) of the data (open circles), full model (solid lines) and basic bulge+disk model (dashed), separately for total light (black), bulge (red) and disk (blue). *Right panel:* image of the basic model residuals. In this basic model, which in particular does not include the envelope component, the bulge outer profile is too extended and does not follow the downturn ("knee") at $\sim 80''$ (~ 20 kpc). The excess brightness of the compact "bar", which is slightly elongated along the minor axis (here: vertical orientation) can also clearly be spotted in the basic model residuals, as well as the dust lane parallel to the major axis.

NGC 2960

NGC2960 (Figures 15 and 16) is a bulge-dominated galaxy with a kpc-scale embedded disk. Its semi-major axis is oriented 150 deg East of North, and the average flattening is rather low, $q \sim 0.7$. The radial surface brightness profile appears to exhibit a bulge-disk structure of a typical lenticular galaxy, with a prominent steepening of the profile inside $\sim 13''$ (4.5 kpc) and an exponential decline outside. However, two salient features distinguish NGC2960 visually from a simple lenticular: the increase of ellipticity towards the center, and an inner (SMA $\sim 8''/2.7$ kpc) flocculent and dusty disk. The residual image of a basic bulge+disk model (Figure 15) reinforces the impression of a dusty disk, and reveals embedded asymmetric spiral structure. The residual image also shows that a highly inclined nuclear disk (residuals at SMA $\lesssim 1.5''/500$ pc) is responsible for the low ellipticity at the smallest radii. Both the nuclear disk and the kpc-scale disk are indicated by separate ellipticity peaks ($e \sim 0.4$ respectively) at radii corresponding to their visual dominance.

By contrast, the large-scale component is round ($q \sim 0.8$) and the round, smooth and dominant outer component morphologically resembles an elliptical galaxy. We thus might interpret this large-scale component as the bulge, despite its exponential profile. At the largest radii at which the light distribution can be traced, from $80''$ (30 kpc) to $30''$ (10 kpc), the profile again flattens and is marked by tidal or shell-like features that can be seen even in the science frames. These features indicate that NGC2960 has undergone a recent interaction. The merger may have distorted the radial brightness profile of the bulge, resulting in a mostly exponential shape with a marked upturn only at the largest radii.

The basic bulge+disk model includes a flat "bulge" that over-predicts the central flux. To extract the bulge parameters more reliably, and to account for the disks, we add an additional nuclear component with a Sérsic profile (Figure 15). Both inner components converge to relatively compact profiles ($n = 1.4$ and 0.5). The comparison of this 4-component model with the data profile makes it clear that both inner components trace the light of nuclear and kpc-scale disk, and that the inner region is reasonably fit by these two components alone. We have also explored models with an additional central bulge, resulting in five components (including the central point source). However, the residuals barely improve, and the corresponding "bulge" component is still significantly flatter ($q = 0.6$) than the large-scale outer profile. We thus do not include this additional component. We have also accounted for the outermost, very flattened light by a separate component, but find that its inclusion does not affect the parameters of the other components.

Given these many complications, we do not find a clear classical bulge component in NGC2960; instead the center is fit by the sum of the two disks. We judge that the third, large-scale component corresponds best to a classical bulge, even with a low best-fit Sérsic $n \sim 1$. For comparison, Vika et al. (2012) have fitted a two component model here, and interpreted the inner component as the bulge, which, given its size, presumably fits both the nuclear and the kpc-scale disk simultaneously and is hence more flattened than the outer component (the "disk" in their interpretation). The Vika et al. 2012 model hence corresponds to our basic model, which does not account for separation of the two inner

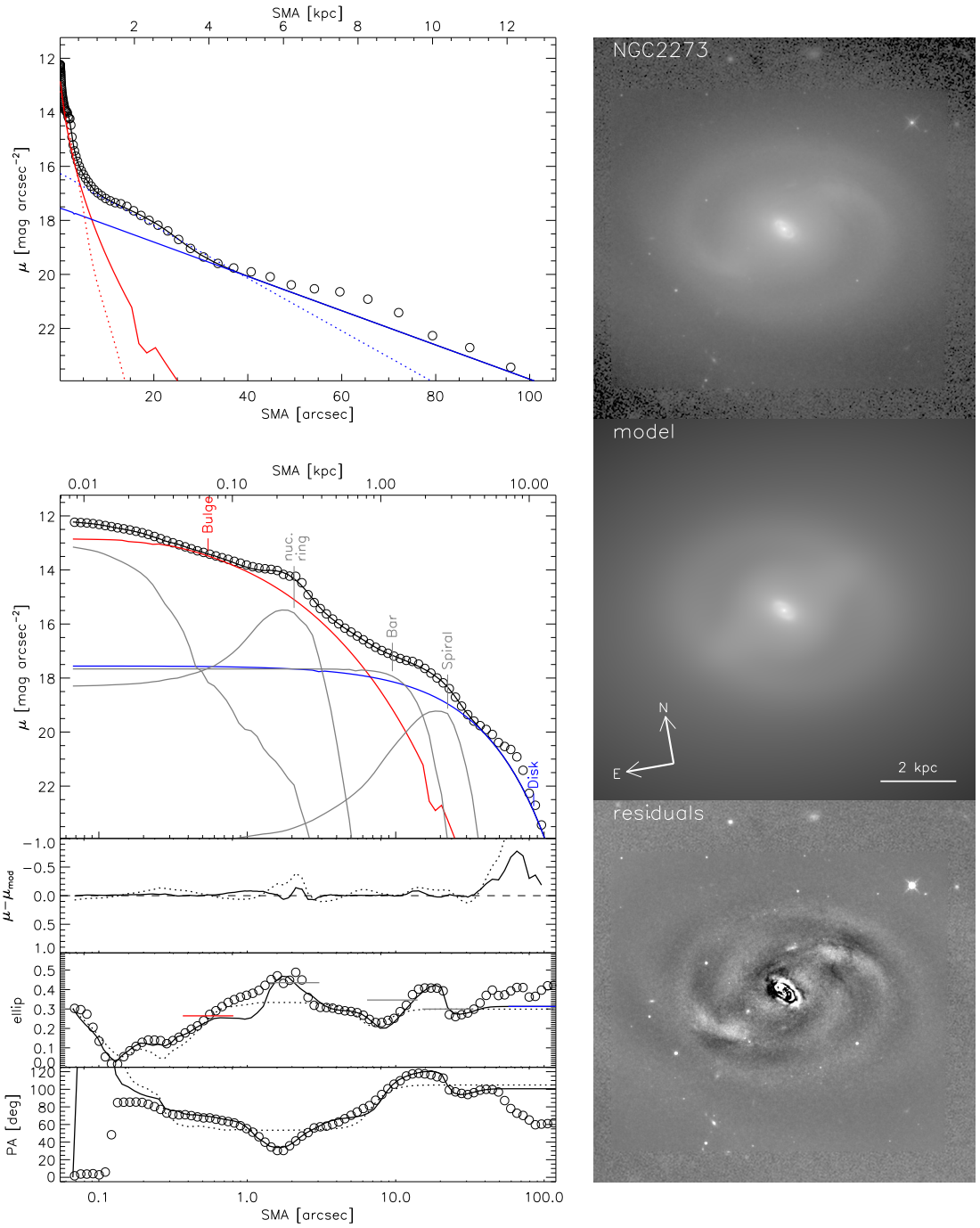

FIG. 13.— NGC2273 photometric data and model, with layout as in Figure 9. *Left panels:* semi-major axis (SMA) profiles of H-band surface brightness (μ), data-model residuals ($\mu - \mu_{\rm mod}$), ellipticity (ellip), and east-of-north position angle (PA). Open circles: data, solid lines: full model, dashed lines: basic (bulge+disk) model. Thick black: total model image profiles, red: bulge, blue: disk, and thin grey: all other components. Only select profiles are shown in the $\mu-$SMA (top panel) and $\mu-\log$SMA (second from top) plots (see also Figure 14). Ellipticities of individual components are indicated by horizontal bars. *Right panels:* Images of the data, model, and residuals. The full model traces the data much better than the basic model, in particular regarding ellipticity and PA. It models the spiral arms by a ring with inner truncation, and dispenses with modeling the rotation of the arms as they are too tightly wound for a stable fit. The other prominent features are the bar (Sérsic profile with best-fit $n \sim 0.2$) and the nuclear disk and ring, which are both modeled by one component with a Gaussian profile and an inner truncation applied. The outer disk and (faint) spiral structure are not shown on the image area and are not separately modeled as their degeneracy with the main exponential disk is large.

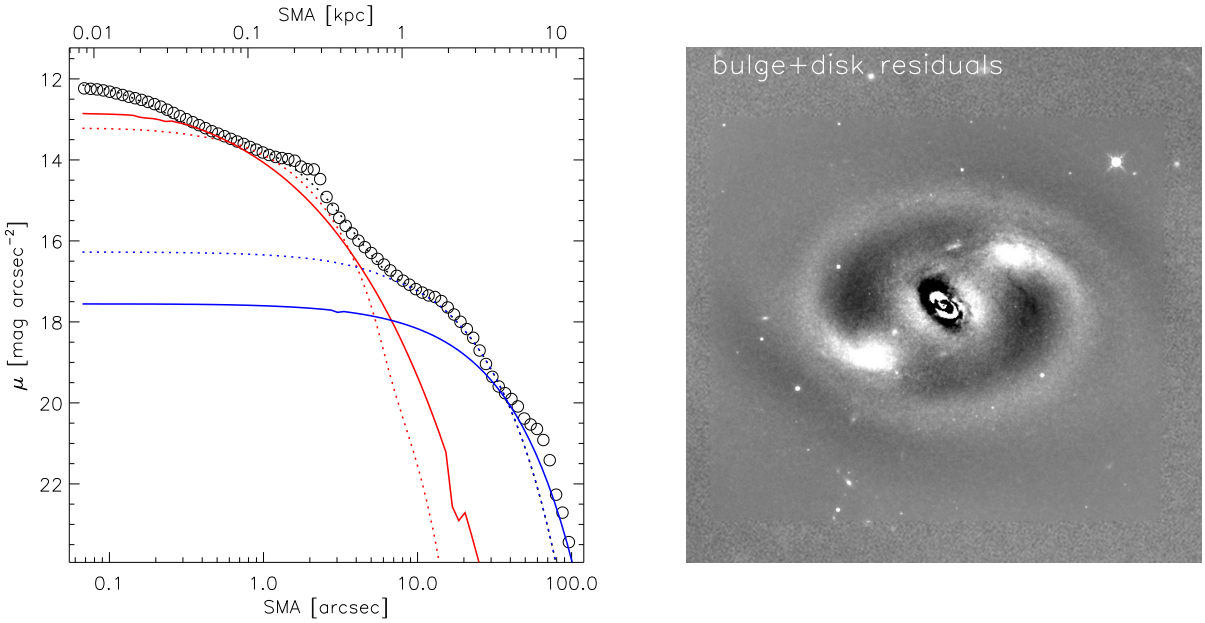

FIG. 14.— NGC2273 photometric data and model, continued from Figure 13. *Left panel:* SMA surface brightness (μ) of the data (open circles), full model (solid lines) and basic bulge+disk model (dashed), separately for total light (black), bulge (red) and disk (blue). *Right panel:* image of basic model residuals. In both the profiles and residuals it is clear that the basic model cannot account for the nuclear disk (near SMA $\sim 2''$, or ~ 250 pc) and cannot distinguish the extended profile of the main disk from the compact profile of the spiral arms (the "knee" at $\sim 20'' \,/\, 2$ kpc)

components and their clear disk morphology. We speculate that the kpc-scale disk was recently accreted and thus still contains gas and spiral structure. If we take one or both of the inner disks as the "bulge" instead, then the magnitude drops by $0.4 - 1.4$ mag. Other modifications, like allowing a Sérsic instead of exponential profile for either disk, or including an envelope, have comparatively minor effects on the bulge parameters. The alternative models provide us with a 0.6 mag estimate of the systematic bulge magnitude uncertainty.

NGC 3393

NGC3393 (Figures 17 and 18) is a late-type galaxy that contains two prominent rings. It is probably seen face-on based on the round outer disk, which extends to $\sim 80''$ (21 kpc). The large-scale disk is slightly lopsided towards -50 deg E of N, and features two asymmetric spiral arms with prominent star-forming regions. The arms barely connect to the galaxy center and broadly resemble a ring, which is clearly indicated by the peak in the SB profile at $40''/10$ kpc. The inner ring at intermediate radii (SMA $= 13'' \,/\, 3.5$ kpc) is much more elongated and has a lower axis ratio than the outer disk. The ring might be the star-forming boundary of a large-scale bar. The innermost region ($\lesssim 2''/0.5$ kpc) appears to be dominated by the bulge, i.e. a steep increase in surface brightness and round isophotes. It harbors yet another bar-like light distribution, with a PA 140 deg E of N, which is misaligned by -20 deg from the major axis defined by the inner ring.

Fitting and removing the basic model (bulge+disk+nucleus, see Figure 18) exposes residuals from the bar and each ring. The basic fit yields an extended ($6.4''/1.6$ kpc and $n = 3.5$) "bulge" component that effectively accounts for all the light at and inside the inner ring and is more flattened ($q = 0.7$) than the outer disk.

We improve the NGC3393 model by adding separate components for the central bar and both rings. With $n = 0.25$ and $q = 0.4$, the bar is compact and flattened as expected. We model the rings with Gaussian profiles ($n = 0.5$) but use an inner truncation so that the ring light does not eat away the disk. This, our best-fit model, has classical bulge parameters $m = 11.2$ mag, $R_e = 2.4''$ (0.6 kpc), $n = 2.6$ and $q = 0.97$. This is 1 mag fainter than the bulge in the basic bulge+disk model, and 0.2 mag brighter than for the intermediate model without truncations. We adopt this difference as a rough estimate of the systematic bulge magnitude uncertainty.

NGC 4388

NGC4388 (Figures 19 and 20) is a spiral galaxy seen at high inclination (disk $q = 0.35 \;\rightarrow\; i \gtrsim 70$ deg). The tightly-wound spiral arms are visually defined between SMA ~ 30 and $50''$ (2.8 and 4.6 kpc). They form a ring that can be identified in the surface brightness and ellipticity profiles. In the center of NGC4388 there is a bright, central ($\lesssim 2.5$"$/200$ pc) disk, seen almost edge-on with very low axis ratio, and at a ~ -15 deg misalignment from the large-scale major axis. The entire region interior to the ring contains several dust lanes. Outside of the spiral/ring, the profile has two nearly exponential parts, with a change to a larger scale radius (factor of several) and ellipticity (by ~ 0.2) occurring at ~ 80" (7 kpc). We identify the inner exponential as the main disk, while the outer exponential "envelope" as a very extended disk, due to its high flattening ($q \sim 0.1$) and ~ 100" (9 kpc) scale radius.

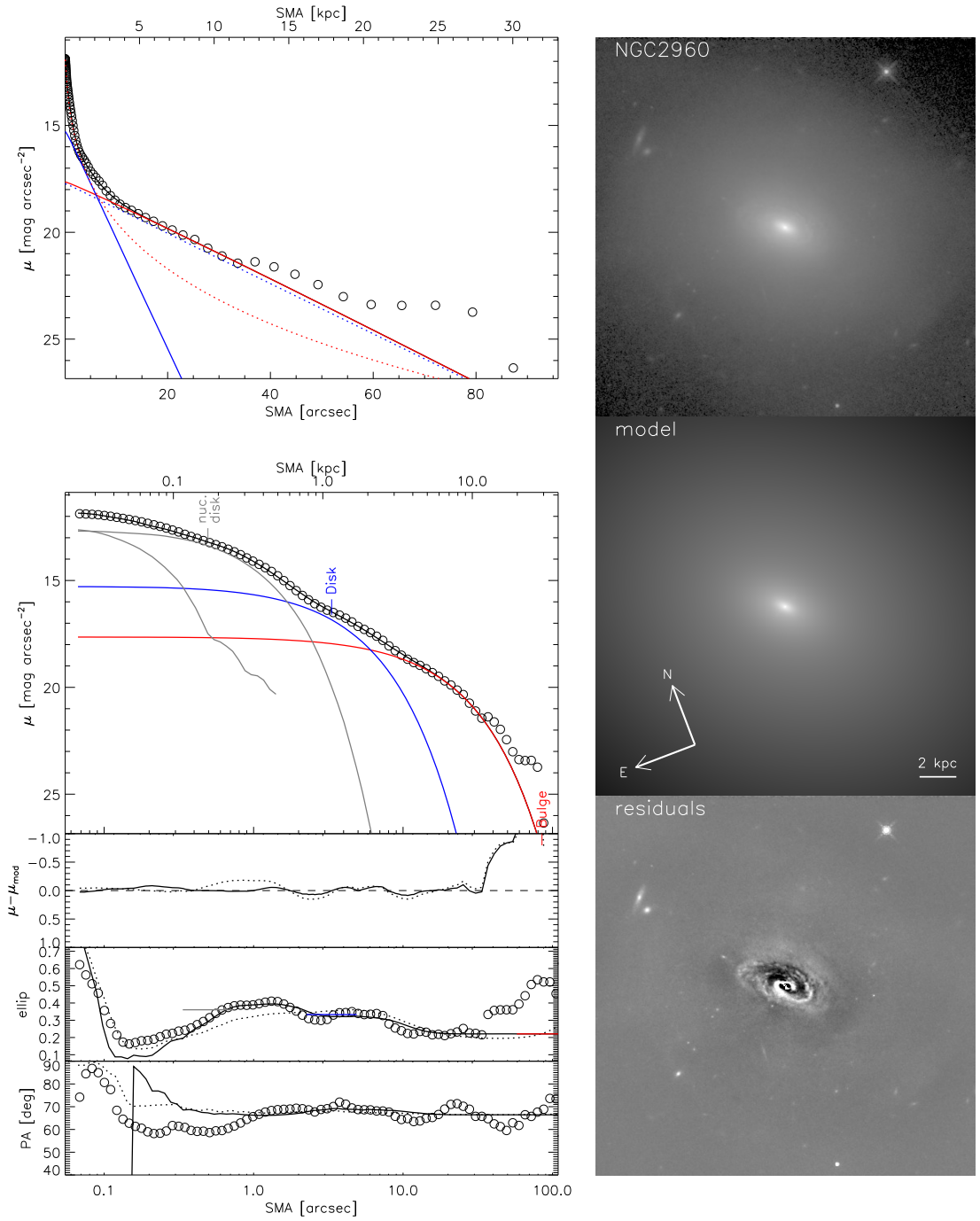

FIG. 15.— NGC2960 photometric data and model, with layout as in Figure 9. *Left panels:* semi-major axis (SMA) profiles of H-band surface brightness (μ), data-model residuals ($\mu - \mu_{\rm mod}$), ellipticity (ellip), and east-of-north position angle (PA). Open circles: data, solid lines: full model, dashed lines: basic (bulge+disk) model. Thick black: total model image profiles, red: bulge, blue: disk, and thin grey: all other components. Only select profiles are shown in the $\mu -$ SMA (top panel) and $\mu - \log$SMA (second from top) plots (see also Figure 16). Ellipticities of individual components are indicated by horizontal bars. *Right panels:* Images of the data, model and residuals. The steepening of the profile inside $\sim 13''$ (4.5 kpc) apparently signals a bulge, but the increased flattening inside $\sim 13''$ (4.5 kpc), the flocculent spiral arms, the dust lanes and two-part inner profile (inflection at ~ 1 kpc) originate in a nuclear (~ 100 pc-scale) and kpc-scale star-forming disk that dominate the light in this region. We identify the smooth and round part of the galaxy outside of these two disks as a likely bulge, and surmise that its near-exponential profile (i.e. its relatively low Sérsic index) is a result of a recent merger, which is likely also responsible for the profile distortions and light excess at the largest observable radii ($\gtrsim 50''$ / 6 kpc).

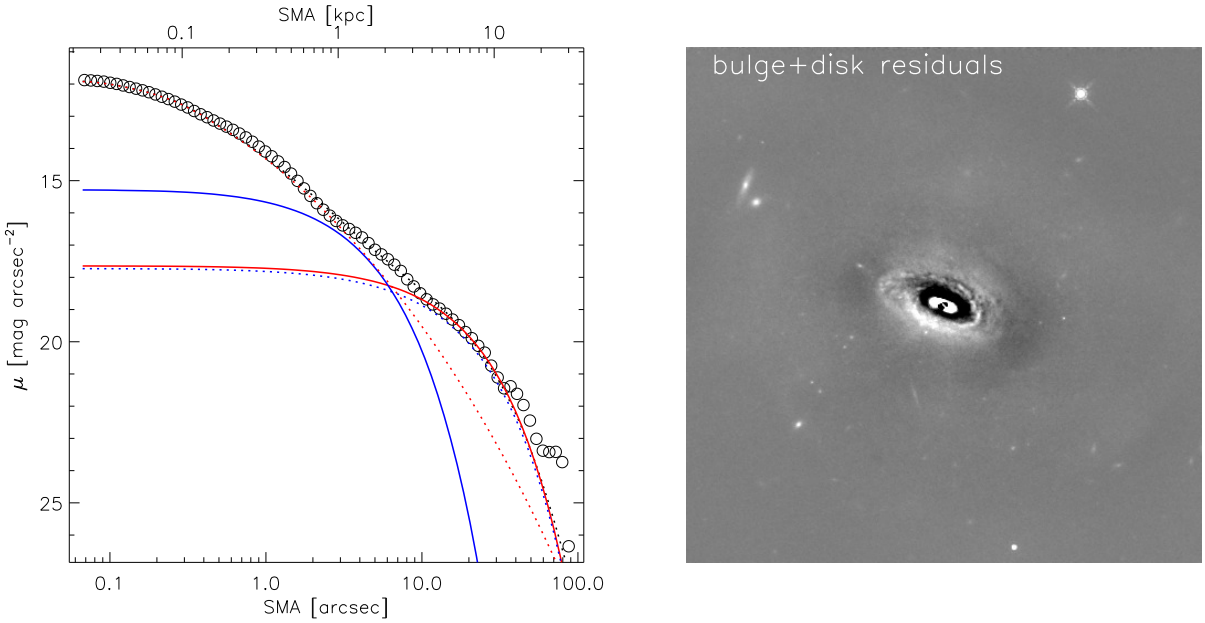

FIG. 16.— NGC2960 photometric data and model, continued from Figure 15. *Left panel:* SMA surface brightness (μ) of the data (open circles), full model (solid lines) and basic bulge+disk model (dashed), separately for total light (black), bulge (red) and disk (blue). *Right panel:* image of basic model residuals. The nuclear and kpc-scale starforming disk are clearly evident in the basic model residuals.

In addition to the bulge, disk and nucleus (point source), we account for the nuclear disk, spiral arms, and envelope with exponential profiles. The spiral arms are modeled as a ring with an inner truncation. To reduce degeneracy, we chose an exponential instead of a Sérsic profile for the spiral ring, and force the bulge, disk and envelope to share a common PA. The best-fit bulge of our adopted reference model is very round ($q \sim 0.8$, compared to the disk $q \sim 0.3$), has an intermediate Sérsic index $n = 2.2$, and boxy isophotes. The nuclear disk dominates the surface brightness in the center, and the PA of the model component converges to the observed value, which provides confirmation that this component is suitably accounted for in our adopted model (see also discussion of the nuclear disk from the kinematics as observed by SINFONI in Greene et al. 2014). The outer envelope also makes a significant difference to the fit in this case, changing the bulge magnitude by -0.5 mag.

Of the various models we fitted, we mention here the model with a Sérsic profile (instead of exponential) for the nuclear disk, a Sérsic for the main disk, and a model without the envelope component. These result in classical bulge magnitude changes of $+0.7$, -0.3 and -0.5 mag, respectively, and lead us to a systematic bulge magnitude uncertainty estimate of 0.5 mag. For reference, the classical bulge in the best-fit bulge+disk+point-source model is 0.3 mag fainter than in our adopted 6-component model.

NGC 6264

NGC6264 (Figures 21 and 22) is dominated by a bar and a pair of smooth spiral arms. A distinct bulge is not immediately visible, but there is a small ($\sim 0.3''/200$ pc) and round central light concentration embedded within the conspicuous bar. The bar is apparent also in the local maximum around 5" (3 kpc) in the surface brightness and ellipticity profiles at constant PA. Within $\sim 5''$ (350 pc), the PA profile shows a ~ 10 deg step, and grows considerably rounder towards smaller radii, suggesting that we are seeing an underlying bulge.

The spiral arms are smooth and show little signs of star formation, perhaps due to the decreased spatial resolution (~ 100 pc at the distance of 136 Mpc). The tightly wound spiral arms emerge from the ends of the bar, then become clearly defined at larger radii and obtain full strength around SMA ~ 10" (7 kpc). This region is marked by a local maximum in the surface brightness, ellipticity and PA profiles, followed by a rapid brightness drop towards larger radii. At $\sim 30''$ (20 kpc) the surface brightness profile transitions into a faint (~ 23 mag arcsec^{-2}) floor that we interpret as an envelope or halo that is traceable out to $50''$ (35 kpc).

When fitted with a basic model (bulge, disk and point source), the "bulge" component is more flattened than the "disk" and appears to predominantly fit the light of the bar. Round residuals near the center expose an underlying rounder light distribution, i.e. the probable bulge. We add another Sérsic component to directly model the bar. The residuals in this second fit are greaty improved, and we find a small bulge component ($R_e = 1''/0.7$ kpc, $q = 0.7$), and a larger flat ($R_e = 4''/2.6$ kpc, $q = 0.4$) and compact (Sérsic $n = 0.5$) component, as expected for a bulge and a bar. Using an exponential profile with inner truncation and powerlaw rotation, we model the spiral arms and the underlying exponential disk component. The adopted 4+1-component model (bulge, disk, bar, spiral, plus the nuclear point source) is a good fit aside from a possible outer envelope (or halo), which was too faint to be fit robustly. We choose not to account for the latter by another component, as it converges to a very large ($R_s = 100$"/70 kpc) scale, suggesting a degeneracy with the background uncertainty.

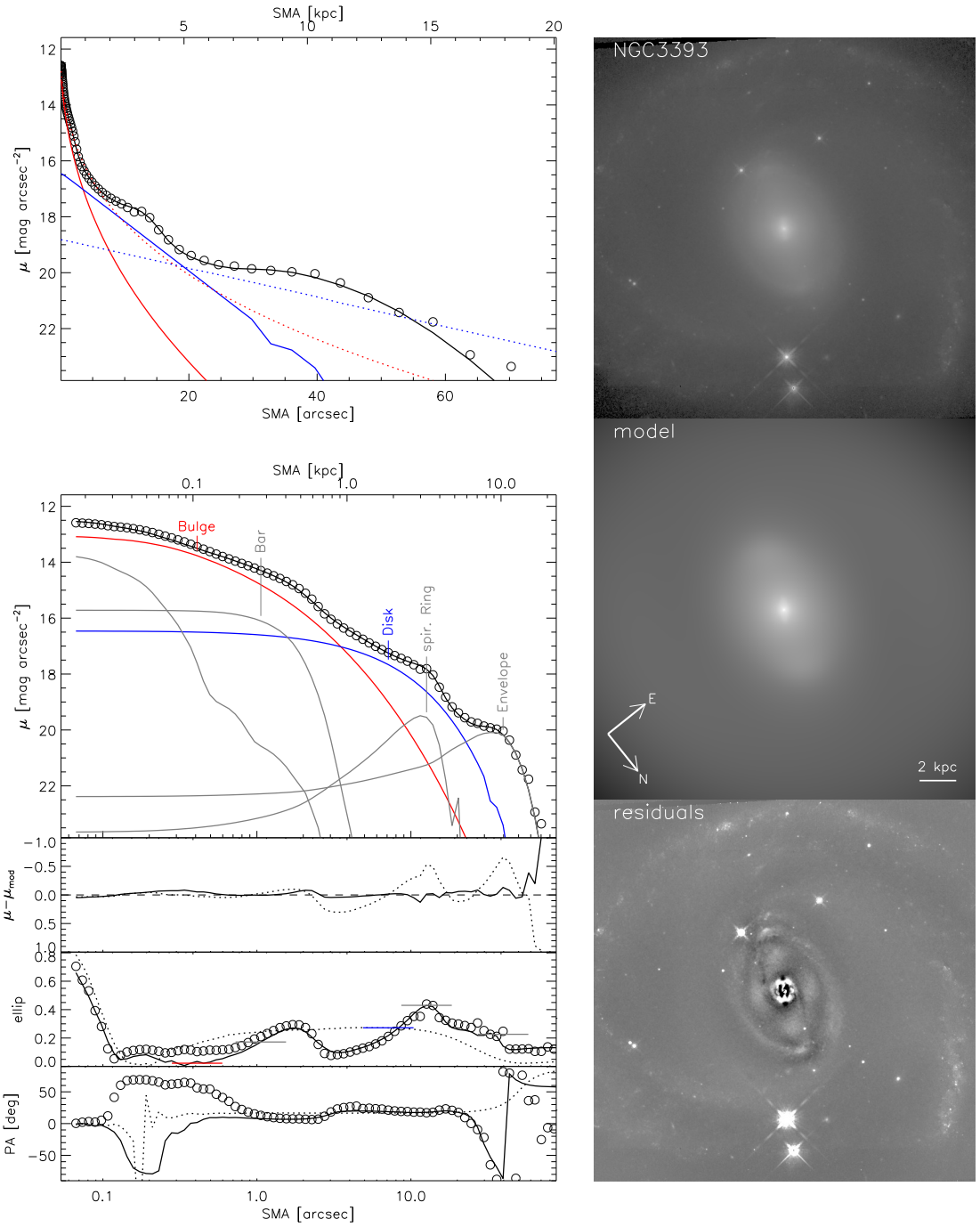

FIG. 17.— NGC3393 photometric data and model, with layout as in Figure 9. *Left panels:* semi-major axis (SMA) profiles of H-band surface brightness (μ), data-model residuals ($\mu - \mu_{\rm mod}$), ellipticity (ellip), and east-of-north position angle (PA). Open circles: data, solid lines: full model, dashed lines: basic (bulge+disk) model. Thick black: total model image profiles, red: bulge, blue: disk, and thin grey: all other components. Only select profiles are shown in the $\mu -$ SMA (top panel) and $\mu -$ log SMA (second from top) plots (see also Figure 18). Ellipticities of individual components are indicated by horizontal bars. *Right panels:* Images of the data, model and residuals. In addition to bulge, disk and central point source, the full model features all major visible structures: the nuclear bar ($\sim$ 500 pc scale) oriented ~ -35 deg E of N (roughly vertical on the shown image); the bright elongated ring, which appears to delineate the boundary of a $\sim$ 3 kpc bar; and an outer round ring (flattening near zero) which appears to consist of weakly defined and tightly wound low-surface brightness spiral arms and marks the boundary of the visible disk (seen in the corners of the field shown here). Both rings have a Gaussian profile and an inner truncation. The residuals suggest an additional nuclear ring that touches the ends nuclear bar, but it is not separately modeled due to ensuing excessive model degeneracy.

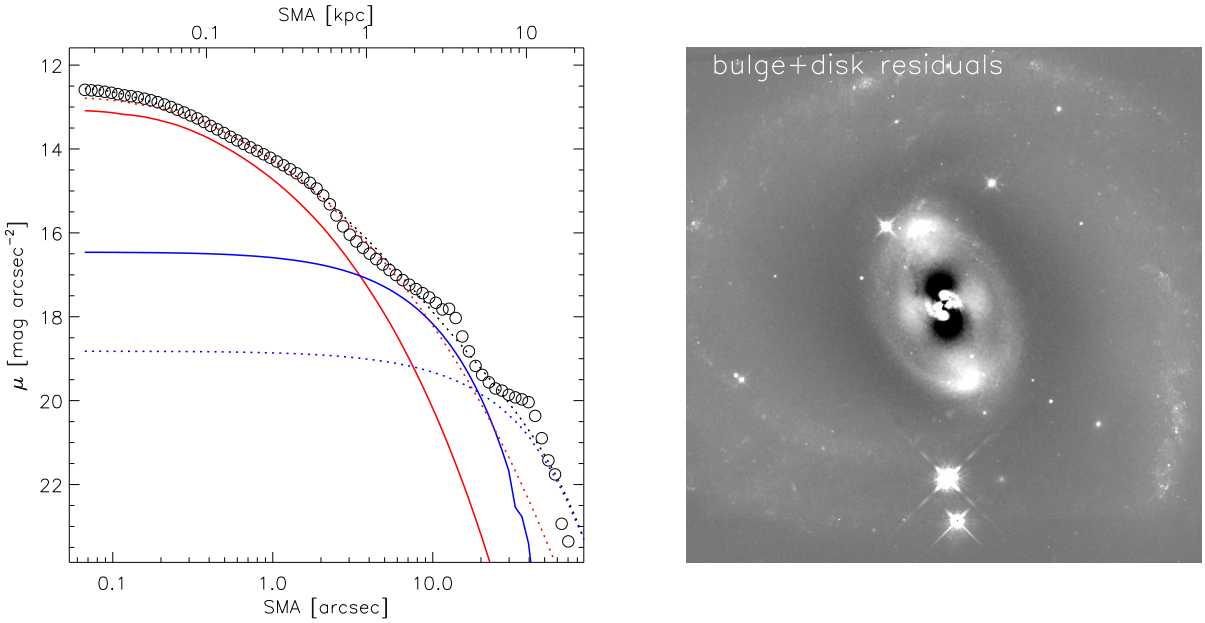

FIG. 18.— NGC3393 photometric data and model, continued from Figure 17. *Left panel:* SMA surface brightness (μ) of the data (open circles), full model (solid lines) and basic bulge+disk model (dashed), separately for total light (black), bulge (red) and disk (blue). *Right panel:* image of basic model residuals. The inability of the basic model to represent the galaxy light is evident, and the basic model residual image exposes both the intermediate ring (elongated) and the outer ring (round, faint spiral structure). The nuclear bar is not clearly visible here, but indicated still by the central isophotal twist.

We experimented with alternatives to this adopted model, and quote the change of bulge magnitude incurred by some of these modifications. Using a Sérsic instead of exponential profile for the disk, or adding an exponential component for the envelope (halo), results in a 0.4 and 0.2 mag fainter bulge, respectively. Modeling bar and bulge with only one Sérsic profile, but retaining the spiral component apart from disk and AGN leads to a much brighter bulge (-1.9 mag), with classical bulge parameters that are close to those of the basic model parameters and differ by -1.4 mag in $m_{\rm bul}$ from the reference model. As a conservative estimate, we thus assign a bulge magnitude uncertainty of 0.7 mag.

NGC 6323

NGC6323 (Figures 23 and 24) is a spiral galaxy at high inclination with an apparent disk axis ratio of ~ 0.4. There is a ring at SMA = 8" (4 kpc), from which two flocculent and unequal-strength spiral arms emerge and extend to SMA ≈ 10 kpc from the center. The main disk profile exhibits a weak truncation at SMA > 20 kpc that is recognizable in the image as the visible boundary of the disk. An inner (4 kpc) ring is clearly seen in the surface brightness profile, delineating the transition from a low-ellipticity, bulge-dominated inner region to a flatter disk-dominated region. A nucleus or small bulge can be distinguished visually within the inner two arcseconds.

The basic bulge+disk+nucleus model fares surprisingly well at emulating the radial profile. However, significant structure remains in the residual image, including spiral arms and a ring from which they appear to emerge, as well as a central misaligned elongated structure whose ends coincide with the ring. We therefore construct a model that includes a spiral component modified by coordinate rotation and inner truncation, as well as a very compact, low-n Sérsic profile with high flattening that accounts for light between the bulge and the spiral arms and may be interpreted as a large-scale bar. This additional component also effectively also removes the ring-like residuals at the onset of the spiral structure. Coincidentally, despite the addition of two components, the best-fit bulge parameters of the reference model are only marginally different from that of the basic model ($m_{\rm bul} = 15.5$ mag instead of 15.4 mag, and similarly for the bulge R_e and n). The bulge is about 2 mag fainter than the disk, $R_e = 1.3''$ (0.65 kpc) in size, and has a near-exponential profile. Allowing a 4th-order Fourier mode for the bulge isophotes gives a boxy shape (amplitude ~ 0.1). The spiral is modified by Fourier modes (4th order and lower), which enables fitting of the asymmetry in the spiral arms and a better convergence of the rotation function.

We explore multiple alternative models and find that, while formally increasing residuals (χ^2), for some of them the residual images and radial profile mismatches differ only in details. Removing the bar/ring component decreases the bulge brightness by 0.2 mag, and omitting the spiral arm component instead changes $m_{\rm bul}$ by less then 0.1 mag. Testing a model where the disk has a Sérsic profile instead of an exponential gives a 0.2 mag brighter bulge, and a disk Sérsic index of 0.9. The lowest change in residuals, but biggest change in $m_{\rm bul}$, occurs when we apply a truncation to the bar/ring instead of the spiral arm component, obtaining a 1 mag brighter and three times larger bulge, with $n = 3.0$ instead of 1.1.Taken together, these alternatives indicate a systematic $m_{\rm bul}$ uncertainty of 0.5 mag.

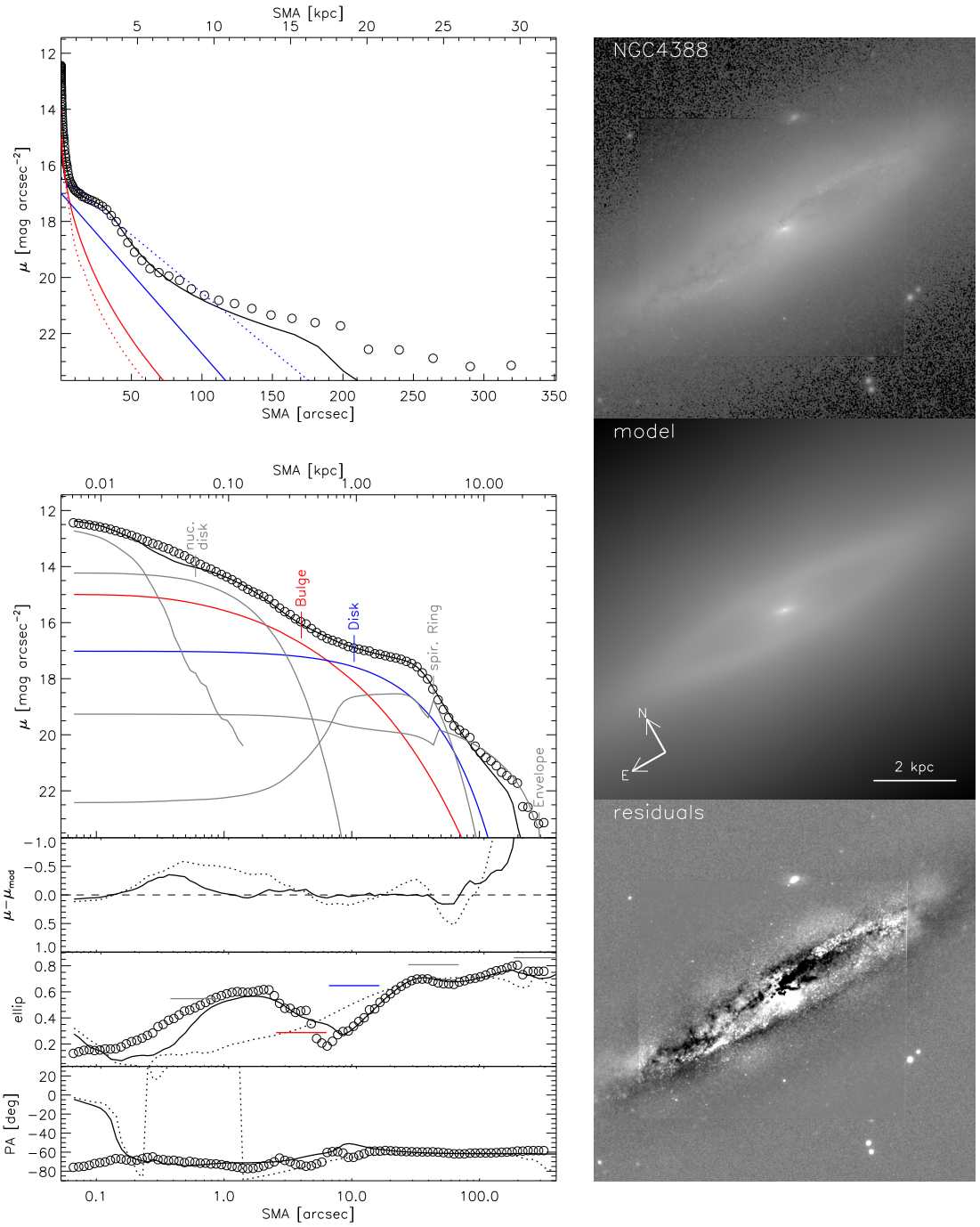

FIG. 19.— NGC4388 photometric data and model, with layout as in Figure 9. *Left panels:* semi-major axis (SMA) profiles of H-band surface brightness (μ), data-model residuals ($\mu - \mu_{\rm mod}$), ellipticity (ellip), and east-of-north position angle (PA). Open circles: data, solid lines: full model, dashed lines: basic (bulge+disk) model. Thick black: total model image profiles, red: bulge, blue: disk, and thin grey: all other components. Only select profiles are shown in the $\mu - {\rm SMA}$ (top panel) and $\mu - \log {\rm SMA}$ (second from top) plots (see also Figure 20). Ellipticities of individual components are indicated by horizontal bars. *Right panels:* Images of the data, model and residuals. The full model accounts for the nuclear disk, spiral arms, and outer disk (envelope) with exponential profiles, where the spiral arms component is modeled as a ring. The innermost profile is partially underpredicted, but corresponding models accounting for it by an additional component proved too degenerate, and dust in the center prevents a more accurate interpretation of the inner structure based on our image.

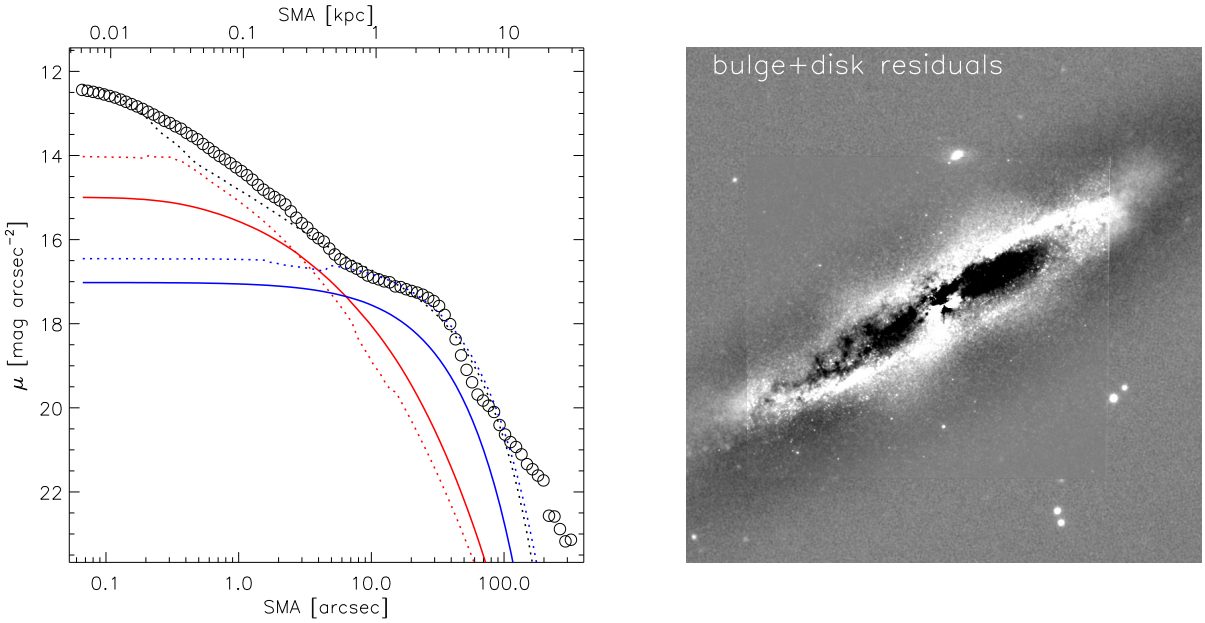

FIG. 20.— NGC4388 photometric data and model, continued from Figure 19. *Left panel:* SMA surface brightness (μ) of the data (open circles), full model (solid lines) and basic bulge+disk model (dashed), separately for total light (black), bulge (red) and disk (blue). *Right panel:* image of basic model residuals. The basic model residuals clearly expose the spiral arms, which wind tightly to nearly form a ring, as well as the thin (inclined) central nuclear disk and intervening dust lanes at all radii.

UGC 3789

UGC3789 (Figures 25 and 26) is a late-type galaxy that is seen nearly face-on and dominated by two rings, one close to the center at SMA = 3.8″ (900 pc), and the second one at SMA = 23″ (5.6 kpc). Both rings contain star forming regions and form the boundary of a disk, respectively. but the larger ring, as in NGC3393, might as well delineate a large-scale bar. The inner ring is nearly round, while the second ring shows marked flattening and asymmetry. Two short spiral arms emerge at a PA≈ 170 deg but varies by several degrees from the center outwards. A third, weaker ring is discernible in the μ profile at $\sim 40''$ (10 kpc) and marks the edge of the visible large-scale disk.

A basic bulge+disk+AGN model is clearly unsuitable to model this galaxy, due to the luminous rings and bar. The "bulge" component fitted by the basic model largely fits the inner ring and is therefore very compact ($n \sim 1$). The "disk" in the basic model roughly accounts for the light of the second ring. In our best-fit model, the rings are modeled by Gaussian profiles with inner truncation, except for the outer ring, which is an untruncated Sérsic profile with low index ~ 0.1 in the best-fit solution. Finally, the bar component becomes readily fit by a typical geometry ($q \sim 0.3$) and compact profile ($n \sim 0.3$).

The resulting reference model is a vast improvement over the basic model in terms of residuals and interpretation. Coincidentally, the bulge magnitude is almost identical to that of the basic model, but the bulge $R_e = 3''/700$ pc and $n = 3.3$ are $\sim 50\%$ and 300% larger, respectively. Fitting the outer ring proves essential to keep the size of the main disk from growing extremely large. The truncation of the two inner rings improve the residuals considerably and allow bulge and disk to account for the central and inter-ring light. Even if these models are less precise representations of the data, they are still superior to the simple model and acceptable alternatives. When removing the outer ring, or the truncation of the second ring, the classical bulge magnitude differs by -0.8 mag ($+0.2$ mag from the reference model respectively. Removing the truncation of the inner ring increases the residuals, but leaves $M_{\rm bul}$ nearly unchanged. Finally, we note that using a Sérsic profile for the main disk also leads to a very similar overall model, as the Sérsic index of the disk is $0.8 \approx 1$ in the best fit. On average, these alternatives provide for a systematic uncertainty estimate of the bulge magnitude of 0.4 mag.

ANCILLARY INFORMATION ON GALFIT IMAGE MODELING

Providing an accurate PSF

In order to account for the effects of the point-spread function (PSF), GALFIT convolves each model with a PSF image. A scaled version of the PSF image is also used as a model of a point source (AGN in our case). The accuracy of the PSF image effects the fit results of small-scale components near the galaxy center, including the bulge, and could in principle be important here. A PSF model can be provided by detailed modeling of the optical path and detector properties, as is commonly done for *HST* images. However, we found that the PSF that we obtained from TinyTim (Krist et al. 2010) is not adequate to describe the surface brightness distributiosn of stars that we observe on our target fields. The problem is large enough to leave characteristic ring-like residuals near the galaxy centers after

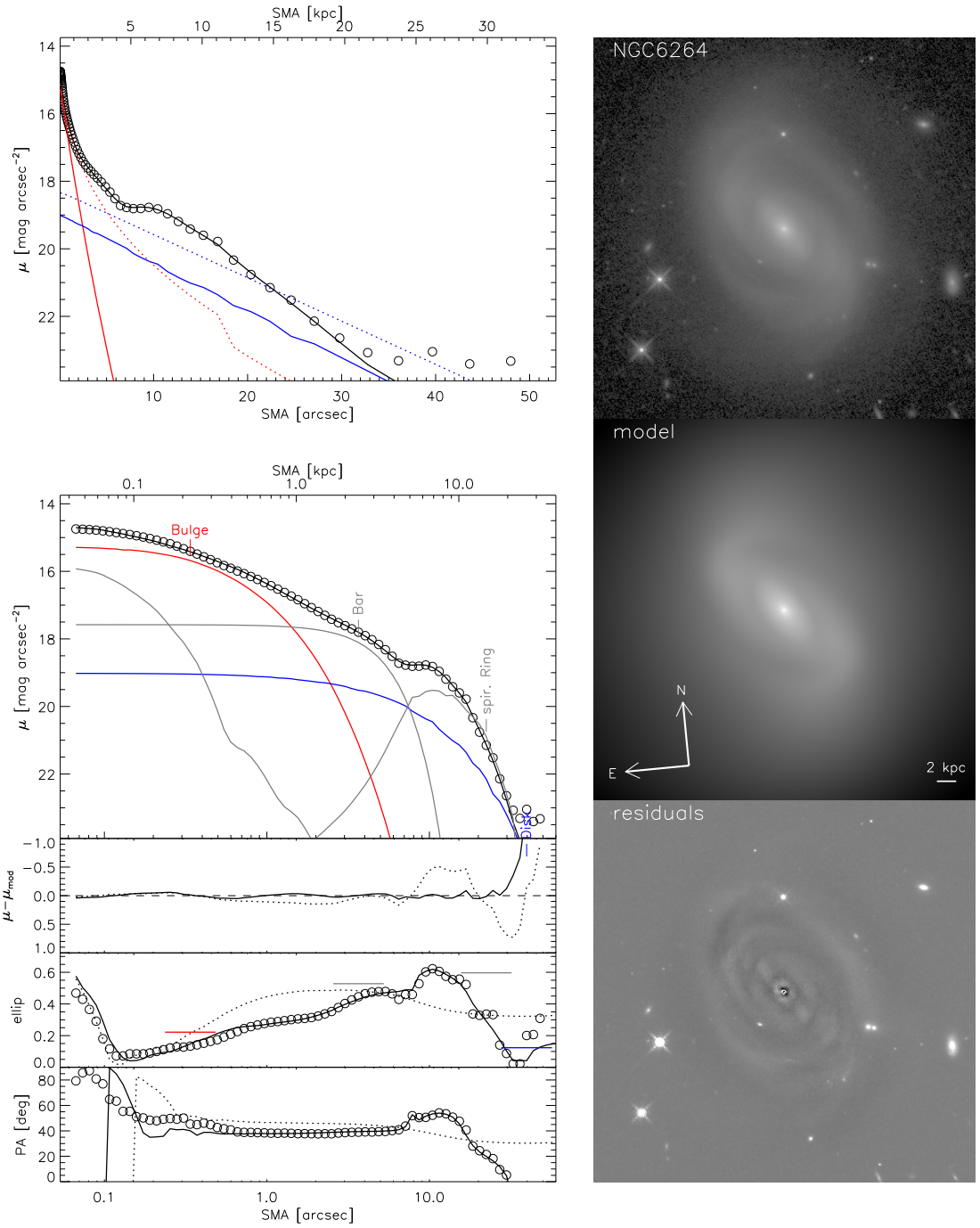

FIG. 21.— NGC6264 photometric data and model, with layout as in Figure 9. *Left panels:* semi-major axis (SMA) profiles of H-band surface brightness (μ), data-model residuals ($\mu - \mu_{\rm mod}$), ellipticity (ellip), and east-of-north position angle (PA). Open circles: data, solid lines: full model, dashed lines: basic (bulge+disk) model. Thick black: total model image profiles, red: bulge, blue: disk, and thin grey: all other components. Only select profiles are shown in the $\mu - {\rm SMA}$ (top panel) and $\mu - \log {\rm SMA}$ (second from top) plots (see also Figure 22). Ellipticities of individual components are indicated by horizontal bars. *Right panels:* Images of the data, model and residuals. The non-axisymmetric structure of NGC6264 is produced by the bar and spiral arms, which we model by a compact (best-fit $n = 0.47$) Sérsic and an exponential profile with both inner truncation and coordinate rotation, respectively. The bulge and bar profiles largely overlap and thus are somewhat degenerate, however their very different axis ratios and the steep profile in the center justify two seperate components here.

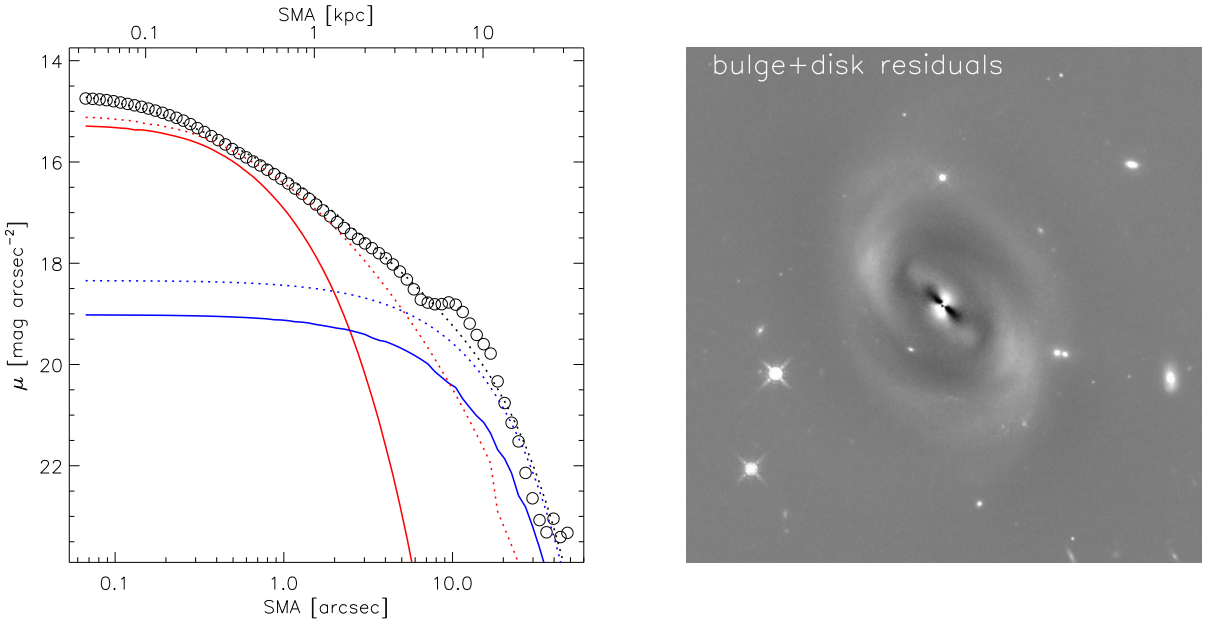

FIG. 22.— NGC6264 photometric data and model, continued from Figure 21. *Left panel:* SMA surface brightness (μ) of the data (open circles), full model (solid lines) and basic bulge+disk model (dashed), separately for total light (black), bulge (red) and disk (blue). *Right panel:* image of basic model residuals, which clearly exhibits the central bulge as distinct from the bar.

modeling, and to notably impact the AGN magnitude and bulge parameters in some of our targets. We therefore derive the PSF empirically using cutout images of non-saturated and isolated stars found on our (co-added) science frames. The co-addition of several of such star cutouts improves S/N and reduces residual background uncertainty. It has the drawback of potentially broadening the PSF profile near the center, due to finite pixel sampling and unavoidable centering error (we do not resample onto fractional pixels). We tested the broadening incurred in our co-added image and find it to be marginal (see Figure 27).

The PSF image must be large compared to the PSF FWHM to include most of the PSF image flux. We use a 43x43 pixel common cutout area, which is ~ 27 times the FWHM of $0.2''$ that we measure. Thus, our PSF image includes nearly 100% of the total PSF flux.

The sigma image

An image of the standard deviation of the flux per pixel (noise, or "sigma") is required to compute χ^2. Providing a realistic estimate of the sigma map is necessary for obtaining the "true" best-fit solution of a given model. We obtain the sigma image by first computing it on the ground-based and *HST* image stacks separately. This consists of measuring the background noise across the image as a whole (with objects masked) for the ground-based images, and adding in quadrature the Poisson noise from the object flux using the flux itself and the local effective gain. For the *HST* stacks, the noise can be computed since the four exposures are weighted evenly and all background levels are known precisely. Afterwards, the two images are scaled and combined, with the *HST* data replacing ground-based data wherever it is available, and the noise maps are scaled accordingly.

Object masks

Since we want to model the galaxy light unbiased by fore- and background objects, masks for the latter are indispensable. We create masks based on automatic object detection by SExtractor. We subsequently add masks by hand for stars that are particularly bright and thus have extended PSF wings, or those that overlap with the galaxy so that they are not picked up by the automatic detection. In one case (UGC3789), we opt not to mask the two stars near the galaxy center, but include them in our model and thereby avoid masking much of the area containing important constraints on the central profile. None of our fields are particularly crowded.

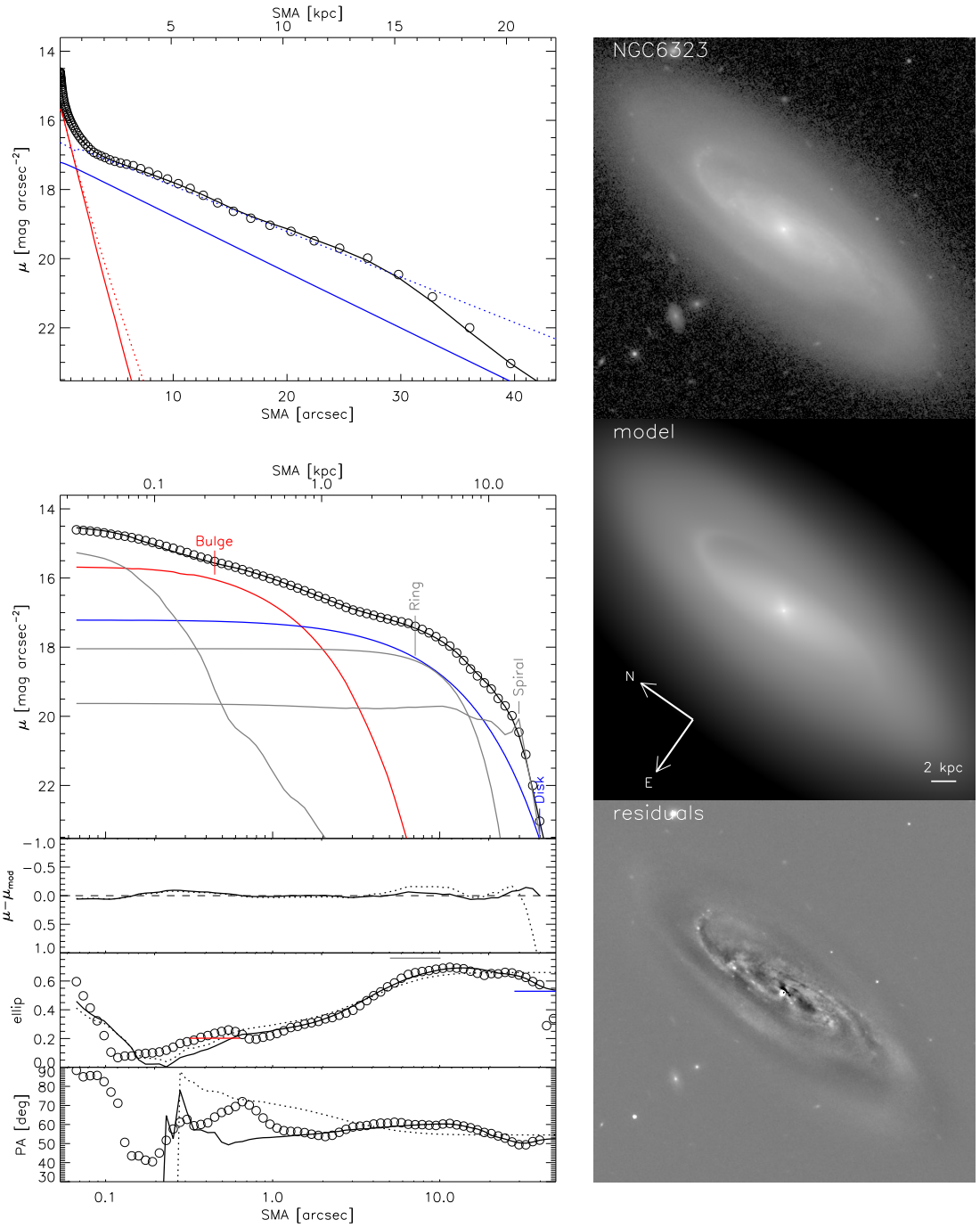

FIG. 23.— NGC6323 photometric data and model, with layout as in Figure 9. *Left panels:* semi-major axis (SMA) profiles of H-band surface brightness (μ), data-model residuals ($\mu - \mu_{\rm mod}$), ellipticity (ellip), and east-of-north position angle (PA). Open circles: data, solid lines: full model, dashed lines: basic (bulge+disk) model. Thick black: total model image profiles, red: bulge, blue: disk, and thin grey: all other components. Only select profiles are shown in the $\mu - {\rm SMA}$ (top panel) and $\mu - \log {\rm SMA}$ (second from top) plots (see also Figure 24). Ellipticities of individual components are indicated by horizontal bars. *Right panels:* Images of the data, model and residuals. The overall structure is simple, dominated by the disk and a clear profile steepening (bulge) in the centre. However, spiral arms and varying PA in the inner $\sim$ kpc are also evident, The spiral arms are not strong or sharply defined in the H-band; we model them nevertheless by an exponential profile, modified by coordinate rotation and an inner truncation. They appear to emerge from an elongated structure that nearly forms a ring, which likely delineates an inner disk (a putative pseudobulge), but possibly also represents a bar. We model this structure separately by a Sérsic component (best-fit axis ratio $q \sim 0.2$ and $n \sim 0.4$) and thus distinguish it from the very round ($q \sim 0.8$) small ($R_e \sim 0.7\,$kpc) classical bulge, for which we allowed a 4th-order isophotal harmonic to account for its boxiness.

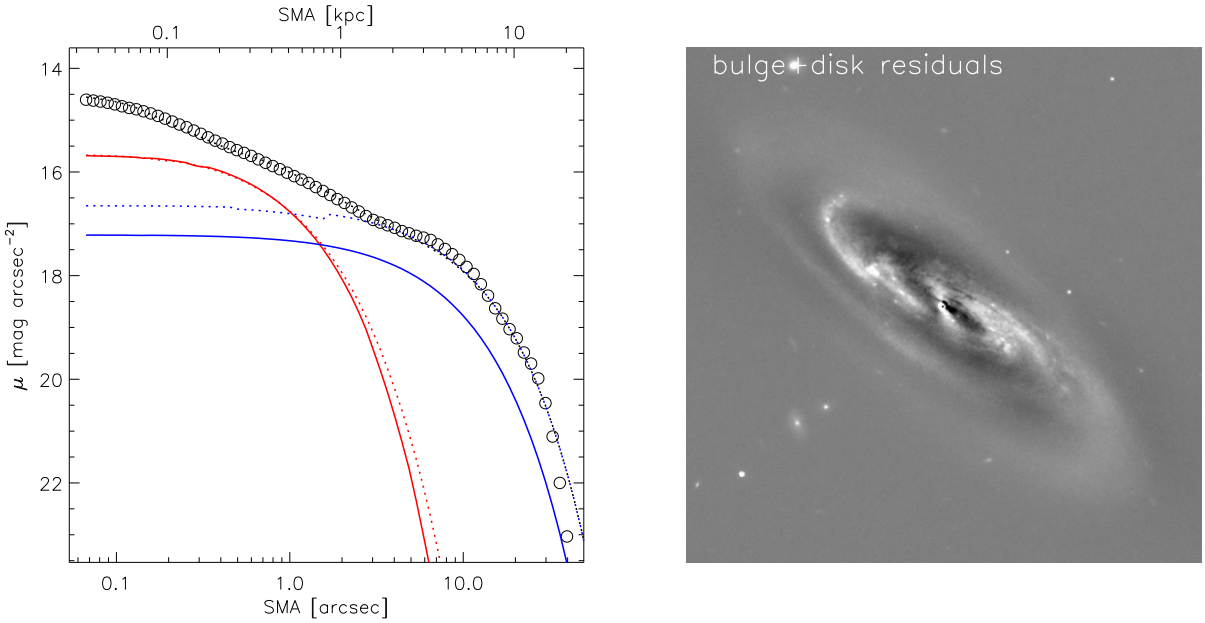

FIG. 24.— NGC6323 photometric data and model, continued from Figure 23. *Left panel:* SMA surface brightness (μ) of the data (open circles), full model (solid lines) and basic bulge+disk model (dashed), separately for total light (black), bulge (red) and disk (blue). *Right panel:* image of basic model residuals, which highlight the spiral arms as well as the inner disk (or bar) from which the spiral arms emerge.

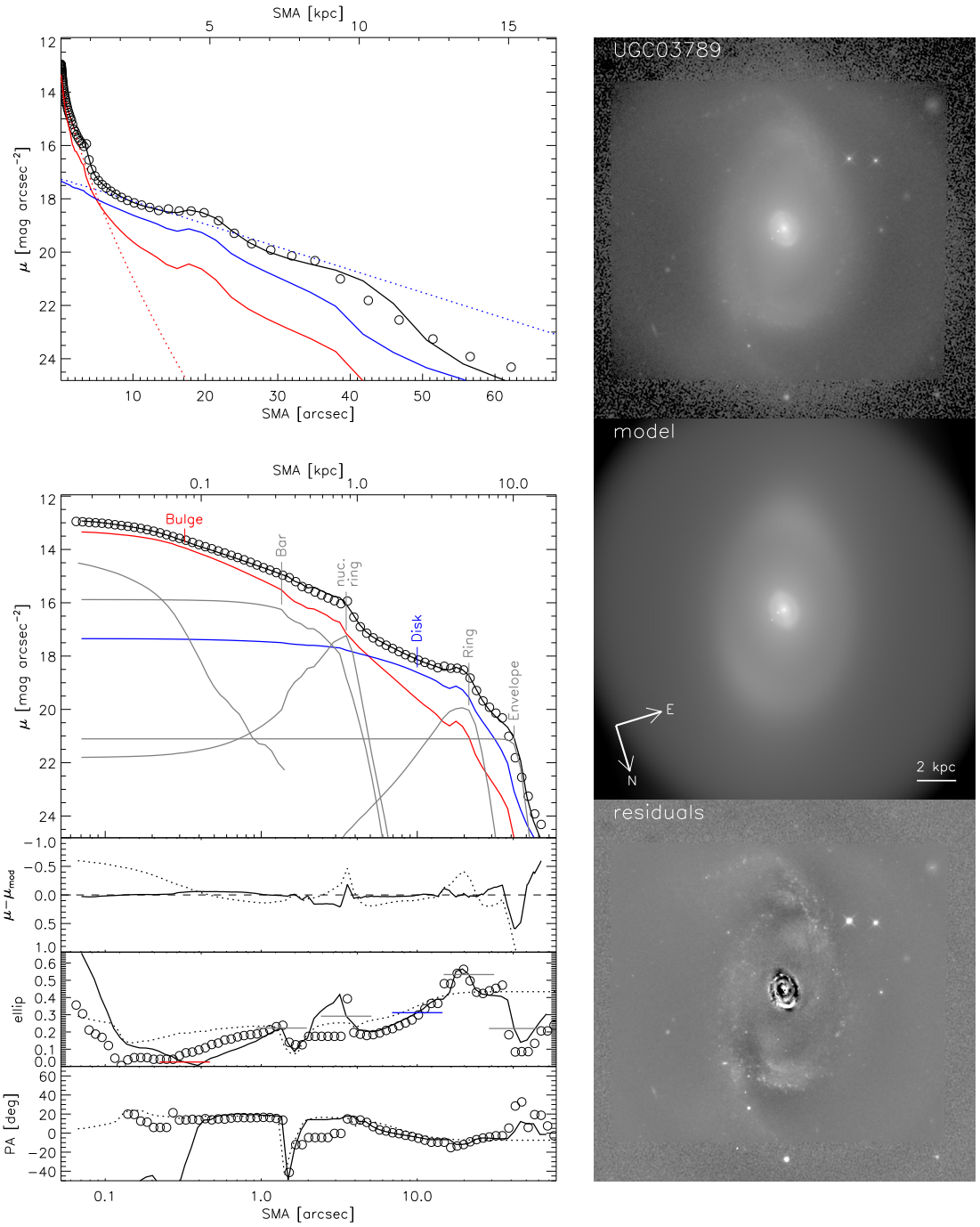

FIG. 25.— UGC3789 photometric data and model, with layout as in Figure 9. *Left panels:* semi-major axis (SMA) profiles of H-band surface brightness (μ), data-model residuals ($\mu - \mu_{\rm mod}$), ellipticity (ellip), and east-of-north position angle (PA). Open circles: data, solid lines: full model, dashed lines: basic (bulge+disk) model. Thick black: total model image profiles, red: bulge, blue: disk, and thin grey: all other components. Only select profiles are shown in the $\mu-$SMA (top panel) and $\mu-\log$SMA (second from top) plots (see also Figure 26). Ellipticities of individual components are indicated by horizontal bars. *Right panels:* Images of the data, model and residuals. The structure of UGC3789 is similar to NGC3998, with a large-scale round outer disk on which faint and weakly defined spiral arms and star-forming regions are superposed, a bright large elongated inner disk (or bar) delineated by a bright star forming ring, and a round nuclear disk/ring with an inset nuclear bar. We model the bar by a Sérsic profile (best-fit $n \sim 0.3$), and the rings with Gaussian profiles with an inner truncation (dropping the truncation for the outer ring due to excessive degeneracy). The best-fit model reproduces the profiles accurately compared to the basic model, especially in terms of the steep central ($\lesssim 100$ pc) brightness and variations in the ellipticity.

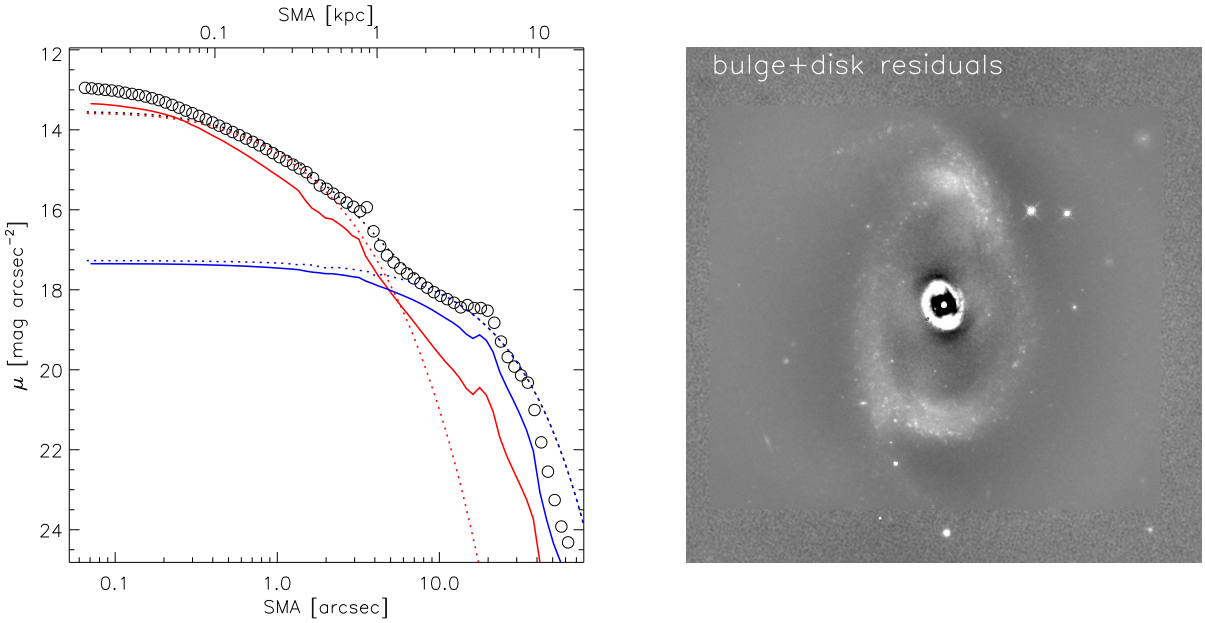

FIG. 26.— UGC3789 photometric data and model, continued from Figure 25. *Left panel:* SMA surface brightness (μ) of the data (open circles), full model (solid lines) and basic bulge+disk model (dashed), separately for total light (black), bulge (red) and disk (blue). *Right panel:* image of basic model residuals, which exposes the intermediate elongated ring (extending about half the way to the edge of the shown image), as well as the nuclear ring and bar. The basic model bulge is biased by this nuclear ring and bar to a too compact profile, which we avoid in the full model by separate nuclear bar and ring components. The basic model also renders an overprediction for the disk (and hence the total) luminosity due to the influence of the kpc-scale bar/ring that is included as a component in the full model as well.

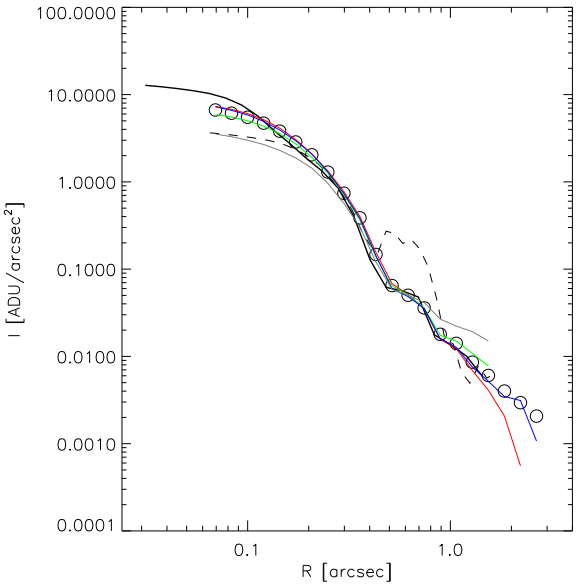

FIG. 27.— Comparison of our empirical PSF (open circles) with the analytic TinyTim-based profile (dashed curve). The two are quite different in the center and around 0.5″, and the analytic version causes significant mismatch with observed stars and bright galaxy centers. The profiles of individual stars used to construct the PSF image (thin colored curves) agree well with their sum and with one another, indicating that broadening by centering errors, residual background, contamination and saturation are minimal. Confirmation of the accuracy of our empirical PSF also comes from comparing it with an independent derivation by the CANDELS collaboration (solid thick black curve), which albeit used upsampling before co-addition (to 0.06″), and therefore probes closer to the PSF center